# Computational Insights into the Corrosion Behavior of NbTaMoW and NbTaMoWV High-Entropy Alloys in Molten Fluoride Salts

by

Agnes Katai

A thesis
presented to the University of Waterloo
in fulfillment of the
thesis requirement for the degree of
Master of Science
in
Chemistry

Waterloo, Ontario, Canada, 2025

© Agnes Katai 2025

## Author's Declaration

This thesis consists of material all of which I authored or co-authored: see Statement of Contributions included in the thesis. This is a true copy of the thesis, including any required final revisions, as accepted by my examiners.

I understand that my thesis may be made electronically available to the public.

## Statement of Contributions

Aside from chapter 1 and section 2.1-2.2, this thesis is composed of a published manuscript for which I served as the first author. Following is a delineation of my co-authors' contributions towards my manuscript:

- Section 2.3 and Chapter 3: This section and chapter are reproduced from Agnes Britte Katai, Arjun Varma Ramasimha Varma, and Conrard Giresse Tetsassi Feugmo; "Computational Insights into the corrosion behavior of NbTaMoW and NbTaMoWV high-entropy alloys in molten fluoride salts", Faraday Discuss. (2025). https://doi.org/10.1039/D5FD00102A.

  This article is published and reused under the terms of a Creative Commons Attribution-NonCommercial 3.0 Unported license: https://creativecommons.org/licenses/by-nc/3.0/

  Conrard Giresse Tetsassi Feugmo and I (Agnes Britte Katai) collaboratively developed the computational framework. I implemented the framework, performed all calculations, and analyzed the data. I drafted the manuscript with input from all authors. Arjun Varma Ramasimha Varmaa assisted in writing – review and editing. Conrard Giresse Tetsassi Feugmo conceived the study and supervised the overall direction and planning.

**Abstract**

Molten salt reactors (MSRs), one of the six next-generation nuclear reactor designs, employ molten fluoride salts as the coolant and/or fuel solvent when operated in a thermal-neutron spectrum, and offer higher thermal efficiency compared to today's water-cooled reactors. Nonetheless, the elevated temperatures, corrosive nature of salts, and high neutron irradiation in MSRs create a harsh environment for structural materials. The influx of impurities, namely moisture, into the molten salt medium has long been shown to exacerbate the corrosivity of fluorides. Owing to their superior thermal and mechanical robustness, refractory high-entropy alloys with a body-centered cubic (BCC) structure have been proposed as candidate containment materials for MSRs. Nonetheless, the degradation of these advanced materials in molten fluorides is an intricate process whose underlying mechanisms remain poorly understood. This study explores the corrosion behavior of BCC (100)-NbTaMoW and (100)-NbTaMoWV surfaces in pure and hydrated FLiBe salt via density functional theory and ab initio molecular dynamics simulations. Electronic structure analyses, including density of states and crystal orbital Hamilton population, provide insight into the interfacial bonding and charge transfer. Irrespective of salt purity, NbTaMoW exhibits minimal d-band shifts which highlight its electronic stability, and weak interactions with fluorine and oxygen. The addition of vanadium to form NbTaMoWV further diminishes susceptibility to oxidation and enhances stability at the salt interface, suggesting superior corrosion resistance in both pure and hydrated salt.

## Acknowledgements

I would first like to thank my supervisor, Dr. Conrard Tetsassi, for assisting me in learning the complex material associated with this research topic and undertaking the various challenges that emerged during this project. I am also grateful for the essential revisions he made to the initial draft of my manuscript. Additionally, I would like to thank my postdoctoral colleague, Arjun Varma, for providing valuable insight into the project and refining the final draft of the manuscript.

I am also grateful to my advisory committee members, Marcel Nooijen and Rodney Smith, for providing me with important feedback following my research seminar, which played a key role in the progress of my work.

Finally, I would like to credit my family and friends for their unconditional support and encouragement.

This work was supported by NSERC-CNSC Small Modular Reactors Research Grant Initiative. This work was made possible by the facilities of the Shared Hierarchical Academic Research Computing Network (SHARCNET: https://www.sharcnet.ca) and Digital Research Alliance of Canada https://alliancecan.ca/en.

# Table of Contents

**Author's Declaration** ii

**Statement of Contributions** iii

**Abstract** iv

**Acknowledgements** v

**List of Figures** ix

**List of Tables** xiv

**List of Abbreviations** xv

**1 Introduction** 1

1.1 Molten salt reactors for advanced nuclear power generation . . . . . 1

1.1.1 Background and significance . . . . . 1

1.1.2 Principles . . . . . 2

1.1.3 Coolant Selection and Thermophysical Considerations . . . . . 5

1.1.4 Materials Selection and Challenges . . . . . 6

1.2 Corrosion Processes . . . . . 8

1.2.1 Thermodynamics of fluoride formation . . . . . 8

1.2.2 Impurities . . . . . 9
1.2.3 Diffusion along Grain Boundaries . . . . . 10
1.3 High Entropy Alloys as Alternative Materials . . . . . 11
1.3.1 Background . . . . . 11
1.3.2 Corrosion Investigations . . . . . 15

**2 Methodology** **18**
2.1 Classical Molecular Dynamics . . . . . 18
2.1.1 Particle Dynamics . . . . . 18
2.1.2 Velocity Verlet Algorithm . . . . . 20
2.1.3 Nosé–Hoover Thermostat . . . . . 21
2.2 Density Functional Theory . . . . . 24
2.2.1 The Many-Body Problem . . . . . 24
2.2.2 Kohn-Sham self-consistent field . . . . . 27
2.2.3 Plane-wave calculations . . . . . 29
2.2.4 Ab Initio Molecular Dynamics . . . . . 31
2.2.5 Density of States . . . . . 32
2.2.6 Projected Crystal Orbital Hamilton Populations . . . . . 34
2.2.7 Electron Localization Function . . . . . 36
2.3 Computational Framework . . . . . 37

**3 Observations** **43**
3.1 HEA Subsystem Equilibration . . . . . 43
3.2 Density of States . . . . . 45
3.3 Crystal Orbital Hamilton Population Analysis . . . . . 51

3.4 Electron Localization Function . . . . . 59
3.5 Effect of RHEAs on Salt Chemistry . . . . . 64
3.6 Conclusions . . . . . 67

**References** **69**

**APPENDICES** **77**

**A Results** **78**

**B Results** **90**

B.1 Revised Computational Workflow . . . . . 90
B.2 Revised Observations . . . . . 92
B.2.1 Radial Distribution Function . . . . . 92
B.2.2 $H_2O$ Reaction Mechanism . . . . . 93
B.2.3 Density of States . . . . . 94
B.2.4 Crystal Orbital Hamilton Population Analysis . . . . . 95

# List of Figures


1.1 Schematic diagram of a molten salt reactor from the US Department of Energy (US DOE) Roadmap.[3] . . . . . 2

1.2 Simplified atomic distribution in a (a) solid solution and (b) intermetallic. 12

2.1 Workflow for constructing the refractory high entropy alloy (RHEA)–salt interface. . . . . 38

2.2 Bird's eye view of surface atoms (top) and side view (bottom) of (100)-NbTaMoW and (100)-NbTaMoWV slabs. . . . . 39

3.1 Common neighbor analysis of (100)-NbTaMoW (top) and (100)-NbTaMoWV (bottom) slabs after 100 ps of NPT using classical molecular dynamics with tabGAP potentials[82]. . . . . 44

3.2 Total radial distribution function of a) (100)-NbTaMoW and b) (100)-NbTaMoWV slabs at 0 ps (top, blue) and 100 ps (bottom, red) of *NPT* at 800 K using classical molecular dynamics with tabGAP potentials[82]. . . . . 45

3.3 Total and partial density of states of the BCC (100)- a) NbTaMoW and b) NbTaMoWV surfaces, in contact with a molten FLiBe salt after 40 ps at 800 K. . . . . 48

3.4 Total and partial density of states of the BCC (100) a) NbTaMoW and b) NbTaMoWV surfaces, in contact with a molten FLiBe salt contaminated with a $H_2O$ molecule after 40 ps at 800 K. . . . . 49

3.5 Total and partial density of states of BCC (100) NbTaMoW and NbTaMoWV surfaces, in contact with a) pure molten FLiBe salt and b) FLiBe salt contaminated with a $H_2O$ molecule after 40 ps at 800 K. . . . . 50

3.6 The evolution of bond length and integrated crystal orbital Hamilton population (ICOHP) of representative metal fluorides at the a) (100)-NbTaMoW−FLiBe and b) (100)-NbTaMoWV−FLiBe interface at 800 K. . . . . 55

3.7 The evolution of bond length and integrated crystal orbital Hamilton population (ICOHP) of representative metal fluorides at the a) (100)-NbTaMoW−$H_2O$−FLiBe and b) (100)-NbTaMoWV−$H_2O$−FLiBe interfaces at 800 K. . . . . 56

3.8 Crystal orbital Hamilton population (COHP) analysis of the BCC (100) surfaces of a) NbTaMoW and b) NbTaMoWV in contact with molten FLiBe 57

3.9 Crystal orbital Hamilton population (COHP) analysis of the BCC (100) surfaces of a) NbTaMoW and b) NbTaMoWV in contact with molten FLiBe contaminated with a $H_2O$ molecule. . . . . 58

3.10 Change in valence electrons of representative surface atoms at the interface between (100)-NbTaMoW and pure FLiBe at 800 K. . . . . 61

3.11 Change in valence electrons of representative surface atoms at the interface between (100)-NbTaMoWV and pure FLiBe at 800 K. . . . . 62

3.12 Change in valence electrons of representative surface atoms at the interface between (100)-NbTaMoW and $H_2O$-contaminated FLiBe at 800 K. . . . . 63

3.13 Change in valence electrons of representative surface atoms at the interface between (100)-NbTaMoWV and $H_2O$-contaminated FLiBe at 800 K. . . . . 63

3.14 Radial distribution function of FLiBe salt after contact with a) (100)-NbTaMoW and b) -NbTaMoWV at 800 K for 40 ps. . . . . 65

3.15 Radial distribution function of $H_2O$-contaminated FLiBe salt after contact with a) (100)-NbTaMoW and b) -NbTaMoWV at 800 K for 40 ps. . . . . 66

A.1 Total and partial density of states of BCC (100) surfaces of (a) NbTaMoW and (b) NbTaMoWV, in contact with a molten FLiBe salt after 20 ps at 800 K. . . . . 80

A.2 Total and partial density of states of BCC (100) surfaces of (a) NbTaMoW and (b) NbTaMoWV, in contact with a molten FLiBe salt after 30 ps at 800 K. . . . . 81

A.3 Total and partial density of states of BCC (100) surfaces of (a) NbTaMoW and (b) NbTaMoWV, in contact with a molten FLiBe salt contaminated with a $H_2O$ molecule after 20 ps at 800 K. . . . . 82

A.4 Total and partial density of states of BCC (100) surfaces of (a) NbTaMoW and (b) NbTaMoWV, in contact with a molten FLiBe salt contaminated with a $H_2O$ molecule after 30 ps at 800 K. . . . . 83

A.5 Murnaghan's equation of state for BCC refractory metal unit cells calculated using Density Functional Theory with PBE exchange-correlation functional. 84

A.6 Murnaghan's equation of state for BCC refractory metal unit cells calculated using Density Functional Theory with PBE exchange-correlation functional. 85

A.7 Crystal Orbital Hamilton Population (COHP) analysis of the BCC (100)-NbTaMoW surface in contact with molten FLiBe at 800 K, shown at four time points: (i) 10 ps, (ii) 20 ps, (iii) 30 ps, and (iv) 40 ps. . . . . 86

A.8 Crystal Orbital Hamilton Population (COHP) analysis of the BCC (100)-NbTaMoWV surface in contact with molten FLiBe at 800 K, shown at four time points: (i) 10 ps, (ii) 20 ps, (iii) 30 ps, and (iv) 40 ps. . . . . 87

A.9 Crystal orbital Hamilton population (COHP) analysis of the BCC (100)-NbTaMoW surface in contact with molten FLiBe contaminated with a $H_2O$ molecule at 800 K, shown at four time points: (i) 10 ps, (ii) 20 ps, (iii) 30 ps, and (iv) 40 ps. . . . . 88

A.10 Crystal orbital Hamilton population (COHP) analysis of the BCC (100)-NbTaMoWV surface in contact with molten FLiBe contaminated with a $H_2O$ molecule at 800 K, shown at four time points: (i) 10 ps, (ii) 20 ps, (iii) 30 ps, and (iv) 40 ps. . . . . 89

B.1 Revised workflow for constructing the refractory high entropy alloy (RHEA)–salt interface. . . . . 91

B.2 a) Total radial distribution function for the metal surface component of the $H_2O$-contaminated FLiBe-NbTaMoW interface and the b) Radial distribution function for the fluoride bonds in the $H_2O$-contaminated FLiBe overlay on NbTaMoW after 10 ps at 800 K in the $NVT$ ensemble. . . . . 92

B.3 a) Total radial distribution function for the metal surface component of the $H_2O$-contaminated FLiBe-NbTaMoWV interface and the b) Radial distribution function for the fluoride bonds in the $H_2O$-contaminated FLiBe overlay on NbTaMoWV after 10 ps at 800 K in the $NVT$ ensemble. . . . . 92

B.4 The splitting of the $H_2O$ molecule at the molten FLiBe-NbTaMoW interface after a) 0.155 ps, b) 0.156 ps, c) 0.157 ps and d) 0.158 ps at 800 K in the $NVT$ ensemble. . . . . 93

B.5 The splitting of the $OH^-$ molecule at the molten FLiBe-NbTaMoW interface after a) 0.815 ps, b) 0.816 ps, c) 0.817 ps and d) 0.818 ps at 800 K in the $NVT$ ensemble. . . . . 93

B.6 The splitting of the $H_2O$ molecule at the molten FLiBe-NbTaMoWV interface after a) 0.026 ps, b) 0.028 ps, c) 0.030 ps and d) 0.032 ps at 800 K in the $NVT$ ensemble. . . . . 94

B.7 Total and partial density of states of the BCC (100) a) NbTaMoW and b) NbTaMoWV surfaces, in contact with a molten FLiBe salt contaminated with a $H_2O$ molecule after 10 ps of the revised simulation at 800 K. . . . . 95

B.8 Crystal orbital Hamilton population (COHP) analysis of the BCC (100) surfaces of a) NbTaMoW and b) NbTaMoWV in contact with molten FLiBe contaminated with a $H_2O$ molecule after 10 ps of the revised simulation at 800 K. . . . . 97

# List of Tables

A.1 Bond lengths and ICOHP values for (100)-NbTaMoW slab in contact with FLiBe at 10, 20, 30, and 40 ps. . . . . 78

A.2 Bond lengths and ICOHP values for (100)-NbTaMoWV slab in contact with FLiBe at 10, 20, 30, and 40 ps. . . . . 78

A.3 Bond lengths and ICOHP values for (100)-NbTaMoW slab in contact with FLiBe contaminated with a $H_2O$ molecule at 10, 20, 30, and 40 ps. . . . . 79

A.4 Bond lengths and ICOHP values for (100)-NbTaMoWV slab in contact with FLiBe contaminated with a $H_2O$ molecule at 10, 20, 30, and 40 ps. . . . . 79

A.5 Structural properties of BCC refractory metal unit cells calculated using DFT with PBE functional and 2b+3b tabGAP potentials. . . . . 79

# List of Abbreviations

**AIMD** ab initio molecular dynamics

**ASE** Atomic Simulation Environment

**BCC** body-centered cubic

**CNSC** Canadian Nuclear Safety Commission

**COHP** crystal orbital Hamilton population

**DFT** density functional theory

**DOS** density of states

**ELF** electron localization function

**EOS** equation of state

**GGA** generalized gradient approximation

**GIF** Generation IV International Forum

**HEA** high entropy alloy

**ICOHP** integrated crystal orbital Hamilton population

**LAMMPs** Large-scale Atomic/Molecular Massively Parallel Simulator

**LWR** light water reactor

**MSR** molten salt reactor

**PAW** projector augmented wave

**PBE** Perdew-Burke-Ernzerhof

**RHEA** refractory high entropy alloy

**SMR** small modular reactor

**VASP** Vienna Ab initio Simulation Package

# Chapter 1

# Introduction

## 1.1 Molten salt reactors for advanced nuclear power generation

### 1.1.1 Background and significance

Nuclear reactors remain a key carbon-neutral energy source capable of delivering the multi-gigawatt power output required to meet the rising global electricity demands driven by AI data centers and growing communities worldwide. Beyond power generation, advanced reactor systems also provide high-temperature heat for hydrogen production, desalination, and a wide range of industrial processes, supporting deep decarbonization across multiple sectors[1,2]. Most of the nuclear reactors in operation today are light water reactors (LWRs), which remain limited in both thermal efficiency and cost-effectiveness[3]. Established in 2001, the Generation IV International Forum (GIF) is a collaborative initiative among 13 countries to coordinate the research and development of Generation IV nuclear systems, which offer advancements in safety, sustainability and efficiency compared to current reactors[4]. The ultimate mission of GIF is to facilitate the deployment and commercialization of Generation IV reactors by 2030. One of the most promising designs proposed by GIF is the molten salt reactor (MSR), distinguished by its inherent passive safety, enhanced thermal efficiency, and improved fuel utilization. The unique advantages

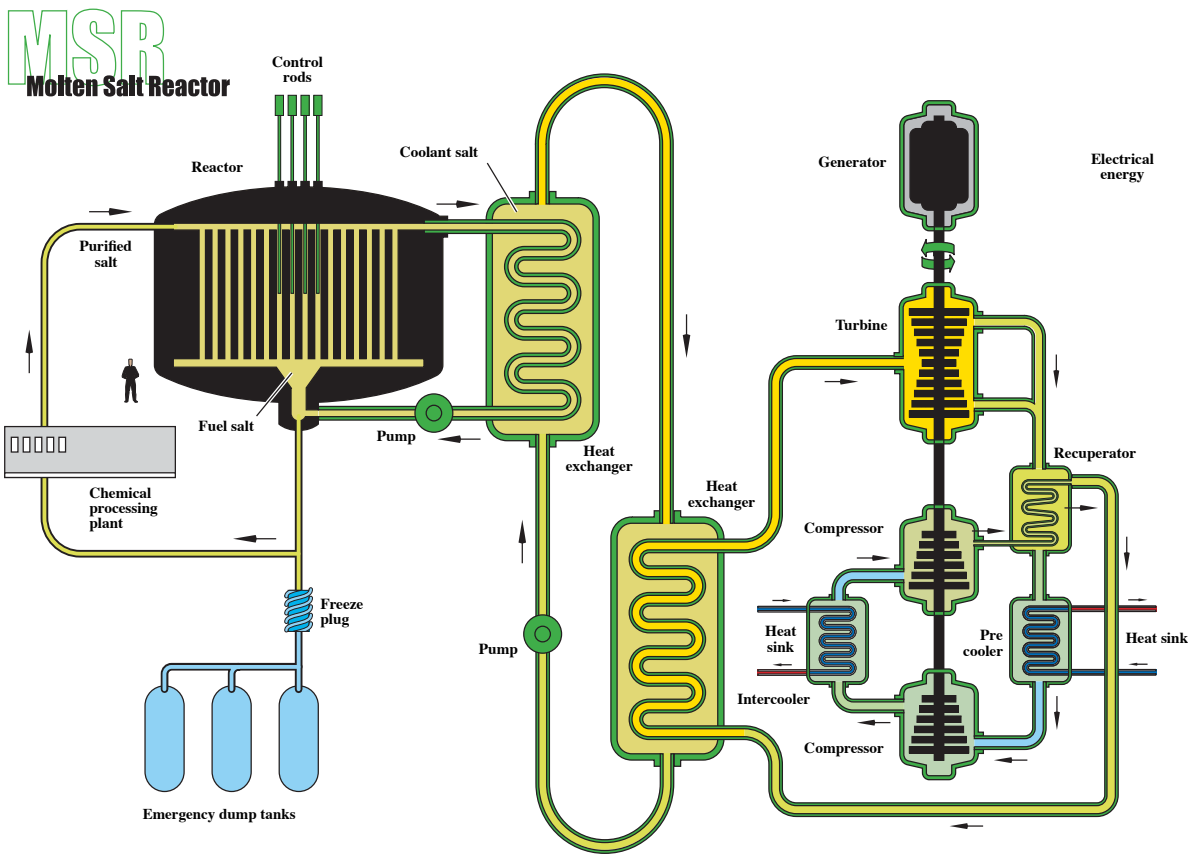



Figure 1.1: Schematic diagram of a molten salt reactor from the US Department of Energy (US DOE) Roadmap.[3]

offered by MSRs derive from their employment of molten fluoride or chloride salts as the fuel solvent and/or primary coolant medium. The MSR reactor concept originated from the Molten Salt Reactor Experiment led by the Oak Ridge National Laboratories in the 1960s which later regained interest from GIF[5,6]. In Canada, Terrestrial Energy has developed a small modular reactor (SMR) concept based on molten salt technology, which has cleared a pre-licensing design review by the Canadian Nuclear Safety Commission (CNSC) in 2023, achieving an early milestone toward commercialization[6,7].

### 1.1.2 Principles

A liquid fuel thermal MSR is depicted in Fig. 1.1. During MSR operation, nuclear fission is confined to the reactor core, enclosed by a high-strength, irradiation-resistant structural

material[8–10]. MSRs can be operated with neutrons in the fast-, thermal- and epithermal-energy range[11]. Fast neutron MSRs utilize chloride salts as the primary fuel solvent and/or coolant medium due to their high neutron capture cross-section while thermal and epithermal neutron MSRs employ fluoride salts as a result of their lower propensity for neutron capture. The thermal energy generated by the fission reaction heats up the primary coolant salt inside the reactor core which operates between 500 °C and 600 °C. The primary coolant subsequently transfers this energy to a secondary coolant salt in a heat exchanger[8,9]. The primary and secondary coolant are typically LiF–$BeF_2$ and LiF–NaF–KF, respectively, which must be in the liquid phase for adequate heat storage and transfer[12]. The heat stored by the secondary coolant is transferred to a water loop, where it is used to produce steam for electricity generation or other industrial applications. The intermediate loop was developed to segregate the fuel from the steam, thereby minimizing safety risks.

There are two variations in MSR design: salt-fueled and salt-cooled reactors. In salt-fueled reactors, fissile material such as uranium-235, uranium-233 and plutonium-239, is dissolved in a liquefied salt, typically LiF–$BeF_2$, allowing the fluid to serve simultaneously as fuel medium and primary coolant[11]. The fluoride salts of thorium, uranium, and plutonium are highly soluble in molten LiF–$BeF_2$, simplifying the separation of these fuel species from salt-insoluble fission fragments during chemical reprocessing of spent fuel (Fig. 1.1). The fuel-salt mixture is pumped at low pressure through the reactor core and the primary circuit. The assembly of control rods inside the reactor vessel regulate the neutron energy to sustain the nuclear fission chain reaction. Thermal neutron MSRs employ graphite rods as a neutron moderator due to the irradiation, chemical, and thermal stability of graphite, as well as its poor neutron absorption cross-section[11,13,14]. In contrast, salt-cooled reactors utilize solid fuel encased in metal rods around which the primary coolant salt circulates. In a salt-cooled, thermal-neutron MSRs, the fuel rods are inserted in graphite moderator blocks immersed in the circulating coolant salt. Hence, the salt-cooled MSR variant is not a radical departure from today's nuclear reactors.[11].

The use of molten salt as a coolant confers safety, economic, and environmentally friendly advantages[8,9,11,14]. Due to their low melting point, vapor pressure and high boiling

point, molten salts remain liquid within a broad temperature range, allowing MSRs to operate at higher temperatures ($T \approx 800$–$1000\,K$) and very low pressure ($p \approx 5\,atm$) compared to standard water-cooled reactors ($T \approx 573\,K$ and $p \approx 150\,atm$)[14]. These operating conditions increase thermal efficiency and reduce mechanical stresses on the vessel and piping, respectively, the latter of which lessens the possibility of radioactive nuclide dispersion and costly replacement of reactor components[3,12]. Since its melting point is well above room temperature and it binds strongly to many radioisotopes, the molten salt would deposit on the ground and freeze in the event of a coolant leakage, containing the radioactive material[14,15].

The use of a liquefied fuel in nuclear reactors offers additional safety and economic benefits. Unlike solid fuel which is encased in metal cladding, the chemical composition of a liquid fuel-salt can be continuously adjusted during reactor operation via online fuel reprocessing. This involves the continuous removal of fission products from the carrier salt through pyroprocessing, and simultaneous fuel replenishment (Fig. 1.1), maximizing fuel utilization[6]. Since many fission fragments have a high neutron capture cross-section, their presence in the fuel salt impedes neutron economy, which underscores the importance of continuous fuel cleanup[8]. Owing to the long half life of transuranic elements recovered from spent fuel, such as neptunium, americium, and curium, radioactive waste disposal remains a challenge. After separation from the fluoride medium, transuranic elements can undergo transmutation by fast or epithermal neutron reactors into fissile radioisotopes or short-lived fission products, the latter of which can be processed for applications in radiodiagnostics and radiation therapy, thereby optimizing resource utilization and eliminating hazardous waste disposal challenges[12,16,17].

Furthermore, when the reactor power exceeds a certain threshold, the fuel-salt mixture undergoes thermal expansion, reducing the fuel density, and thereby, fission rate and temperature[6,11]. This inherent negative feedback mechanism minimizes the need for active operator intervention. Additionally, the freeze plug (Fig. 1.1) made of solidified salt, melts past a certain power threshold, draining the fuel salt from the core into emergency dump tanks where it remains in subcritical state[6,8].

### 1.1.3 Coolant Selection and Thermophysical Considerations

Candidate salts must exhibit specific thermophysical properties to be suitable as coolants in nuclear reactors[18]. Low melting point, viscosity and corrosivity, together with high volumetric heat capacity and thermal conductivity, are key attributes that must be considered when selecting a salt as a primary and/or secondary coolant. If a salt is to serve as both a fuel solvent and a primary coolant, it must satisfy additional criteria, including low neutron capture cross-section, resistance to irradiation, high density, relatively low toxicity and high solubility of fissile materials such as plutonium fluoride ($PuF_3$) and uranium fluoride ($UF_4$). Fluoride salts best fulfill the criteria for both fuel solvent and coolant, making them promising candidates for applications in thermal- and epithermal- neutron MSRs. Nonetheless, fluoride salts are heavily limited by their corrosive effects on MSR structural materials which may be reduced by ensuring high salt purity, optimizing the chemical and molar salt composition, and employing corrosion-resistant container materials. Among the various fluoride salt mixtures characterized, LiF–NaF–KF (FLiNaK) and LiF–$BeF_2$ (FLiBe), have shown to be the most promising candidates for both fuel medium and coolant applications. 66-34% LiF–$BeF_2$, in particular, has been proposed for the first time as a fuel carrier and primary coolant in the MSR experiment by Oak Ridge National University and has been extensively studied in previous molten salt corrosion research[13,19].

A low melting point enables a broader operational temperature range for the reactor. According to safety protocols, the melting point of the salt must be at least 50 K lower than the inlet temperature of the MSR[8]. Individual salt components such as LiF, $BeF_2$, NaF, and KF are generally combined into binary or ternary mixtures, referred to as eutectic salts, which melt at a lower temperature than their constituent salts[9]. The chemical and molar composition of eutectic salts may be tuned accordingly to optimize for various thermophysical properties[9]. For example, in the LiF-$BeF_2$ eutectic mixture, the melting point decreases and the viscosity increases with $BeF_2$ content[18].

Volumetric heat capacity, thermal conductivity, and viscosity are key parameters governing heat storage and transfer performance[18]. The volumetric heat capacity of the salt, a function of the specific heat capacity and density, dictates the size of the reactor vessel

needed to store a specified amount of heat; a higher volumetric heat capacity is ideal for small modular reactors (SMRs) and reduces the cost of vessel materials. Thermal conductivity is proportional to the heat transfer capabilities of the salt while viscosity determines how easily the fuel salt circulates through the MSR piping system. The lower the viscosity, the less pressure is required to circulate the fuel-salt mixture and the less likely for pipe clogging to occur. Eutectic fluoride salts, such as LiF–$BeF_2$ and NaF–$BeF_2$, have been reported to have high heat capacities ranging from 2.1-3 $J/(g \cdot K)$. However, their higher melting point and viscosity remain a drawback, particularly the very high viscosity of 22.2 mPa.S for 50-50% LiF–$BeF_2$[8,20]. In contrast, salts consisting of Na and K possess a lower melting point and heat capacity, the latter of which is suboptimal.

The primary coolant and fuel solvent is subjected to high levels of neutron irradiation and hence, must possess radiation stability. Since ionic liquids tend to be resistant to damage by particulate or radiation, molten fluorides and chlorides are suitable choices[21]. During FLiBe salt preparation, natural Li (92.5% Li-7) is enriched to 99.99% Li-7 since the Li-6 isotope produces tritium, a radiation hazard, when irradiated by neutrons[11]. A low neutron capture cross-section for fission is also critical to prevent interference with nuclear fission reactions. Owing to its lower neutron capture cross-section, FLiBe is preferred over FLiNaK as the primary coolant and fuel carrier[12].

### 1.1.4 Materials Selection and Challenges

Currently, the lack of suitable metallic container materials impedes the commercial development and deployment of MSRs. General criteria for container materials in any nuclear application include high temperature, creep, irradiation, and corrosion resistance, as well as low tritium retention[10]. Corrosion resistance becomes especially challenging in molten halide salts, for which the mechanisms governing corrosion are different than those for aqueous environments - in particular, the passivating metal oxide layer that protects alloys from corrosion in aqueous solutions readily dissolves in molten salt[10,22,23]. The attack of the oxide film by the fluoride melt can be described by the following chemical reaction[8],

$$Me_xO_y(s) + yBeF_2(l) \rightarrow xMeF_y(l) + yBeO(s) \quad (1.1)$$

where Me represents a pure alloying element. The metal fluoride products formed ($MeF_y$) in Equation (1.1) subsequently dissolve in the salt, promoting the selective dissolution of elements from the alloy. In addition, the corrosive nature of salts is intensified under the extreme operating temperatures of MSRs ( T $\approx$ 800-1000 K), accelerating the degradation and thinning of containment materials. Another key consideration is that metal dissolution into the salt phase could modify the chemical properties of the salt, including its redox potentials. Thus, structural materials that are resistant to corrosion in water-cooled reactors, including stainless steels and nickel-based alloys, would fail in MSR conditions. The alloy degradation process is known to be driven by the thermodynamics of fluoride formation between the alloying elements and the salt, the presence of salt impurities, galvanic corrosion and metal diffusion along grain boundaries[23–30]. In nickel- and iron-based alloys, corrosion is primarily governed by chromium (Cr) depletion, intensified at grain boundaries. Despite its chemical reactivity, increasing the Cr content of an alloy can improve creep strength at high temperatures and resistance to air oxidation as observed in Hastelloy X[26]. Owing to the higher reduction potential of nickel (Ni), modified Ni-based alloys, particularly Hastelloy N (Ni-6.5Mo-6.9Cr-4.5Fe), have been shown to be more effective against molten salt corrosion at 600-700°C compared to stainless steels. Nonetheless, Hastelloy N lacks the required mechanical strength for high temperature applications[30,31]. Understanding the corrosion mechanisms of alloys in high temperature molten fluoride salts and identifying corrosion-resistant materials is crucial to the development and deployment of molten salt technologies.

## 1.2 Corrosion Processes

### 1.2.1 Thermodynamics of fluoride formation

The chemical reactivity of metals that constitute the containment material in MSRs have an important role in corrosion. The Gibbs free energy of fluoride formation between the alloying elements and salt dictates the susceptibility of the metals to fluoride salt corrosion[25,27–29]. The more negative the Gibbs free energy of metal fluoride formation, the more prone the alloying element to selective depletion from the surrounding alloy matrix and oxidation by the cations of major salt constituents such as Li(I), K(I), and Be(II)[27]. The thermodynamic stability of the fluoride product can be related to the standard reduction potential ($E^o$) of the metal half cell ($M^{n+}/M^n$) with respect to the $F_2/F^-$ reference cell - as $E^o$ becomes more negative, the reduction potential of the metal constituent decreases. Since the reduction potentials of the salt cations such as Li(I) and Be(II) in FLiBe fall substantially below those of structural metals, corrosion of metals by the salt cations is expected to be minimal.

Aluminum (Al), chromium (Cr), titanium (Ti), and manganese (Mn) possess a higher propensity to fluoride attack given their lower reduction potential while refractory metals, niobium (Nb), molybdenum (Mo) and tungsten (W) demonstrate stronger corrosion resistance[26,32]. In the absence of oxygen, the formation of fluorides between the alloying elements and salt constituents can be described by the following chemical reaction[29]:

$$\mathrm{xMe(s) + yMF(l) \rightarrow Me_xF_y(l) + yM(l)} \tag{1.2}$$

where Me is a pure alloying element and M is the cationic component of the salt (Li, Na, K, etc.) which acts as an oxidant in this reaction. Metal fluorides form at the salt-alloy interface with subsequent dissolution of metal ions in the salt, depleting the fluoride-forming elements from the surrounding alloy matrix. The more thermodynamically stable the metal fluoride product, the greater the depletion of the metal constituent from the matrix[28,29]. For instance, Muránsky et al. (2019)[29] determined that the material mass loss of candidate Ni-based alloys in molten FLiNaK at 650°C was correlated with the content

of alloying elements which are electrochemically less noble than Ni.

Under equilibrium conditions, the Gibbs free energy of fluoride formation for the cationic components of the salt should be significantly lower than that of any potential metal fluoride products, limiting corrosion in pure salt conditions[25,26,29]. Despite their thermodynamic instability, trace equilibrium concentrations of metal fluorides are still expected in alkali fluoride melts which increase with temperature[32]. Salt impurities, such as oxygen and water, delay equilibrium between the salt and the alloy, thereby accelerating metal fluoride formation and subsequent metal dissolution into the salt.

### 1.2.2 Impurities

Common corrosive contaminants found in molten salts include water, oxygen, and hydroxides[33]. Given the hygroscopic nature of fluoride salts, water is especially difficult to remove[25,33]. Water introduces $O^{2-}$ into the environment and is much more reactive than oxygen, causing the formation of metal oxide products and hydrofluoric acid (HF) which is prone to corroding metal constituents, as shown in the following chemical reactions[29].

$$\mathrm{xMe(s) + yH_2O(g) \rightarrow Me_xO_y(s) + yH_2(g)} \tag{1.3}$$

$$\mathrm{MF(l) + H_2O(g) \rightarrow MOH(l) + HF(g), HF(g) \rightarrow HF(l)} \tag{1.4}$$

$$\mathrm{xMe(s) + yHF(l) \rightarrow Me_xF_y(l) + \frac{y}{2}H_2(g)} \tag{1.5}$$

In oxygen-rich environments, adherent and corrosion-resistant metal oxide layers, including $Cr_2O_3$, $Fe_2O_3$ and NiO, develop on the alloy surface, acting as a protective barrier to thermodynamically- and impurity-driven attack[34]. However, these oxides are readily soluble in molten halide salts, driving metal dissolution in the salt[34,35]. As the enthalpy of oxide formation decreases, the oxide solubility decreases accordingly[36]. The enthalpy of oxide formation has been observed to decrease with the square of the cation charge divided

by the cation radius, making fluorides more stable for lower charged states (i.e., $Rb^+$, $K^+$ and $Cs^+$) and oxides are more stable for higher charged states (i.e., $Ti^{4+}$, $Zr^{4+}$ and $Al^{3+}$). The relationship between the standard enthalpy of oxide formation and $z^2/r$ is illustrated in Baes (1974)[36].

Significantly, the nobility of metal container materials in molten fluorides decreases in the presence of an oxide, making the metals more susceptible to dealloying. For instance, Baes (1974) found that the electrode potential of various container materials, such as Cr, Mo, Fe and Ni, in $Li_2BeF_4$ at 600°C decreased upon beryllium oxide (BeO) saturation[36]. The most drastic change upon addition of an oxide was observed for Nb which forms a stable oxyion, $NbO_2^+$[36,37].

D'Souza et al. (2021)[38] determined the effect of salt purity on corrosion rate by measuring the mass loss of the Ni-based HAYNES® 230® alloy in molten KCl−$MgCl_2$−NaCl salt at 800°C for 100 hours. Thermal and chemical purification techniques were used to purify the salt of moisture and/or oxygen contaminants. The latter technique involves the addition of magnesium (Mg) to the salt which reduces oxygen content by forming a magnesium oxide (MgO) sludge at the bottom of the crucible. Static corrosion tests were performed inside an SS316L chamber and nickel crucibles containing the HAYNES® 230® specimens submerged in the molten chloride salt. The specimens were analyzed for their weights and dimensions using an analytical balance and a vernier caliper before and after the static corrosion test. D'Souza et al. found that the mass loss was lowest in the thermally and chemically purified salt and highest in the non-purified salt, suggesting that salt purification lowers corrosion rate. Importantly, analysis on corrosion data collected from studies published in 1960-2016 concluded that salt purity was the most significant factor affecting corrosion rates amongst various factors including temperature, sample material, container material, and experimental method[39].

### 1.2.3 Diffusion along Grain Boundaries

In Hastelloy X, Hastelloy N and 316-stainless steel (SS) alloys, Cr dissolution into molten FLiNaK salt was the highest amongst the major metal constituents (Fe, Mo and Ni) and

most prominent in SS316[22]. Pitts developed on the surface of all 3 specimens, advancing into the matrix along the grain boundary and serving as preferred sites for $Cr_2O_3$ deposition. In alloys containing high Cr content - Hastelloy X and SS316 - both initial and subsequent corrosion stages were dominated by $Cr_2O_3$ formation and dissolution at the surface. In Hastelloy N, which had lower Cr content, the initial oxidation phases were governed by Cr diffusion from the inner matrix, which occurs preferentially along grain boundaries. Alloys with a larger grain size and twin boundaries have been shown to be more resistance to intragranular corrosion[29]. Intragranular corrosion can occur via Cr dissolution in the form of $CrF_x$ species or Cr transport to localized $F^-$ concentrations[40]. In the later phases of oxidation, the Cr dissolution rate into FLiNaK dominates, evidenced by long-term $Cr_2O_3$ loss between grain boundary sites. Hence, the corrosion mechanism is affected by Cr content of alloys and the grain boundary density.

Cr is oxidized by hydrofluoric acid (HF) into $Cr^{2+}$ or $Cr^{3+}$ as a result of moisture ingress, a spontaneous process except in certain combinations of hydrogen partial pressure and/or HF activities[41]. $CrF_3$, in particular, lowers the energy barrier to Cr dissolution at the grain boundaries[40]. Cr has also been found to promote stronger F adsorption on the surface compared to Ni, which in turn facilitates Cr surface segregation[42].

## 1.3 High Entropy Alloys as Alternative Materials

### 1.3.1 Background

Since the Bronze Age, improvements in material properties have traditionally been achieved by mixing a primary element with small amounts of secondary elements, referred to as "alloying"[43]. For instance, iron-based alloys are doped with carbon and chromium to improve strength and corrosion resistance, respectively. However, the conventional alloying approach limits the compositional space, much of which has already been explored. Expanding the possible element combinations to fine-tune alloy properties requires an alternative approach.

In binary alloy phase diagrams, solid solutions are typically found at the pure-element ends, while ordered intermetallics fall in the middle[44]. In general, there is a maximum amount of solute that can be incorporated into the base metal solution after which a distinct secondary phase will form upon solidification[45]. This causes the formation of a crystal with an ordered atomic arrangement, also known as an intermetallic, which is generally hard and brittle. As the number of elements in a mixture increases, the number of possible intermetallics that can form between element pairs upon solidification also increases, as well as the possibility of ternary intermetallics[43]. Hence, this counterintuitive notion has long deterred metallurgists from the exploration of multi-element alloys.

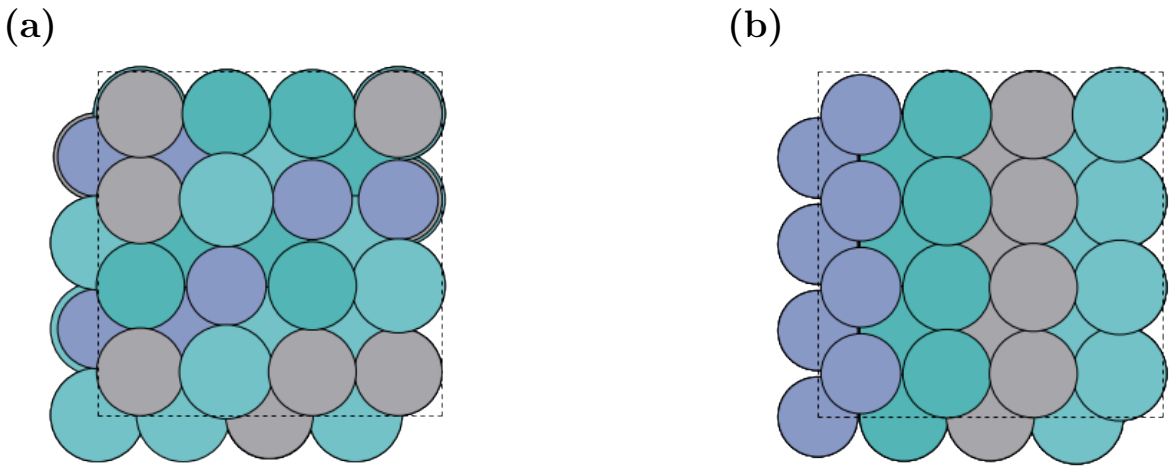



Figure 1.2: Simplified atomic distribution in a (a) solid solution and (b) intermetallic.

In the early 2000s, Taiwanese scientist Jien-Wei Yeh[46] proposed that combining multiple elements in a near equimolar solution would increase the entropy of mixing such that the solid solution state competes with intermetallic formation. In statistical mechanics:

$$\Delta S_{mix} = -R \sum_{i=1}^{N} x_i \ln(x_i) \tag{1.6}$$

where $\Delta S_{mix}$ is the mixing entropy, R is the ideal gas constant, and $x_i$ is the mole fraction of the $i^{th}$ element. In an equimolar alloy, $x_i$ is equal for all N constituent elements, and the mixing entropy becomes proportional to the number of different elements:

$$\Delta S_{mix} = n \cdot \ln(n) \tag{1.7}$$

At the melting temperature, $T_m$, if the Gibbs free energy of mixing is more negative than the free energies of formation of all possible $A_iB_j$-type intermetallics, a solid solution will form. In contrast, $A_iB_j$-type intermetallic compound formation may be more favorable in certain conditions. The free energy calculations are as follows for an A + B = AB stoichiometry,

$$\Delta G_{mix} = \Delta H_{mix} - T_m \Delta S_{mix} \tag{1.8}$$

$$\Delta G_f = \Delta H_f - T_m \Delta S_f \tag{1.9}$$

where $\Delta G_{mix}$ is the Gibbs free energy of mixing, $\Delta H_{mix}$ is the mixing enthalpy and $\Delta S_{mix}$ is the mixing entropy while $\Delta G_f$, $\Delta H_f$ and $\Delta S_f$, are the Gibbs free energy, enthalpy and entropy of compound formation, respectively. Assuming a completely random (ideal) solid solution ($\Delta H_{mix} = 0$) and a perfectly ordered intermetallic ($\Delta S_f = 0$), the Gibbs free energy of mixing and intermetallic formation can be further simplified:

$$\Delta G_{mix} = -T_m \Delta S_{mix} \tag{1.10}$$

$$\Delta G_f = \Delta H_f \tag{1.11}$$

For 5 or more constituent elements and/or at high temperatures, the contribution of mixing entropy to the free energy may exceed that of the formation enthalpies of all intermetallic compounds, shifting the equilibrium toward single-phase solid solution formation. The term "high entropy alloys" was thus coined, defining alloys with at least 5 principal elements with concentrations between 5 and 35%, that form random solid solutions. However, it was eventually confirmed that configurational entropy is not the sole contributor to solid solution formation in multi-component alloys; mixing enthalpy and non-configurational entropy are additional factors governing phase stability which were neglected in Equation (1.11)[47]. In practice, many multi-component alloys exhibited several intermetallic phases

after annealing at high temperatures[47–49]. Moreover, certain multi-component alloys that form solid solutions at higher temperatures dissociate when annealed at lower temperatures. The original HEA criterion established by Yeh et al.[46] later extended to encompass 4-component alloys capable of forming enthalpy-stabilized solid solutions.

The first single-phase solid solution of a multi-element, equiatomic alloy was observed for face-centered cubic (FCC) CoCrFeMnNi by Cantor et al.[48] after induction melting. Interestingly, they found that equimolar alloys made of 16 and 20 elements form multi-phase, crystalline, and brittle structures with their main FCC phase constituting Co, Cr, Fe, Mn, and Ni. This reinforces the notion that there are factors beyond configurational entropy that determine solid solution formation. Otto et al.[47] extended the work of Cantor et al.[48] by incrementally replacing individual elements in the FCC CoCrFeMnNi alloy with others of similar size/electronegativity to prepare new equimolar, quinary alloys and test the hypothesis that solid solution formation is governed by configurational entropy. Only the base CoCrFeMnNi alloy formed a stable single-phase crystal, affirming the effect of competing driving forces favoring secondary phase formation[47]. Troparevsky et al.[49] later proposed a model that reliably predicts elemental combinations that form multi-element, single-phase solid solutions using high-throughput computations of formation enthalpies of binary compounds made of constituent elements and constructing a 30 x 30 matrix. They identified a specified range in which the formation enthalpies of all possible binary compounds must fall, in order for the corresponding solid solution to be stabilized. An overly stable compound may cause that phase to precipitate out of the mixture, while a high degree of instability suggests the immiscibility of that group of elements. Considering the formation enthalpies of competing intermetallics can guide the screening of compositional subspaces for regions where single phases are more likely to be stable. The limitations of preliminary experimental techniques used to investigate phase stability of HEAs merit further evaluation. For instance, X-ray diffraction (XRD) is frequently the sole method of characterizing microstructural states of multi-component alloys, despite its low resolution.

The advantage of high entropy alloys (HEAs) over standard alloys is the large compositional space, which enables better fine-tuning of mechanical and thermophysical properties

via adjustment of chemical and molar composition. Many HEAs exhibit superior properties such as high thermal stability, hardness, strength, creep, and corrosion resistance, making them prospective materials for use in the harsh conditions of Generation IV MSRs[43,50]. HEAs are distinguished by four core effects that impart their desirable properties: severe lattice distortion, sluggish diffusion, high configurational entropy, and the cocktail effect[51]. Lattice distortion and sluggish diffusion are correlated with enhanced neutron swelling resistance and phase stability, as well as lower point defect mobility, observed in HEAs compared to standard alloys[52,53].

HEAs primarily made of refractory metals have gained recent interest owing to their great resistance to heat and wear. Certain refractory high entropy alloys (RHEAs) have been shown to be more oxidation resistant than others which may be attributed to the greater stability of Mo and Nb in corrosive substances[32]. Of particular interest are body-centered cubic (BCC) NbTaMoW and NbTaMoWV, first synthesized by Senkov et al.[54] via vacuum arc-melting. Both RHEAs formed a simple and disordered BCC crystal structure at 1400°C, exceeding the temperature limits (1200°C) of nickel-based superalloys used in high-temperature applications[55]. The reported compressive strength of NbTaMoW was 1211 MPa at room temperature and 405 MPa at 1600°C. The addition of V to NbTaMoW maintained the single-phase BCC structure and even enhanced the compressive strength, rendering both RHEAs suitable for high temperature applications.

### 1.3.2 Corrosion Investigations

Preliminary studies on the corrosion behavior of HEAs in aqueous conditions have demonstrated that HEAs exhibit enhanced corrosion resistance compared to standard steels[50,56]. This behavior is attributed to the distinct dissolution and passivation mechanism of HEAs, synergistic effect of multiple principal components and locally random chemical arrangement[50,56,57]. Simple and disordered solid solutions tend to facilitate the growth of a single and continuous passive film that protects against corrosion in aqueous solutions[50]. One of the earliest investigations was carried out by Chen et al.[57] who observed a lower corrosion rate for $Cu_{0.5}$NiAlCoCrFeSi in $H_2SO_4$ and NaCl solutions compared to austenitic

stainless steel (304SS). Later, Qiu et al.[58] examined the corrosion and pitting potential ($E_{corr}$ and $E_{pit}$) of 20 unique HEAs in 0.6 M NaCl while also documenting a galvanic series. The $E_{corr}$ values of HEAs were comparable to those of austenitic and stainless ferric steels, with HEAs containing Co, Cr and Ni exhibiting even lower nobility than austenitic stainless steel. Corrosion resistance of HEAs was shown to vary with elemental composition[58], prompting further investigation into the effects of different constituent elements on corrosion resistance[56].

Despite the lower density and enhanced mechanical strength conferred by HEAs synthesized with Al, it has shown to preferentially deplete from solid solutions in aqueous environments due to its lower reduction potential[59]. Both Cr and Ti are known to form the most stable passivating oxide films in aqueous conditions[50], however, Ti is prone to precipitating out from the solid solutions and forming intermetallic compounds[60]. At concentrations exceeding 12%, Cr promotes passivation in HEAs via $Cr_2O_3$ film formation, thereby slowing the corrosion process[61]. Mo strengthens the passivity and pitting resistance of austenitic stainless steels, however, has been found to develop sigma phases in HEAs[62]. Incorporating Ni into stainless steels stabilizes the ductile FCC structure and improves corrosion resistance, yet its small atomic radius may lead to high lattice distortion in HEAs, compromising the microstructure[63]. Furthermore, when examining the corrosion characteristics of $FeCoNiCrCu_x$ in a solution of 3.5% NaCl, Hsu et al.[64] observed that an increase in Cu content increases the preferential depletion of Cu along the interdentrites.

Much of previous corrosion research on HEAs concentrates on aqueous environments which are distinct from molten salts. Similar to the corrosion behavior observed in standard iron- and nickel- based alloys, the passivating oxide films that confer stability of HEAs in aqueous conditions become unstable in molten halide salts. Thus, recent investigations have shifted the focus to understanding the complex mechanisms governing corrosion of HEAs in halide salts. Elbakhshwan et al.[65] found that FCC $Cr_{18}Mn_{27}Fe_{27.5}Ni_{27.5}$ exhibited higher mass loss compared to reference 316 H stainless steel in FLiBe salt at 700 °C for 1000 hours due to selective depletion of the least noble constituent element, Mn, and dissolution of the protective $Cr_2O_3$ layer into the salt. Its lower reduction potential and higher diffusion

coefficient may have prompted higher Mn dissolution compared to Cr. However, Cr was retained in the alloy, refuting the notion that Cr is the most chemically active element and undergoes selective leaching. The work of Elbakhshwan et al.[65] could be extended by tuning the elemental and molar compositions of the HEA to preserve structural integrity and augment oxidation resistance.

Computational studies have been leveraged to elucidate the complex, atomic-level corrosion mechanisms in molten fluoride salts, such as diffusion and surface reactions between metal and fluorine atoms, which may be difficult to accomplish via experimentation. Arkoub et al.[40] parameterized a ReaxFF force field for the FLiNaK–NiCr interface which was subsequently used in classical molecular dynamics simulations to model the dynamic chemical reactions at the interface. Strong Cr–F bonding was observed as well as a significantly greater dissolution of Cr metal ions relative to Ni over time, reinforcing that Cr increases susceptibility to corrosion in fluoride salts. Furthermore, Schneider et al.[66] employed ab initio molecular dynamics to investigate the impact of moisture on the atomistic corrosion of FeCr alloys in molten salts. Their results underscore the high stability of $H_2O$ in molten salts with occasional partial dissociation of $H_2O$ at the salt-metal interface, especially in fluoride salts, which occurs sequentially rather than simultaneously.

The objective of this research is to gain insight into the corrosion mechanisms of two body-centered cubic (BCC) refractory high-entropy alloys, NbTaMoW and NbTaMoWV, in a high-temperature, molten 66-34 mol% LiF–$BeF_2$ (FLiBe) environment using first-principles methodologies, specifically density functional theory (DFT) and Ab Initio Molecular Dynamics (AIMD)[67]. Electronic analyses is conducted on periodic snapshots from the AIMD simulation, such as the density of states (DOS), crystal orbital Hamilton population (COHP) analyses and electron localization function (ELF), to elucidate the electronic stability, metal-salt interfacial bonding, and redox reactions. As one of the earliest atomistic studies of the corrosion behavior of HEAs in molten salts, it examines the preliminary stages of advanced material degradation.

# Chapter 2

# Methodology

## 2.1 Classical Molecular Dynamics

### 2.1.1 Particle Dynamics

In the realm of classical physics, an atom is mathematically treated as a classical particle or "point mass" attributed a position vector $\mathbf{r} = (x, y, z)$ and a velocity vector $\mathbf{v} = (v_x, v_y, v_z)$ in Cartesian coordinates at an instant of time. Classical particles are subject to Newton's laws of motion, the second law which stipulates that the force vector $\mathbf{F}$ on an atom of mass $m$, is directly proportional to the acceleration vector $\mathbf{a}$,

$$\sum \mathbf{F} = m \cdot \mathbf{a} \tag{2.1}$$

where $\sum \mathbf{F}$ is the sum of all forces acting on the atom. $\mathbf{F}$ and $\mathbf{a}$ also have Cartesian components, $x$, $y$, and $z$.

$$\sum F_x = m \cdot a_x \quad \sum F_y = m \cdot a_y \quad \sum F_z = m \cdot a_z \tag{2.2}$$

For a conservative system containing a total of $N$ atoms, the total force on the $i_{th}$ atom is the sum of all the force vectors exerted on the $i_{th}$ atom by its neighboring atoms

indexed by $j = 1, ..., N$ with $j \neq i$. Summing over all particles[68–70],

$$\sum_{j>i}^{N}\sum_{i=1}^{N}\mathbf{F}_{ji} = \sum_{i=1}^{N}\mathbf{F}_i = \sum_{i=1}^{N} m_i \cdot \mathbf{a}_i = -\sum_{j>i}^{N}\sum_{i=1}^{N}\frac{\partial U}{\partial r}(r_{ji}) \cdot \frac{\mathbf{r}_j - \mathbf{r}_i}{r_{ji}} \tag{2.3}$$

where $r_{ji} = |\mathbf{r}_j - \mathbf{r}_i|$ and $U(r_{ji})$ is the potential energy between atom $j$ and atom $i$. The magnitude of force, $F_{\text{mag},ji}$, that atom $j$ exerts on atom $i$ is calculated by the negative derivative of the potential energy with respect to the interatomic distance $r$,

$$F_{\text{mag},ji} = -\frac{\partial U}{\partial r}(r_{ji}) \tag{2.4}$$

The potential energy function is predefined; it should be chosen such that it accurately describes the interatomic interactions in a system. In classical molecular dynamics, it is common practice to use semi-empirical potentials such as the Leonard Jones potential. The magnitude of force, $F_{\text{mag},ji}$, is computed between each (j, i) atom pair, and the Cartesian force components $F_{x,ji}$, $F_{y,ji}$ and $F_{z,ji}$ are calculated by multiplying $F_{\text{mag},ji}$ by the unit vector in each Cartesian direction:

$$F_{x,ji} = F_{\text{mag},ji} \cdot \frac{x_j - x_i}{|\mathbf{r}_j - \mathbf{r}_i|} \quad F_{y,ji} = F_{\text{mag},ji} \cdot \frac{y_j - y_i}{|\mathbf{r}_j - \mathbf{r}_i|} \quad F_{z,ji} = F_{\text{mag},ji} \cdot \frac{z_j - z_i}{|\mathbf{r}_j - \mathbf{r}_i|} \tag{2.5}$$

According to Newton's third law of motion, the force exerted by atom $j$ on atom $i$ is equal in magnitude but opposite in direction to the force exerted by atom $i$ on atom $j$. This is considered in the numerical algorithm for force computations when looping over atom arrays.

$$\mathbf{F}_{ji} = -\mathbf{F}_{ij} \tag{2.6}$$

where the force vector $\mathbf{F}_{ji} = (F_{x,ji}, F_{y,ji}, F_{z,ji})$. The acceleration of the $i_{th}$ atom is thus computed by dividing the sum of all forces exerted by neighboring atoms on the $i_{th}$ atom by the mass of the $i_{th}$ atom,

$$m_i \cdot \mathbf{a}_i = \sum_{\substack{i=1 \\ j \neq i}}^{N} \mathbf{F}_{ji} \tag{2.7}$$

### 2.1.2 Velocity Verlet Algorithm

The initial atomic forces and accelerations are computed with Equation (2.7) from the initial position coordinates of a system. The initial acceleration is subsequently applied to Newton's classical equations of motion to determine the updated position of the $i_{th}$ atom after a specified timestep $\Delta t$ chosen to be sufficiently small[69,71],

$$\mathbf{r}_i(t + \Delta t) = \mathbf{r}_i(t) + \mathbf{v}_i(t)\Delta t + \frac{1}{2}\mathbf{a}_i(t)\Delta t^2 \tag{2.8}$$

The smaller the $\Delta t$ value, the less drastic the changes in the computed atomic forces at the updated position coordinates[71]. $\Delta t$ is typically set to approximately $10^{-15}$ seconds, or alternatively, $10^{-3}$ picoseconds, to ensure adequate accuracy. While larger time steps speed up the dynamics, they may compromise the accuracy of the calculated interatomic forces. The updated position computed by Equation (2.8) is thereafter used to calculate the updated acceleration of the $i_{th}$ atom after a timestep of $\Delta t$ using Equation (2.7). The average acceleration based on the current and updated positions is subsequently used to compute the updated velocity after a timestep of $\Delta t$,

$$\mathbf{v}_i(t + \Delta t) = \mathbf{v}_i(t) + \frac{1}{2}[\mathbf{a}_i(t) + \mathbf{a}_i(t + \Delta t)]\Delta t \tag{2.9}$$

Equation (2.8) is then modified to include the updated acceleration and velocity, and the entire process is repeated for a given number of timesteps. To compute the system dynamics accordingly, the initial positions and velocities of all $N$ atoms must be known. Hence, the accuracy of the Velocity Verlet algorithm is heavily dependent on the accuracy of the initial atomic configuration - if it differs substantially from the equilibrium one, a longer simulation time will be needed for the system to reach equilibrium, if reached at all.

Assuming that the total energy, $E$, of the system is conserved[70],

$$\frac{\partial E}{\partial t} = 0 = \frac{\partial K}{\partial t} + \frac{\partial U}{\partial t} \quad \frac{\partial K}{\partial r} = -\frac{\partial U}{\partial t} \tag{2.10}$$

where $K$ is the kinetic energy and $U$ is the potential energy of the system. Substituting in the expression for $K$,

$$\frac{1}{2} m_i \cdot \frac{\partial \mathbf{v}_i^2}{\partial t} = -\frac{\partial U}{\partial t} \tag{2.11}$$

$$\frac{1}{\cancel{2}} m_i \cdot \cancel{2} \mathbf{v}_i \frac{\partial \mathbf{v}_i}{\partial t} = -\frac{\partial U}{\partial t} \tag{2.12}$$

$$\mathbf{F}_i = m_i \mathbf{a}_i = -\frac{\partial U}{\partial t} \cdot \frac{1}{\mathbf{v}_i} \tag{2.13}$$

$$\mathbf{F}_i = m_i \mathbf{a}_i = -\frac{\partial U}{\cancel{\partial t}} \cdot \frac{\cancel{\partial t}}{\partial r} = -\frac{\partial U}{\partial r} \tag{2.14}$$

and where $m_i$, $\mathbf{v}_i$ and $\mathbf{a}_i$ denotes the mass, velocity vector and acceleration vector of atom $i$. Thus, the interatomic forces calculated in Equation (2.3) automatically generate a microcanonical ($NVE$) ensemble for which the particle number, volume, and energy remain constant. To simulate an $NVE$ ensemble, the initial particle velocities are either scaled to the desired kinetic energy or set to zero.

### 2.1.3 Nosé–Hoover Thermostat

In the canonical ($NVT$) ensemble, the particle number, volume, and temperature remain constant. To model systems at a fixed temperature, velocity scaling and heat-bath coupling methods are introduced.

Simple velocity scaling is typically employed to scale the initial particle velocities to the desired temperature prior to time integration. The particle velocities are initialized by sampling random numbers from a specified distribution, such as a uniform and Gaussian

distribution, and subsequently scaling the initial velocities to the desired temperature of the system. For reproducing the molecular simulation, a random seed is used to initialize the velocities prior to scaling, resulting in the same initial velocities each time. According to the kinetic theory of gases, the approximation of the actual temperature $T_A$ for the ensemble at an instant of time is correlated with the average kinetic energy $\langle KE \rangle$ of the $N$-particle system as follows[69],

$$T_A = \frac{2\langle KE \rangle}{3k_B} = \frac{1}{3Nk_B} \left\langle \sum_{i=1}^{N} m_i \mathbf{v}_i \cdot \mathbf{v}_i \right\rangle \tag{2.15}$$

where $k_B$ is the Boltzmann constant. Consequently, the initial particle velocities can be adjusted to the desired temperature $T_D$ using the following relation,

$$v_{ix}^{new} = v_{ix}\sqrt{\frac{T_D}{T_A}} \quad v_{iy}^{new} = v_{iy}\sqrt{\frac{T_D}{T_A}} \quad v_{iz}^{new} = v_{iz}\sqrt{\frac{T_D}{T_A}} \tag{2.16}$$

The simplest approach to maintaining a constant temperature through out the simulation is to periodically re-scale the velocities to the desired temperature using Equation (2.16). However, a more rigorous strategy is to couple the system to an external heat-bath at the desired temperature. The heat bath supplies heat to the system or removes heat from the system in order to simulate an $NVT$ ensemble. A common heat-bath coupling method is the Nosé–Hoover thermostat[72] which modifies Newton's equations of motion with a fictitious dynamic variable $\zeta$, analogous to a friction coefficient[69,71],

$$m_i \mathbf{a}_i = \mathbf{F}_i - \zeta m_i \mathbf{v}_i \tag{2.17}$$

The particle velocities are periodically adjusted until the actual temperature reaches the desired temperature. According to the equipartition function, $\zeta$ is correlated with the user-defined effective mass, $Q$, which dictates how strongly the temperature is coupled to the thermostat heat bath[71],

$$\frac{d\zeta(t)}{dt} = \frac{1}{Q}\left[\sum_{i=1}^{N} \frac{m_i \mathbf{v}_i^2}{2} - \frac{3N+1}{2} k_B T_D\right] \tag{2.18}$$

As $Q$ approaches infinity, the behavior of the system tends toward $NVE$[73]. It can be inferred that a larger $Q$ value diminishes the coupling to the heat bath, leading to smaller fluctuations in the kinetic energy and temperature with time. A smaller $Q$ strengthens the coupling, resulting in larger fluctuations in the kinetic energy and temperature with time. $Q$ is empirically determined for the system of interest such that equilibrium is obtained in a reasonable number of timesteps. The default $Q$ value generally suitable for most systems is $100 \cdot \Delta t$ where $\Delta t$ is the timestep. Using Equation (2.17) to solve for modified $\mathbf{a}_i$ and substituting it into Equation (2.8), the modified Velocity Verlet algorithm becomes[71],

$$\mathbf{r}_i(t + \Delta t) = \mathbf{r}_i(t) + \mathbf{v}_i(t)\Delta t + \frac{1}{2}\left(\frac{\mathbf{F}_i(t)}{m_i} - \zeta(t)\mathbf{v}_i(t)\right)\Delta t^2 \tag{2.19}$$

$$\mathbf{v}_i(t + \frac{\Delta t}{2}) = \mathbf{v}_i(t) + \frac{\Delta t}{2}\left(\frac{\mathbf{F}_i}{m_i} - \zeta(t)\mathbf{v}_i(t)\right) \tag{2.20}$$

$$\zeta(t + \frac{\Delta t}{2}) = \zeta(t) + \frac{\Delta t}{2Q}\left[\sum_{i=1}^{N}\frac{m_i\mathbf{v}_i(t)^2}{2} - \frac{3N+1}{2}k_BT_D\right] \tag{2.21}$$

$$\zeta(t + \Delta t) = \zeta(t + \frac{\Delta t}{2}) + \frac{\Delta t}{2Q}\left[\sum_{i=1}^{N}\frac{m_i\mathbf{v}_i(t + \frac{\Delta t}{2})^2}{2} - \frac{3N+1}{2}k_BT_D\right] \tag{2.22}$$

$$\mathbf{v}_i(t + \Delta t) = \frac{\left[\mathbf{v}_i(t + \frac{\Delta t}{2}) + \frac{\Delta t}{2}\frac{\mathbf{F}_i(t+\Delta t)}{m_i}\right]}{1 + \frac{\Delta t}{2}\zeta(t + \Delta t)} \tag{2.23}$$

where $\zeta$ is initially set to 0[69]. The updated acceleration is computed using the latest calculated velocity.

## 2.2 Density Functional Theory

### 2.2.1 The Many-Body Problem

The wavefunction $\psi$ describing a three-dimensional system composed of $N$ quantum particles can be expressed as $\psi(\mathbf{r}_1, \mathbf{r}_2, ..., \mathbf{r}_N)$ where $\mathbf{r}_i$ represents the position coordinates of the $i^{th}$ particle[74]. If the $N$-particle wavefunction is known, then the static energy of the quantum system can be solved using the time-independent, non-relativistic Schrödinger equation[75],

$$\hat{H}\,\psi(\mathbf{r}_1, \mathbf{r}_2, ..., \mathbf{r}_N) = E\,\psi(\mathbf{r}_1, \mathbf{r}_2, ..., \mathbf{r}_N) \tag{2.24}$$

In the Born-Oppenheimer approximation, the wavefunction is written as a function of both electron and nuclear position coordinates, $\mathbf{r}_i$ and $\mathbf{R}_A$, respectively. Since nuclei are considerably larger than electrons and thus move much slower than their counterparts, they are treated as classical particles fixed at instantaneous atomic coordinates. By making this assumption, the Schrödinger equation becomes[75],

$$\hat{H}\,\psi(\mathbf{r}_i, \mathbf{R}_A) = E\,\psi(\mathbf{r}_i, \mathbf{R}_A) \tag{2.25}$$

The total wavefunction, $\psi(\mathbf{r}_i, \mathbf{R}_A)$, can be separated into a wave component for electrons $\psi_{elec}$ and a wave component for nuclei $\psi_{nuc}$,

$$\psi(\mathbf{r}_i, \mathbf{R}_i) = \psi_{elec}(\mathbf{r}_i) \cdot \psi_{nuc}(\mathbf{R}_A) \tag{2.26}$$

By invoking the fourth postulate of quantum mechanics, the total energy of the system is computed through the addition of the electronic energy and nuclear energy,

$$E_{total} = E_{elec} + E_{nuc} \tag{2.27}$$

According to Fermi-Dirac statistics, electrons are non-interacting, indistinguishable

particles and therefore, $\psi_{elec}$ must be anti-symmetric upon the exchange of two electron coordinates[74]. An approximation to the $N$-electron wavefunction can be expressed as a single Slater determinant of a matrix of one-electron spin orbitals, $\chi_i(\mathbf{x}_i)$. In addition to the position coordinates of electron $i$, the vector $\mathbf{x}_i$ now contains an additional term - its spin state - which can be either up or down. Using a 2-electron wavefunction as an example where $\frac{1}{\sqrt{2}}$ is the normalization constant,

$$\psi(\mathbf{x}_1, \mathbf{x}_2) = \frac{1}{\sqrt{2}} \left[\chi_1(\mathbf{x}_1)\chi_2(\mathbf{x}_2) - \chi_2(\mathbf{x}_1)\chi_1(\mathbf{x}_2)\right] \tag{2.28}$$

it becomes clear that there is an equal probability that electron $\mathbf{x}_1$ is located in orbital $\chi_1$ and $\chi_2$. For an $N$-electron system, the normalization constant is $\frac{1}{\sqrt{N}}$. The Slater determinant is a systematic approach to formalizing the anti-symmetry principle and enforcing the Pauli-exclusion principle by reducing to zero if the same two electrons reside in the same orbital. Each one-electron spin orbital in the Slater determinant can be specified as a linear combination of basis functions $\phi_i(\mathbf{r})$, also known as a basis set,

$$\chi_j(\mathbf{x}) = \sum_{i=1}^{K} c_{j,i}\phi_i(\mathbf{x}) \tag{2.29}$$

where $c_{j,i}$ are the expansion coefficients for $i = 1, ..., K$ and $j = 1, ..., N$. All basis functions must be orthogonal to each other.

Revisiting Equation (2.24), the total Hamiltonian $\hat{H}$ is the sum of kinetic ($\hat{T}$) and potential ($\hat{V}$) energy operators which are further decomposed into the electron and nuclei kinetic terms and into the repulsive and attractive Coloumbic interactions, respectively[68],

$$\hat{H} = \hat{T}_e + \hat{T}_n + \hat{V}_{ee} + \hat{V}_{nn} + \hat{V}_{ne} \tag{2.30}$$

The kinetic energy operator for electrons $\hat{T}_e$ is expressed as

$$\hat{T}_e = -\frac{\hbar^2}{2m_e} \sum_{1=1}^{N_e} \nabla_i^2 \tag{2.31}$$

where $\hbar$ is Planck's constant, $m_e$ is the electron mass and $N_e$ is the total number of electrons. The kinetic energy operator for nuclei is expressed as

$$\hat{T}_n = -\frac{\hbar^2}{2} \sum_{A=1}^{N_n} m_n \nabla_A^2 \tag{2.32}$$

where $N_n$ is the total number of nuclei and $m_n$ is the mass of the nuclei. The Coloumbic attraction between electrons and nuclei, $\hat{V}_{en}$, is given by

$$\hat{V}_{en} = -\sum_{i=1}^{N_e} \sum_{A=1}^{N_n} \frac{Z_A e}{4\pi\epsilon_0 |\mathbf{r}_i - \mathbf{R}_A|} \tag{2.33}$$

where $Z_A$ is the charge of the $A_{th}$ nucleus, $e$ is the magnitude of charge of a single electron, $\epsilon_0$ is the vacuum electric permittivity, and $\mathbf{r}_i$ and $\mathbf{R}_A$ are the position vectors of the $i_{th}$ electron and $A_{th}$ nuclei, respectively. The Coloumbic repulsion between electrons is given by

$$\hat{V}_{ee} = \sum_{i<j}^{N_e} \frac{e^2}{4\pi\epsilon_0 \, |\mathbf{r}_i - \mathbf{r}_j|} \tag{2.34}$$

and the Coloumbic repulsion between nuclei is given by

$$V_{nn} = \sum_{A<B}^{N_n} \frac{Z_A Z_B}{4\pi\epsilon_0 \, |\mathbf{R}_A - \mathbf{R}_B|} \tag{2.35}$$

The attractive and repulsive energy contributions are characterized by a negative and positive sign, respectively. The Bohn-Oppenheimer approximation neglects the nuclear kinetic energy due to the treatment of nuclei as stationary particles. Simplifying the expressions by setting $\hbar$, $m_e$, $e$ and $\epsilon_0$ to unity, the total Hamiltonian in Equation (2.30) becomes

$$\hat{H} = -\frac{1}{2} \sum_{i=1}^{N_e} \nabla_i^2 - \sum_{i=1}^{N_e} \sum_{A=1}^{N_n} \frac{Z_A}{|\mathbf{r}_i - \mathbf{R}_A|} + \sum_{i<j}^{N_e} \frac{1}{|\mathbf{r}_i - \mathbf{r}_j|} + \sum_{A<B}^{N_n} \frac{Z_A Z_B}{|\mathbf{R}_A - \mathbf{R}_B|} \tag{2.36}$$

The corresponding Schrodinger equation (2.24) becomes,

$$\left[-\frac{1}{2}\sum_{i=1}^{N_e}\nabla_i^2 - \sum_{i=1}^{N_e}\sum_{A=1}^{N_n}\frac{Z_A}{|\mathbf{r}_i-\mathbf{R}_A|} + \sum_{i\neq j}^{N_e}\frac{1}{|\mathbf{r}_i-\mathbf{r}_j|} + \sum_{A<B}^{N_n}\frac{Z_A Z_B}{|\mathbf{R}_A-\mathbf{R}_B|}\right]\psi(\mathbf{r}_1,...,\mathbf{r}_N) = E\psi(\mathbf{r}_1,...,\mathbf{r}_N) \tag{2.37}$$

where the electronic wavefunction $\psi$ is a function of all the position coordinates corresponding to $N$ electrons.

### 2.2.2 Kohn-Sham self-consistent field

The fundamental problem with Equation (2.37) is that the electronic wavefunction has $3N$ variables, thereby producing an inherently complex calculation[74]. Hohenberg and Kohn proposed that the ground-state energy $E_0$ from the Schrodinger equation can be expressed as a functional of the electron density, $\rho(\mathbf{r})$[75]. The Schrodinger equation (2.37) is thereby modified so that the electron density $\rho(\mathbf{r})$ replaces $\psi(\mathbf{r}_1,...,\mathbf{r}_N)$ as the eigenfunction and an additional effective potential term is incorporated,

$$E[\rho(\mathbf{r})] = T_e[\rho(\mathbf{r})] + V[\rho(\mathbf{r})] + V_H[\rho(\mathbf{r})] + V_{XC}[\rho(\mathbf{r})] \tag{2.38}$$

where the first term is the electron kinetic energy and the succeeding three terms are the electron-nuclei attractive term, the Hartree potential defining electron-electron interactions and and the exchange-correlation term. $\rho(\mathbf{r})$ is defined by

$$\rho(\mathbf{r}) = 2\sum_{i=1}^{N}\psi_i^*(\mathbf{r})\psi_i(\mathbf{r}) \tag{2.39}$$

where the term inside the summation in Equation (2.39), $\psi_i^*(\mathbf{r})\psi_i(\mathbf{r})$, defines the probability that an electron in wavefunction $\psi_i$ is found at the given position coordinates, $\mathbf{r}$. The factor of 2 preceding the summation satisfies the Pauli exclusion principle, which stipulates that 2 electrons of opposite spins can occupy an individual electron wavefunction.

This formulation reduces the number of dimensions from $3N$ to 3, thereby rendering the solution to the Schrodinger equation more tractable. Hohenberg and Kohn proceeded to develop a second theorem stating that the ground-state electron density is the electron density that minimizes the energy functional. If the general form of the energy functional is known, then the electron density could be systematically varied until the energy functional reaches a local minimum. These two Hohenberg and Kohn theorems coined the density functional theory (DFT).

In DFT, the electronic energy functional is a sum of two known contributions - the electron-nuclei electrostatic attraction and the electron-electron electrostatic repulsion - as well as two unknown terms - the electron kinetic energy and the exchange-correlation energy, $V_{XC}$,

$$E[\rho(\mathbf{r})] = -\frac{\hbar^2}{m}\sum_i \int \psi_i^* \nabla \psi_i d^3r + \int V(\mathbf{r})\rho(\mathbf{r})d^3r + \frac{e^2}{2}\int\int \frac{\rho(\mathbf{r})\rho(\mathbf{r}')}{|\mathbf{r}-\mathbf{r}'|}d^3r d^3r' + V_{XC}[\rho(\mathbf{r})] \tag{2.40}$$

which describes the exchange of same-spin electrons amongst different orbitals. The exact form of the $V_{XC}$ is unknown, however, it is currently approximated by various numerical methods such as the local density approximation (LDA) and the generalized gradient approximation (GGA), one of which is the Perdew-Burke-Ernzerhof (PBE)[76]. To further simplify the solution for the energy functional, Kohn and Sham established a single-electron equation modeling a non-interacting reference system,

$$\left[-\frac{\hbar^2}{m}\nabla^2 + V(\mathbf{r}) + V_H(\mathbf{r}) + V_{XC}(\mathbf{r})\right]\psi_i(\mathbf{r}) = \epsilon_i \psi_i(\mathbf{r}) \tag{2.41}$$

Equation (2.41) can be used to identify the individual wavefunctions in the electron density function defined in Equation (2.39) that depend on only three spatial variables, $\mathbf{r} = (x, y, z)$. To solve the Kohn-Sham equations, an iterative algorithm is implemented.

1. Estimate a trial electron density function, $\rho(\mathbf{r})$. If starting a DFT calculation from scratch, $\rho(\mathbf{r})$ is initialized by superimposing the electron densities for each isolated

atom.

2. Define the potential terms, $V_H$ and $V_{XC}$, in the Kohn-Sham equation (2.41) in terms of the trial electron density. Solve for the optimal individual wavefunctions using the variational principle and the orthonormality constraint.

3. Use the electron wavefunctions determined in step 2. to calculate the corresponding total energy of the system and construct the new electron density, $\rho(\mathbf{r})$. The initial and new electron density are combined somehow to predict a new trial density.

4. The total energy corresponding to the new electron density from step 3. is computed. If the initial and updated total energy are within a specified threshold, then the energy and, therefore, electron density achieve convergence. The new electron density is considered to accurately describe the ground-state configuration of the system, and therefore the ground-state energy is obtained.
   However, if the initial and updated total energy differ from one another, then a new trial density is estimated and a subsequent iteration step is required.

Intuitively, the lower the threshold for the calculated change in energy, the higher the accuracy of the ground-state energy calculation. Nonetheless, there is a tradeoff between accuracy and speed of the computation.

### 2.2.3 Plane-wave calculations

The application of Bloch's theorem is used to solve the Kohn-Sham equations and determine the electron density for periodic systems. Bloch's theorem defines the single-electron wavefunction in the Kohn-Sham equation in terms of plane-waves which describe the translational invariance of the lattice. The individual electron wavefunctions must satisfy Equation (2.41) and can be expressed as a sum of plane-waves of the following form[74],

$$\phi_{\mathbf{k}}(\mathbf{r}) = \exp(i\mathbf{k}\cdot\mathbf{r})u_{\mathbf{k}}(\mathbf{r}) \tag{2.42}$$

where $u_{\mathbf{k}}(\mathbf{r})$ is a function that is periodic in space and shares the same periodicity as the supercell of interest. Plane-wave functions are solved in terms of the spatial vector $\mathbf{k}$ in reciprocal space as opposed to the spatial vector $\mathbf{r}$ in real space. The Kohn-Sham equations are solved independently for each vector $\mathbf{k}$ and the electron density is obtained via summation over all $\mathbf{k}$ vectors (or "$\mathbf{k}$-space"). For a periodic unit cell, the lattice vectors can be converted from real space into reciprocal space accordingly,

$$\begin{aligned}
\mathbf{b}_1 &= 2\pi \frac{\mathbf{a}_2 \times \mathbf{a}_3}{\mathbf{a}_1 \cdot (\mathbf{a}_2 \times \mathbf{a}_3)} \\
\mathbf{b}_2 &= 2\pi \frac{\mathbf{a}_3 \times \mathbf{a}_1}{\mathbf{a}_2 \cdot (\mathbf{a}_3 \times \mathbf{a}_1)} \\
\mathbf{b}_3 &= 2\pi \frac{\mathbf{a}_1 \times \mathbf{a}_2}{\mathbf{a}_3 \cdot (\mathbf{a}_1 \times \mathbf{a}_2)}
\end{aligned} \tag{2.43}$$

It can be observed that the longer the lattice vectors in real space, the shorter the reciprocal lattice vectors. The latter define the primitive cell in reciprocal space, also known as the Brillouin zone. Both real and reciprocal primitive cells have the smallest possible volume whilst retaining the full periodicity (or symmetry) of the system. In order to facilitate plane-wave electronic structure calculations, the Brillouin zone is sampled via summation over the specified number of $\mathbf{k}$-points, the most important of which occurs at $\mathbf{k} = 0$, referred to as the $\Gamma$ point,

$$\bar{g} = \frac{V_{cell}}{(2\pi)^3} \int_{BZ} g(\mathbf{k}) d\mathbf{k} \tag{2.44}$$

where $g(\mathbf{k})$ is a periodic function that defines the periodicity of the supercell multiplied by a plane-wave, $\exp(i\mathbf{k} \cdot \mathbf{r})$. Gaussian quadrature is the most commonly employed numerical technique for integral calculation in reciprocal space. Generally, the number of k-points required for evaluation of Equation (2.44) is inversely proportional to the lattice vector in each Cartesian direction in real space. If the unit cell in real space is very large or the system lacks translation order such as liquids and amorphous materials, it becomes more efficient to evaluate the plane-wave integral in Equation (2.44) at the $\Gamma$ point only. The periodic descriptor, $u_k(\mathbf{r})$, of the wave function in Equation (2.42) can be further expanded into an infinite number of Fourier components,

$$u_{\mathbf{k}}(\mathbf{r}) = \sum_{\mathbf{G}} c_{\mathbf{G}} \exp(i\mathbf{G} \cdot \mathbf{r}) \tag{2.45}$$

The reciprocal lattice points $\mathbf{G_i}$ must satisfy $\mathbf{G} = m_1\mathbf{b}_1 + m_2\mathbf{b}_2 + m_3\mathbf{b}_3$ where $m_i$ assumes any (positive or negative) integer value and $\mathbf{b}_1$, $\mathbf{b}_2$, $\mathbf{b}_3$ span the Brillouin zone. The set of $\mathbf{G}$ vectors must satisfy the following relation - $\mathbf{G} \cdot \mathbf{a}_i = 2\pi m_i$ where $\mathbf{a}_i$ is a real space lattice vector. Since there are an infinite number of $\mathbf{G}$ values, the summation must be truncated to include only a finite number of Fourier components. Combining Equation (2.42) and Equation (2.45),

$$\phi_{\mathbf{k}}(\mathbf{r}) = \sum_{|\mathbf{G}+\mathbf{k}|<G_{cut}} c_{\mathbf{k}+\mathbf{G}} \exp\left[i(\mathbf{k}+\mathbf{G}) \cdot \mathbf{r}\right] \tag{2.46}$$

where the summation term is truncated to produce only solutions of the Schrodinger equations with kinetic energies less than a specified cutoff value of $E_{cut} = \frac{\hbar^2}{2m} G_{cut}^2$. The plane-wave cutoff energy used should be well-converged with respect to the energy difference for the system of interest. The default value for many DFT packages is the largest cutoff energy of any constituent atom.

### 2.2.4 Ab Initio Molecular Dynamics

Although the use of a prescribed potential energy function with empirically fitted parameters renders classical molecular dynamics computationally efficient, it may not reliably model chemically complex and/or ionic systems[75]. AIMD updates the atomic coordinates, accelerations and velocities through Newton's second law of motion and the Velocity Verlet algorithm, however, the interatomic forces are calculated quantum mechanically. In particular, the electrostatic interactions between electrons and nuclei are accounted for in the derivation of the potential energy, intrinsically accounting for effects such as bonding, charge transfer, polarization, and many-body effects. Therefore, AIMD provides a more rigorous and accurate description of the dynamics compared to the classical approach at the cost of increased computational resources and being restricted to small system sizes.

Additionally, AIMD is able to simulate systems for which a force field has not been parameterized yet, which is especially advantageous given the effort and complexity involved in force field parameterization.

The main difference between classical MD and AIMD is the potential energy used to derive the interatomic forces in Equation (2.3). In AIMD, the potential energy of the system is calculated via DFT using the full set of Kohn-Sham single-electron wavefunctions from Equation (2.41).

### 2.2.5 Density of States

The density of states (DOS) of a material describes the number of energy states available for occupation in the energy interval $(E \rightarrow E + \Delta E)$[74]. The distribution of energy states in a material provides insight into its electronic behavior and bonding. As the system size increases, the spacing between allowed energy levels decreases, resulting in a continuum of quantum states. Atoms and molecules are characterized by a spectral DOS owing to their discrete energy levels, while periodic crystal structures have a continuous DOS. Of critical importance is the DOS at the band edge between the valence and conduction bands. For example, an insulating material is characterized by a "forbidden zone" between the valence band and conduction band which no electrons can occupy. In contrast, the valence band and conduction band overlap in a conducting material, indicating free electron behaviour. The projected DOS (pDOS) provides a space-resolved DOS by decomposing the total DOS into angular momentum components of the constituent atoms in the system.

In periodic crystal structures, electrons are considered as free meaning their behaviour can be approximated by the free electron particle in a box model in which one electron is constrained within a potential well. The dimensions of this well, $a$, are considered to be identical to the lattice constant of the crystal. Using boundary conditions, the solution to the Schrodinger equation for one electron becomes the following[77]:

$$E_n = \frac{\pi^2 \hbar^2}{2ma^2} \left( n_x^2 + n_y^2 + n_z^2 \right) \tag{2.47}$$

where $n_x$, $n_y$ and $n_z$ are principal quantum numbers that can assume integer values from $1...n$. Each set of principal quantum numbers in associated with a point $E_n$ in $n$-space. This can be represented geometrically, where equal energy values lie on the surface of a sphere with radius $n = \sqrt{n_x^2 + n_y^2 + n_z^2}$. Since $n$ can only assume positive integer values, only the positive octant of the $n$-space is considered. The number of quantum states with energy values less than $E_n$ becomes proportional to one eighth of the spherical volume.

$$\eta = \frac{1}{8}\frac{4}{3}\pi n^3 = \frac{1}{6}\pi\left(\frac{\sqrt{2ma^2E}}{\pi\hbar}\right)^3 \tag{2.48}$$

Differentiation of $\eta$ with respect to the energy $E$ provides the number of energy states per unit energy, also referred to as the density of states. For a free electron model, the density of states is proportional to $\sqrt{E}$.

$$\frac{d\eta}{dE} = Z(E) = \frac{\pi}{4}\left(\frac{2ma^2}{\pi^2\hbar^2}\right)^{\frac{3}{2}} E^{\frac{1}{2}} = \frac{V}{4\pi^2}\left(\frac{2m}{\hbar}\right)^{\frac{3}{2}} E^{\frac{1}{2}} \tag{2.49}$$

Intuitively, as the energy increases, the combinations of possible quantum numbers resulting in the energy increases. However, for actual crystals, the DOS will sometimes deviate from the theoretical $\sqrt{E}$ dependence due to the $E$ vs $k$ energy dispersion relation.

$$E = \frac{\hbar}{2m}\left(k_x + \frac{2\pi n}{a}\right)^2 \tag{2.50}$$

Discontinuities are observed at $k_x$ values of $\frac{n\pi}{a}$ at which the branches of individual parabolas intersect with adjacent ones, which cause a deviation from the free electron parabolic function defined by $E = k_x^2$. These critical points are referred to as van Hove singularities, where the slope of the dispersion curve approaches zero. This causes a spike in the DOS at that particular energy. The more the electronic structure deviates from the free electron model, the larger the width of the disallowed energy gaps known as "band gaps" in these regions. Therefore, the energy conditions in the reduced zone scheme, or alternatively, first Brillouin zone, cause deviations from the theoretical DOS model in Equation (2.49).

The Fermi level is formally defined as the energy at which the Fermi function equals $\frac{1}{2}$. Given that the Fermi function is the probability of an electron occupying a given energy state, the Fermi level can be thought of as the energy at which the probability of electron occupation is $\frac{1}{2}$. The higher the Fermi level of the system, the higher the electronic levels of a system occupied by electrons.

### 2.2.6 Projected Crystal Orbital Hamilton Populations

Electronic structure calculations based on plane-wave density functional theory provide a self-consistent description of the electron density in a periodic system. When these calculations are performed with a sufficiently dense $k$-point mesh, as required by Bloch's theorem, the outcome is a set of band functions $\phi_j(\mathbf{k}, \mathbf{r})$, where $j$ denotes the band index. Each band function can be represented as a linear combination of plane waves:

$$\phi_j(\mathbf{k}, \mathbf{r}) = \sum_{\mathbf{G}} c_{j\mathbf{G}}(\mathbf{k})\, e^{i(\mathbf{k}+\mathbf{G})\cdot\mathbf{r}} \tag{2.51}$$

Although these band functions may appear purely mathematical being expressed as linear combinations of plane waves with coefficients $C_{j\mathbf{G}}(\mathbf{k})$ and reciprocal lattice vectors $\mathbf{G}$ they encode the same physical information as a linear combination of atomic orbitals (LCAO). Thus, we can define an LCAO-type representation $\Phi_j(\mathbf{k}, \mathbf{r})$ that approximates the same electronic state as $\phi_j(\mathbf{k}, \mathbf{r})$:

$$\Phi_j(\mathbf{k}, \mathbf{r}) = \sum_{\mu} c_{j\mu}(\mathbf{k})\, \psi_\mu(\mathbf{r}) \approx \phi_j(\mathbf{k}, \mathbf{r}) \tag{2.52}$$

Here, $\phi_\mu(\mathbf{r})$ are localized, orthonormal atomic orbitals centered on the atoms of the unit cell, and $c_{j\mu}(\mathbf{k})$ are the corresponding expansion coefficients.

The choice of localized orbitals $\{\phi_\mu\}$ is flexible and guided by chemical intuition. One may employ Slater-type orbitals or other basis sets suited to the bonding characteristics

of interest. To quantify how well the chosen local basis can reproduce the plane-wave-derived band functions, we define the *transfer matrix* $T(\mathbf{k})$ as the overlap between the band functions and the local orbitals:

$$T_{j\mu}(\mathbf{k}) = \langle \psi_j(\mathbf{k}) | \phi_\mu \rangle \tag{2.53}$$

Within the LCAO formalism, the coefficients $c_{j\mu}$ convey chemical information, as products such as $c_\mu c_\nu$ form elements of the density matrix $P_{\mu\nu}$. In the plane-wave framework, equivalent information resides in the transfer matrix. Thus, a projected density matrix for each band $j$ and each $k$-point is defined as:

$$P^{(\mathrm{proj})}_{\mu\nu,j}(\mathbf{k}) = T^*_{j\mu}(\mathbf{k})\, T_{j\nu}(\mathbf{k}) \tag{2.54}$$

To perform a COHP-like analysis, we must also express the Hamiltonian operator in the local orbital basis. This is achieved by projecting the plane-wave Hamiltonian $\hat{H}^{(\mathrm{PW})}$ onto the same localized functions:

$$\begin{aligned} H^{(\mathrm{proj})}_{\mu\nu}(\mathbf{k}) &= \langle \phi_\mu | \hat{H}^{(\mathrm{PW})} | \phi_\nu \rangle \\ &= \sum_j \langle \phi_\mu | \psi_j(\mathbf{k}) \rangle\, \varepsilon_j(\mathbf{k})\, \langle \psi_j(\mathbf{k}) | \phi_\nu \rangle \end{aligned} \tag{2.55}$$

By substituting eq. (2.53), we can rewrite the above as:

$$H^{(\mathrm{proj})}_{\mu\nu}(\mathbf{k}) = \sum_j \varepsilon_j(\mathbf{k})\, T^*_{j\mu}(\mathbf{k})\, T_{j\nu}(\mathbf{k}) \tag{2.56}$$

With both projected density and Hamiltonian matrices available, the projected Crystal

Orbital Hamilton Population (pCOHP) can be defined as[78]:

$$\mathrm{pCOHP}_{\mu\nu}(E,\mathbf{k}) = \sum_j \Re\left[P^{(\mathrm{proj})}_{\mu\nu,j}(\mathbf{k})\, H^{(\mathrm{proj})}_{\nu\mu}(\mathbf{k})\right] \delta(\varepsilon_j(\mathbf{k}) - E) \tag{2.57}$$

This expression is energy-dependent since the Dirac delta ensures that contributions arise only from band energies equal to $E$. The real-space pCOHP($E$) is obtained by summing over orbital pairs $(\mu, \nu)$ corresponding to the atoms forming the bond of interest and integrating across the Brillouin zone.

Finally, the integrated projected COHP (IpCOHP), analogous to the integrated COHP (ICOHP), is obtained by integrating the pCOHP up to the Fermi level $\varepsilon_F$:

$$I_{\mathrm{pCOHP}}(\varepsilon_F) = \int_{-\infty}^{\varepsilon_F} \mathrm{pCOHP}(E)\, dE \tag{2.58}$$

This integrated measure provides a chemically intuitive description of bonding contributions up to the Fermi energy, offering a bridge between plane-wave calculations and orbital-based bonding analysis.

### 2.2.7 Electron Localization Function

Defined in 1990 by Becke and Edgecombe,[79] the electron localization functions (ELFs), denoted as $\eta(\mathbf{r})$, quantifies the maximal probability for finding an electron pair in a molecule or a crystal. This work laid the foundation for ELF's wide adoption and further generalizations in density functional theory by Savin et al. and others[80]. Its mathematical expression is given by:

$$\eta(\mathbf{r}) = \frac{1}{1 + \left(\frac{D_s(\mathbf{r})}{D_s^0(\mathbf{r})}\right)^2} \tag{2.59}$$

where $D_s(\mathbf{r})$ represents the electron localization measure of the system, and $D_s^0(\mathbf{r})$ corresponds to the reference value from a homogeneous electron gas. These quantities are defined as:

$$D_s(\mathbf{r}) = \tau_s(\mathbf{r}) - \frac{1}{4}\frac{|\nabla\rho_s(\mathbf{r})|^2}{\rho_s(\mathbf{r})} \tag{2.60}$$

$$D_s^0(\mathbf{r}) = \frac{3}{5}(6\pi^2)^{2/3}\rho_s^{5/3}(\mathbf{r}) \tag{2.61}$$

Here, $\tau_s(\mathbf{r})$ is the kinetic energy density and $\rho_s(\mathbf{r})$ is the electron spin density for spin $s$.

The ELF ranges from 0 to 1, where a value of 1 indicates perfect electron localization, such as in electron pairs or lone pairs, and a value of 0.5 reflects electron-gas-like delocalization. The maxima of the ELF function are called attractors, with each attractor defining a separate domain (or pair region) in space. All points that, when followed along the path of steepest ascent of the ELF function, reach the same attractor are assigned to its domain. The total number of valence electrons in a domain is computed by integrating the electron density over that domain.

## 2.3 Computational Framework

This section has been reproduced from Agnes Britte Katai, Arjun Varma Ramasimha Varma, and Conrard Giresse Tetsassi Feugmo; "Computational Insights into the corrosion behavior of NbTaMoW and NbTaMoWV high-entropy alloys in molten fluoride salts", Faraday Discuss, (2025). https://doi.org/10.1039/D5FD00102A [67].

The general workflow for constructing the interface between the body-centered cubic (BCC) (100)-NbTaMoW and -NbTaMoWV surfaces, and the FLiBe salt overlay, is depicted in Fig. 2.1. The refractory high entropy alloys (RHEAs) and salt subsystems were independently equilibrated at 800 K using classical molecular dynamics (see Section 2.1) implemented within the Large-scale Atomic/Molecular Massively Parallel Simulator (LAMMPs) [81], with their respective external machine-learned potentials, 2b+3b tabGAP [82,83] and moment tensor potentials [19,84]. Thermal equilibration was conducted in the isothermal–isobaric ($NPT$) ensemble at 800 K for both subsystems, employing a Nosé–Hoover thermostat (see Section 2.1.3) and barostat to maintain the desired temperature of the particles and facilitate volume relaxation under ambient pressure, respectively.

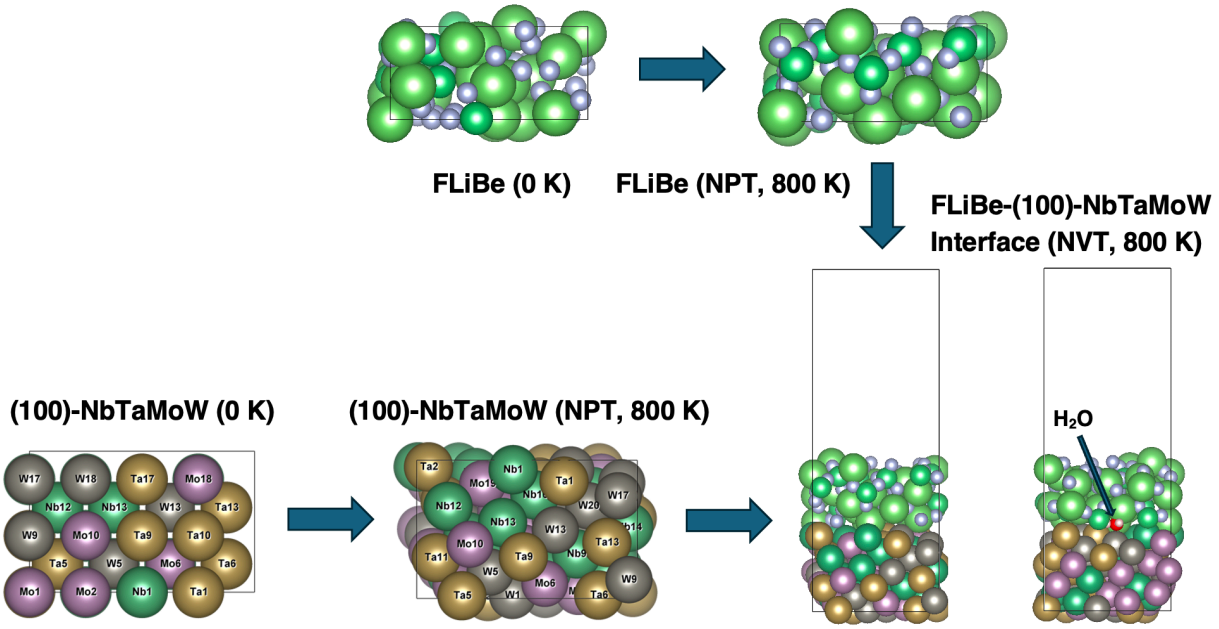



Figure 2.1: Workflow for constructing the refractory high entropy alloy (RHEA)–salt interface. Top left: Initial configuration of FLiBe at 0 K. Top right: Thermally equilibrated FLiBe at 800 K under *NPT* conditions. Bottom left: Initial BCC (100) NbTaMoW slab at 0 K. Bottom middle: Thermally relaxed BCC (100) NbTaMoW at 800 K under *NPT* ensemble. Bottom right: Construction of the interface between the equilibrated BCC slab and molten salt, under *NVT* conditions at 800 K. In parallel, 1 $H_2O$ molecule was added at the RHEA-FLiBe interface and the system was simulated in the *NVT* ensemble.

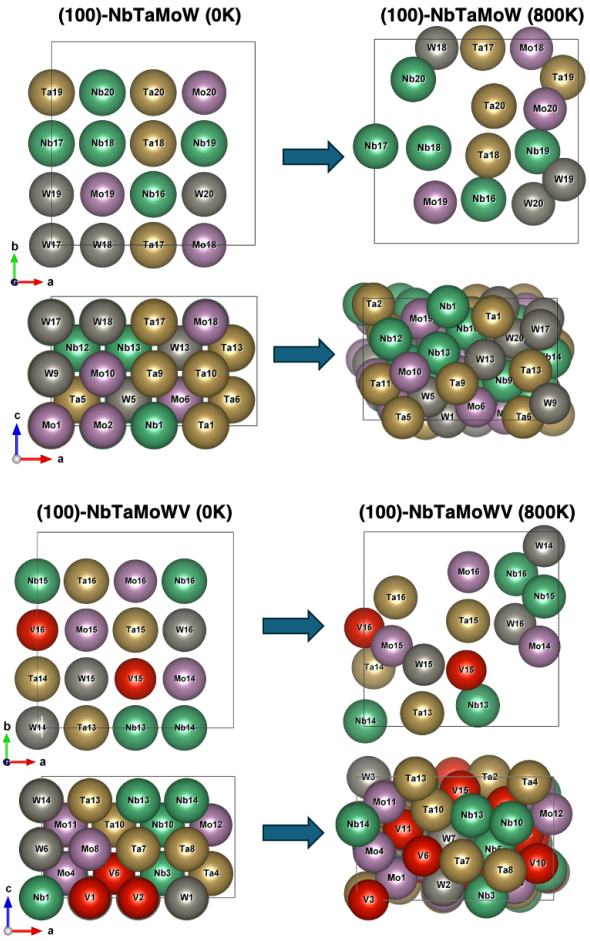



Figure 2.2: Bird's eye view of surface atoms (top) and side view (bottom) of (100)-NbTaMoW and (100)-NbTaMoWV slabs. An *NPT* simulation was conducted on both (100)-RHEA slabs for 100 ps at 800 K to equilibrate the slab volume and atomic configuration at the given temperature. Only the surface atoms are depicted in the bird's eye view (top) with the atoms in the bottom layers filtered out from the image.

This equilibration step is imperative for achieving a stable atomic configuration and density prior to modeling the RHEA-FLiBe interface at the desired temperature, especially for the molten salt environment.

Two BCC (4 x 4 x 5) (100)-NbTaMoW and -NbTaMoWV surfaces containing a total of 80 atoms were constructed using ASE, a Python package for setting up atomic simulations. The constituent elements were randomly distributed throughout the RHEA slab in equiatomic concentrations using the ICET Python package[85]. The lattice constants utilized were 3.220 Å and 3.185 Å for NbTaMoW and NbTaMoWV, respectively, as determined experimentally by Senkov et al.[54]. Fig. 2.2 depicts the initial configuration of the (100)-NbTaMoW slab (top left) and (100)-NbTaMoWV slab (bottom left) prior to the equilibration step at high temperature.

As shown in Fig. 2.2, separate *NPT* simulations were carried out on (100)-NbTaMoW and -NbTaMoWV slabs for a duration of 100 picoseconds (ps) at 800 K and ambient pressure with a timestep of 0.001 ps using 2b+3b tabGAP machine-learned interatomic potentials[82,83] to obtain thermally equilibrated surfaces. The initial particle velocities were sampled from a Gaussian distribution and scaled to 800 K using Equation (2.16). Nosé–Hoover style thermostating and barostating were achieved with damping coefficients of 0.0001 and 0.001 ps, respectively. The Nosé–Hoover style equations of motion used to compute particle dynamics are presented in Equations (2.18)–(2.23). During barostatting, all 3 diagonal components were relaxed simultaneously in order to compute the hydrostatic pressure.

In parallel, an initial randomized configuration of 2LiF–$BeF_2$ (FLiBe) was generated using the Packmol[86] package with 56 F, 28 Li and 14 Be atoms based on an experimental density of 2.156 g/cm$^3$ at 800 K[87]. The FLiBe overlay was constructed such that the xy-plane matches the area of its corresponding RHEA slab to ensure interfacial commensurability for subsequent simulations. Using the same simulation parameters as for the RHEAs, the salt system was independently equilibrated for 100 ps using moment tensor potentials[19,84]. Sample *NPT* simulation data for the (100)–NbTaMoW slab and its corresponding FLiBe overlay can be accessed at https://doi.org/10.5281/zenodo.15699534.

Following thermal equilibration of each subsystem, a clean metal surface was set up alongside the RHEA-salt interfaces for subsequent reference. To investigate the effect of moisture on the corrosion process, 1 $H_2O$ molecule was randomly added at the RHEA-salt interface to be conducted in parallel with the clean metal surface and the interface between the metal and the pure salt (Fig. 2.1). A vacuum spacing of 20 Å was added in the z-direction perpendicular to the isolated slab and both RHEA–salt interface configurations. The two bottom layers of each RHEA slab were immobilized where as the topmost three layers were allowed to move freely. The simulation cells were as follows: 1) isolated (100)-NbMoTaW and (100)-NbMoTaWV slabs, 2) (100)-NbMoTaW and (100)-NbMoTaWV slabs interfaced with pure FLiBe and 3) (100)-NbMoTaW and (100)-NbMoTaWV slabs interfaced with a FLiBe layer containing 1 $H_2O$ molecule. The Python script used to prepare the initial configuration of the salt-alloy interface can be obtained from https://doi.org/10.5281/zenodo.15699534.

The equilibrated structures, including the isolated slab and salt-slab interfaces, were simulated in the canonical ($NVT$) ensemble for 40 ps using the Vienna Ab initio Simulation Package (VASP)[88] through Born–Oppenheimer ab initio molecular dynamics (AIMD) (see Section 2.2.4). Dynamics were modified according to a Nosé–Hoover thermostat at a temperature of 800 K with a timestep of 1 femtosecond (fs). Electronic calculations utilized spin-polarized density functional theory (DFT) detailed in Section 2.2, in conjunction with the projector augmented wave (PAW) method. The generalized gradient approximation (GGA) with the Perdew-Burke-Ernzerhof (PBE) formulation was implemented to account for the exchange and correlation effects[76]. A plane-wave energy cutoff of 400 eV, an electronic energy convergence threshold of $10^{-4}$ eV and Gaussian smearing with a smearing width of 0.2 eV was used, along with a Γ-centered $1 \times 1 \times 1$ $k$-point mesh. Grimme's D3 dispersion correction[89] was implemented to account for the Van der Waals interactions within the salt and at interface regions. Each system underwent equilibration at 800 K for no less than 10 ps, followed by production runs of up to 30 ps. Sample $NVT$ simulation data for the interface between (100)-NbTaMoW and pure FLiBe can be accessed at https://doi.org/10.5281/zenodo.15699534.

The electronic structure, interfacial bonding and redox reactions were examined utilizing density of states (DOS), crystal orbital Hamilton population (COHP) analyses and the partitioning of the electron localization function (ELF) with subsequent integration of electron density, respectively, at every 10 ps for a total of 40 ps of simulation time. The theoretical principles of the DOS, COHP and ELF calculations are detailed in Sections 2.2.5, 2.2.6 and 2.2.7, respectively.

DOS analyses were conducted using the py4vasp software, a tool for extracting data from VASP output files. COHP analysis was employed using the LOBSTER code[90], which reconstructs localized orbital information from plane-wave DFT outputs. The projected COHP and bond strength corresponding to an atomic pair are computed via Equation (2.57) and (2.58), respectively. The ELF is computed via Equation (2.59) and analyzed using Critic2[91]. All customized Python scripts involved in data postprocessing and generating plots can be found at https://github.com/aka607/PyVaspTools.git.. All atomic configurations were visualized with VESTA[92] and OVITO[93].

To assess the accuracy of the 2b+3b tabGAP machine-learned force field and the simulation parameters in DFT and implemented in the equilibration step, a set of equation of state (EOS) calculations were conducted for each pure BCC refractory metal in the RHEA composition (Nb, Ta, Mo, W, V) using both methods[82]. These calculations employed the VASP and LAMMPS calculators integrated into ASE. Murnaghan's EOS models[94] were fitted to static energy calculations performed at fixed volumes in the range of $0.8V_0$ to $1.2V_0$ where $V_0$ is the estimated equilibrium volume. Structural properties were derived from the EOS, including the lattice parameter and bulk modulus, and compared against experimental values[95]. The DFT predictions were in strong agreement with experimental lattice constants (within 0.3% error, except for V), and within reasonable accuracy for bulk moduli, aligning with the observations of Fernández-Pello et al.[96]. The tabGAP potential also performed reasonably well, manifesting its transferability to pure-element systems. Full details and comparative results, including EOS fits and property discrepancies, are provided in the Appendix (Figures 19-20, Table 5). All Python scripts and electronic structure calculations pertaining to the EOS can be retrieved from https://doi.org/10.5281/zenodo.15699534.

# Chapter 3

# Observations

This chapter has been reproduced from Agnes Britte Katai, Arjun Varma Ramasimha Varma, and Conrard Giresse Tetsassi Feugmo; "Computational Insights into the corrosion behavior of NbTaMoW and NbTaMoWV high-entropy alloys in molten fluoride salts", Faraday Discuss. (2025).
https://doi.org/10.1039/D5FD00102A[67].

## 3.1 HEA Subsystem Equilibration

As depicted in Fig. 2.2, both (100)-NbTaMoW and -NbTaMoWV slabs no longer exhibit a single-phase BCC crystal structure after equilibration at 800 K[67]. Many atoms have been displaced away from their BCC lattice positions to minimize the energy at 800 K, thereby removing the symmetry from the system. A common neighbor analysis (Fig. 3.1) was performed to characterize the local atomic arrangement of the alloys. This algorithm classifies atoms based on the cutoff distance between atoms in the crystal structure. Fig. 3.1 illustrates a ≈50% loss of the BCC crystal structure for thermally equilibrated (100)-NbTaMoW and -NbTaMoWV slabs. This behavior is attributed to the formation of point defects, such as vacancies and self-interstitials, and the enhanced motion of dislocations at elevated temperatures, an effect that is amplified in smaller atomic systems. Compositionally complex solid solutions are known to exhibit a greater variation in the en-

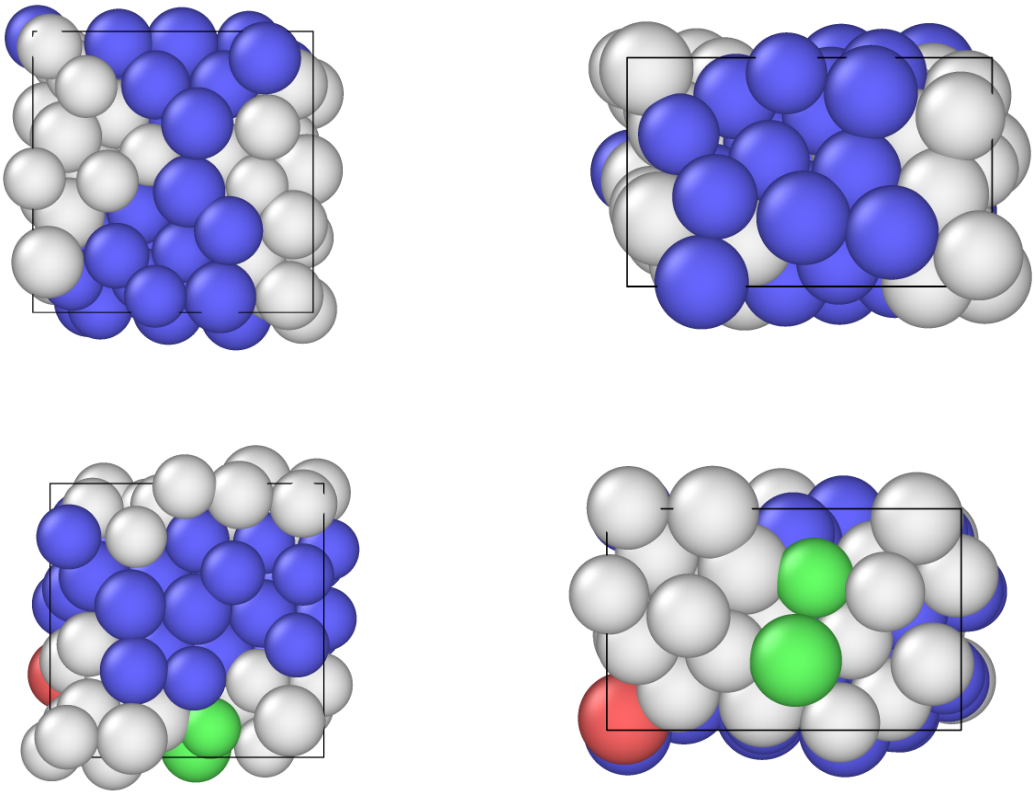


Figure 3.1: Common neighbor analysis of (100)-NbTaMoW (top) and (100)-NbTaMoWV (bottom) slabs after 100 ps of NPT using classical molecular dynamics with tabGAP potentials[82]. Bird's eye and side view of the lattice are shown on the left- and right-hand side, respectively. Atoms classified as BCC phase are depicted in blue, FCC in green, and HCP in red. White atoms correspond to an unknown crystal structure.

ergy landscape due to the vastly differing Peierls barriers amongst constituent elements[97]. This results in unpredictable dislocation movement, causing the RHEA slabs to adopt an asymmetric (or lopsided) configuration as shown in Fig. 2.2.

The loss of the BCC crystalline after equilibration at 800 K is further evidenced by the loss of long-range ordering in the total radial distribution function between 0 ps (blue) and 100 ps (red) illustrated in Fig. 3.2. In both Fig. 3.2-a. and 3.2-b., the disappearance of peaks after 100 ps is observed at 1.4-1.9 Å, 3.5-4.3Å and $>$ 6Å. Moreover, the two sharp, well-defined peaks observed at 0 ps in the ranges 2.5-3.5 Å and 4.2-5.8 Å undergo notable changes by 100 ps - the former peaks merge into a single broader peak at 2.5-3.5 Å, while the latter join to form a bimodal distribution at 4.2-5.8 Å. However, the peak in

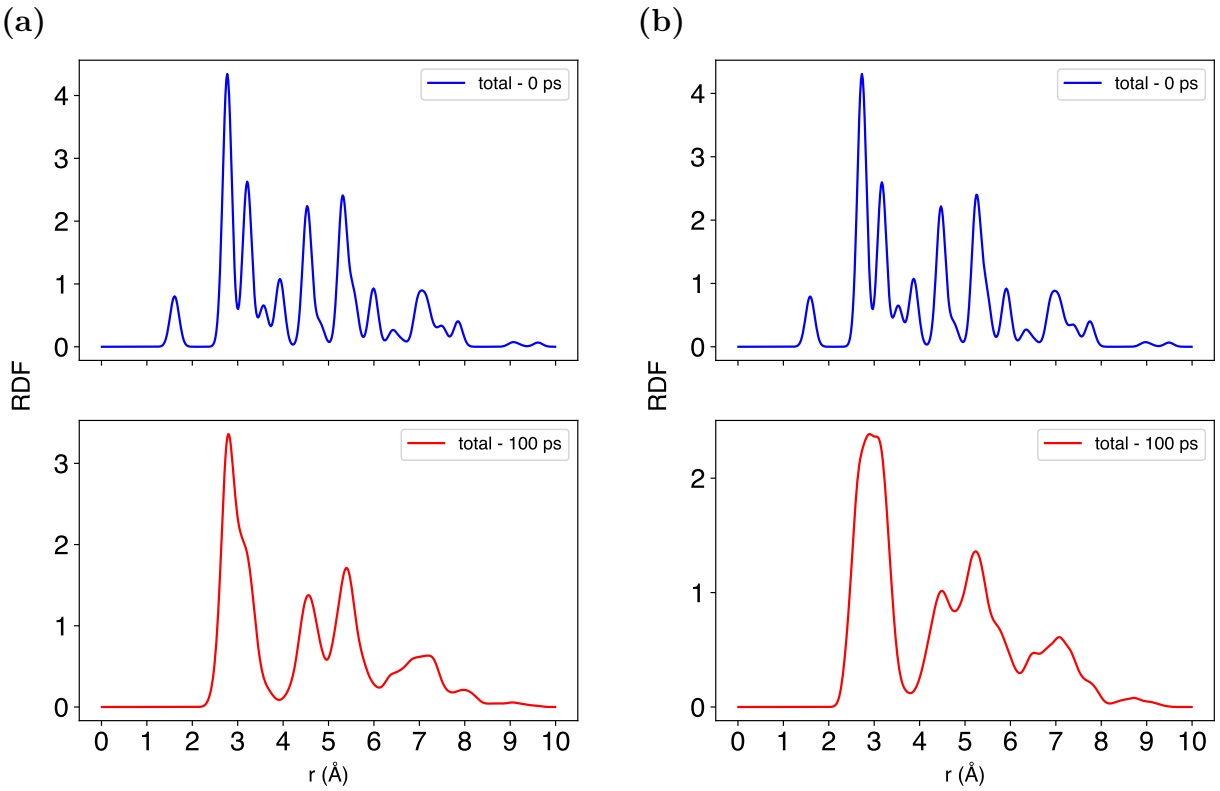



Figure 3.2: Total radial distribution function of a) (100)-NbTaMoW and b) (100)-NbTaMoWV slabs at 0 ps (blue) and 100 ps (red) of *NPT* at 800 K using classical molecular dynamics with tabGAP potentials[82].

the 4.2-5.8 Å range exhibits a more unimodal character for NbTaMoWV (Fig. 3.2-b., 100 ps) compared to that in NbTaMoW (Fig. 3.2-a., 100 ps). These observations are indicative of increased structural disorder introduced by point defects and dislocations in the lattice, particularly for NbTaMoWV.

## 3.2 Density of States

Fig. 3.3 illustrates the total and partial DOS for BCC (100)-NbTaMoW and -NbTaMoWV surfaces both in vacuum and in contact with pure molten FLiBe[67]. Fig. 3.4 compares the total and partial DOS of the two RHEA compositions in vacuum and in contact with $H_2O$-contaminated molten FLiBe. All configurations in Fig. 3.3-3.4 were examined after 40 ps of *NVT* simulation at 800 K. Three simulations were conducted in parallel; one for the RHEA

without salt represented by the blue line, another for the RHEA including the salt overlay represented by the red line (Fig. 3.3), and another for the RHEA combined with $H_2O$-contaminated salt represented by the black line (Fig. 3.4). To facilitate a direct comparison between the alloy surfaces devoid of salt and those covered with salt, the energies along the x-axis are displayed without adjustment to the Fermi level ($E_F$). Additionally, Fig. 3.5 depicts the overlaid DOS profiles of NbTaMoW and NbTaMoWV in pure salt and in $H_2O$-contaminated salt, highlighting the similarities and differences in the electronic stability of the two RHEA compositions. The salt-alloy interfaces without and with vanadium (V) are represented by the green and purple line, respectively. The DOS near the Fermi level is of highest significance due to its correlation with bonding and material properties.

In both Fig. 3.3 and Fig. 3.4, there is substantial overlap between the valence and conduction bands in both the total and partial DOS of NbTaMoW and NbTaMoWV, thereby corroborating the metallic nature of these RHEAs. Furthermore, the total DOS manifests a bimodal distribution with the Fermi level located within the "pseudo-band gap", attesting to the electronic stability of the BCC crystal structure as previously documented[98,99]. The pseudo-band gap defines the incomplete energy gap at the minimum of the bimodal distribution in the DOS. Despite the defect formation observed in the RHEA slab at 800 K in Fig. 2.2, the bimodal shape of the total DOS indicates that some BCC crystalline character remains. Nonetheless, Fig. 3.5 shows that the incorporation of the FLiBe salt layer markedly broadens this pseudo-band gap in the NbTaMoW system (green line) compared to NbTaMoWV (purple line), suggesting enhanced covalency in the NbTaMoW system[100]. Conversely, the metallic character increases upon introduction of vanadium (V) within the alloy, thereby narrowing the pseudo-band gap and elucidating its role in modulating the electronic structure.

For both RHEA-salt interfaces in Fig. 3.3, the primary contributors to the lower valence band are the 2p-orbitals of F, whereas the upper valence band and lower conduction band are dominated by refractory metal d-orbitals. Upon contact with $H_2O$ (Fig. 3.4), the 2p-orbitals of O contribute to the lower valence band which displays an upward shift toward higher energies. The compact shape of the 2p-orbitals of F and O (see Fig. 3.3, 3.4-F

and Fig. 3.4-O) and the metal d-electron delocalization (see Fig. 3.3, 3.4-Nb,Ta,Mo,W,V) highlight the covalent and metallic bonding in the salt and RHEA subsystems, respectively. Furthermore, the overlap between metal s and d orbital contributions within the valence band is indicative of s–d hybridization, a characteristic of metallic cohesion in transition metals. Weak orbital hybridization between the constituent metals and the electronegative F/O species is evident from the minimal overlap between the 2p-orbitals of F/O and metal d-orbitals (see Fig. 3.3 and Fig. 3.4). These electronic descriptors manifest the modest reactivity of the RHEA sub-lattice.

Significantly, the partial d-orbital DOS for Nb and Ta (see Fig. 3.3,3.4-Nb,Ta) depict a left-skewed distribution and a less pronounced bimodal shape compared to Mo and W. Consequently, the higher local DOS in the conduction band relative to the valence band suggests higher reactivity for Nb and Ta. In contrast, Mo and W (see Fig. 3.3,3.4-Mo,W) exhibit a nearly symmetric bimodal d-band structure, typically corresponding to higher electronic stability and a reduced susceptibility to oxidation by the salt melt. This enhanced stability found in Mo and W arises from the progressive filling of the d-band across the transition metal series, which causes the $n$d-level to approach or fall below the $(n+1)$s level. The reduction in d-band energy elevates the ionization energies of Mo and W, thereby diminishing their oxidative potential compared to earlier transition metals.

As seen in Fig. 3.3-3.4, upon exposure to FLiBe, the occupied electronic states in both RHEAs exhibit a shift toward higher energy levels as indicated by the progressive increase in the Fermi level. This evolution is captured in the DOS at 20 ps and 30 ps, as shown in Figures 15-18 in the Appendix. At 40 ps, the separation between the 2p orbitals of F and the metal d orbitals of the metal has intensified due to the upward shift of the metal d-band states and the simultaneous downward shift of the F 2p-states, demonstrating progressive destabilization of the metal in the salt. Amongst the constituent refractory metals, Mo d-electrons experience the smallest energy shift while Ta d-electrons exhibit the largest shift, indicative of lower and higher reactivity, respectively. Notably, in Fig. 3.5, the NbTaMoW system in pure FLiBe exhibits a greater increase in high-energy electron occupation relative to the NbTaMoWV system, suggesting that incorporating V heightens corrosion resistance.

This is consistent with the enhancement of metallic bonding introduced by vanadium in the NbTaMoWV HEAs. Interestingly, following contact with water, the differences between the DOS profiles of NbTaMoW-salt and NbTaMoWV-salt interfaces diminishes.

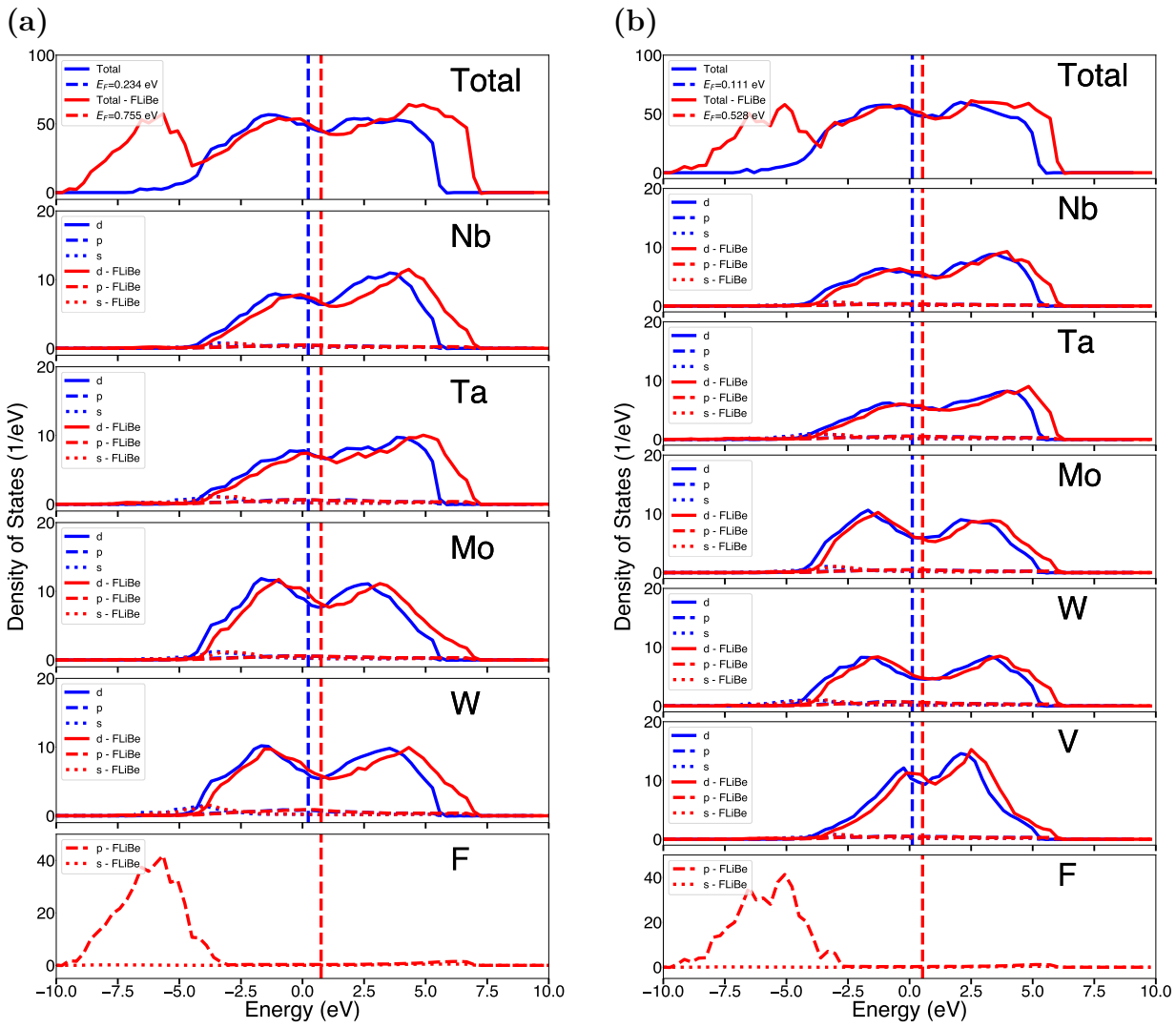



Figure 3.3: Total and partial density of states of the BCC (100)- a) NbTaMoW and b) NbTaMoWV surfaces, in contact with a molten FLiBe salt after 40 ps at 800 K. The blue curves represent the DOS of the clean refractory high-entropy alloy without the FLiBe layer, while the red curves depict the DOS with the FLiBe layer present. The dotted blue and red vertical lines represent the Fermi level of the clean RHEA surface and the RHEA with the added salt, respectively.

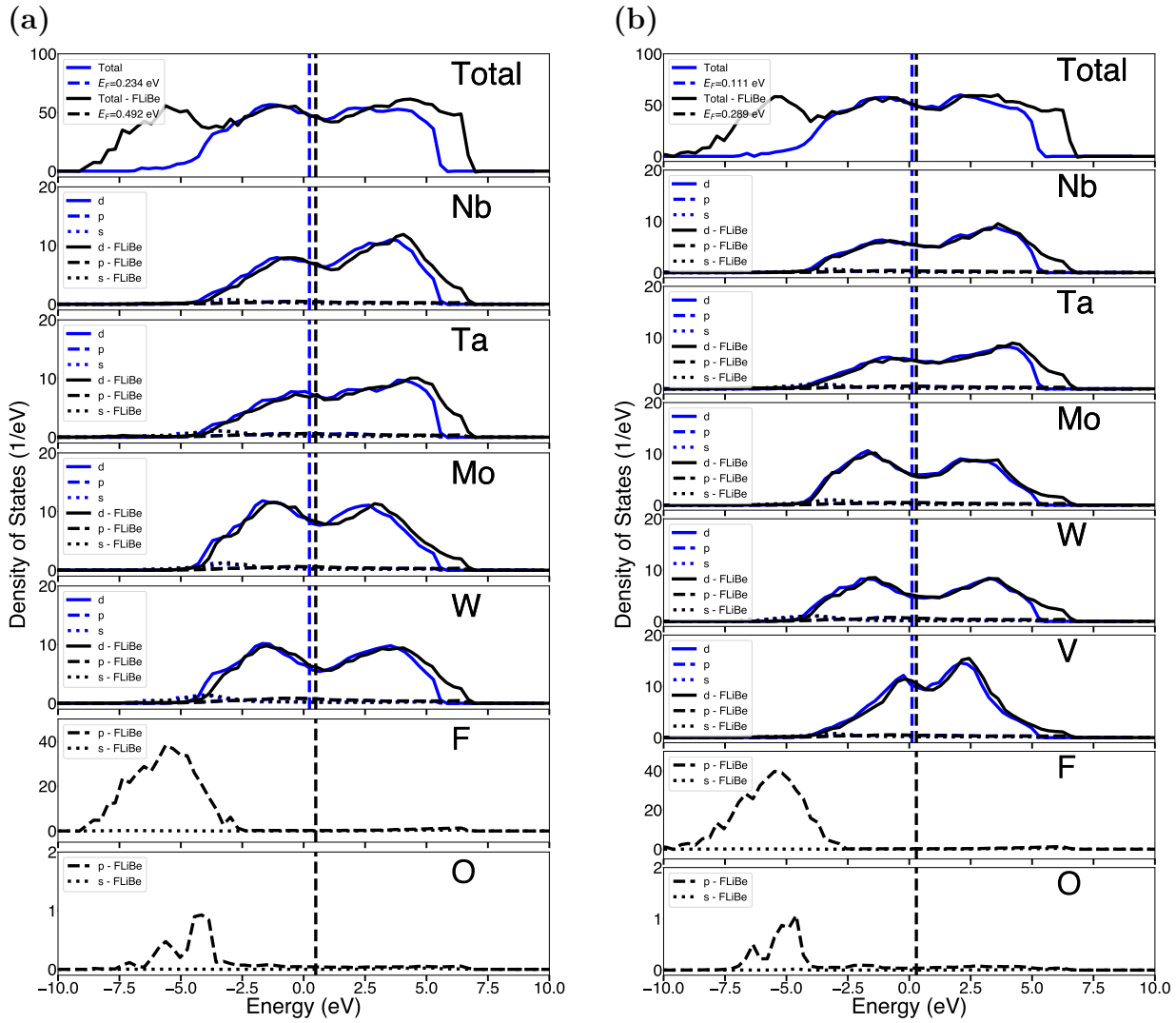



Figure 3.4: Total and partial density of states of the BCC (100) a) NbTaMoW and b) NbTaMoWV surfaces, in contact with a molten FLiBe salt contaminated with a $H_2O$ molecule after 40 ps at 800 K. The blue curves represent the DOS of the clean refractory high-entropy alloy without the FLiBe layer, while the black curves depict the DOS with the $H_2O$-contaminated FLiBe layer present. The dotted blue and black vertical lines represent the Fermi level of the clean RHEA surface and the RHEA with the $H_2O$-contaminated salt, respectively.

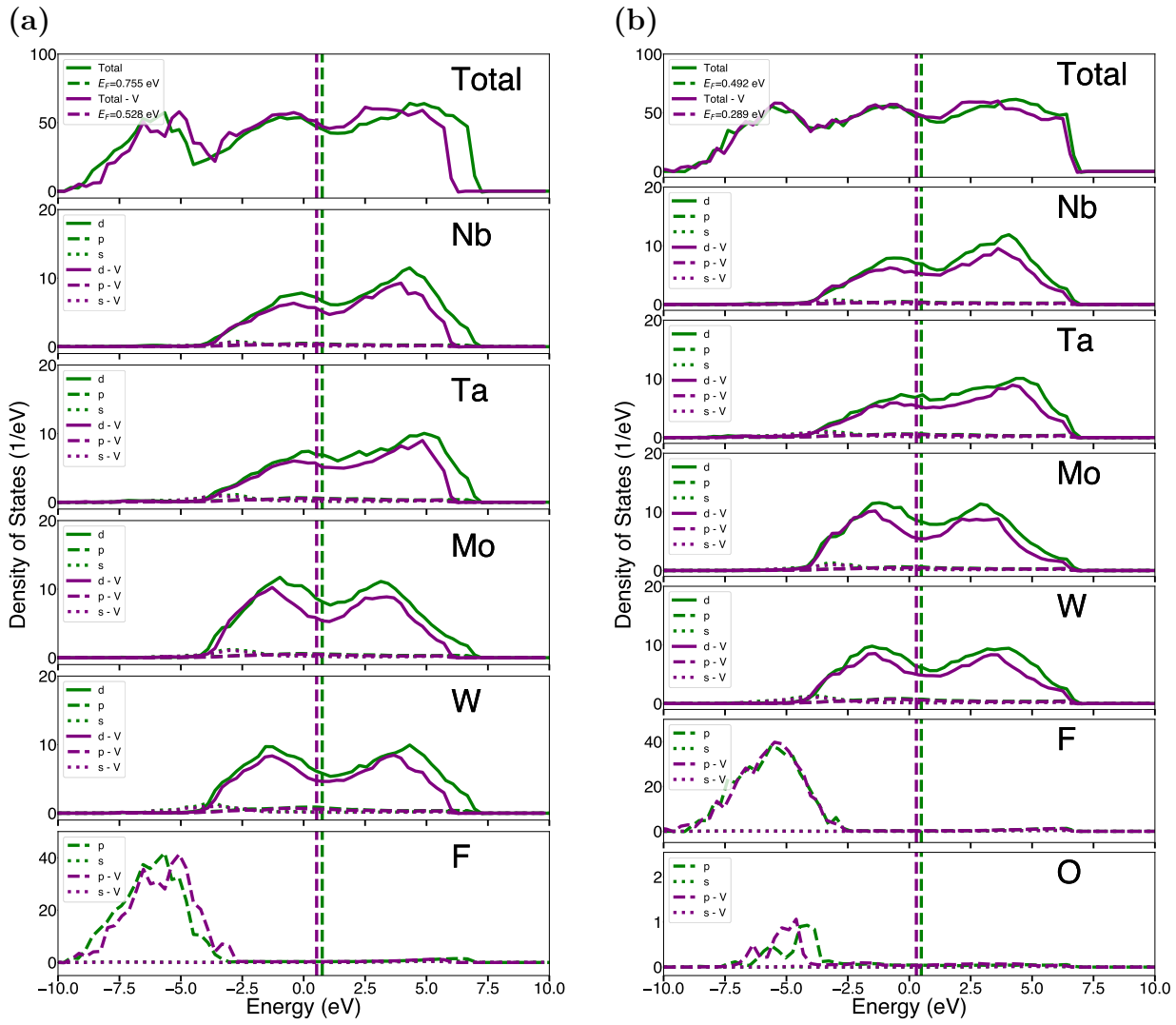



Figure 3.5: Total and partial density of states of BCC (100) NbTaMoW and NbTaMoWV surfaces, in contact with a) pure molten FLiBe salt and b) FLiBe salt contaminated with a $H_2O$ molecule after 40 ps at 800 K. The green curves represent the DOS of the NbTaMoW-salt interface, while the purple curves represent the DOS of the NbTaMoWV-salt interface. The dotted green and purple vertical lines represent the Fermi level of the NbTaMoW and NbTaMoWV alloy with the added salt, respectively.

## 3.3 Crystal Orbital Hamilton Population Analysis

To gain quantitative insight into the interfacial bonding between the refractory metal atoms and the electronegative fluorine/oxygen species, crystal orbital Hamilton populations (COHPs) analysis was conducted on both NbTaMoW and NbTaMoWV slabs in contact with a pure and hydrated FLiBe salt layer. Each configuration was examined after 10, 20, 30 and 40 ps of simulation time at 800 K. The evolution of bond lengths and integrated crystal orbital Hamilton populations (ICOHPs) values corresponding to representative metal–fluorine (M–F) pairs at the interface between the RHEA slabs and the pure FLiBe overlay are presented in Fig. 3.6. The evolution of representative M-F and metal–oxygen (M–O) pairs at the interface between the RHEA slabs and the $H_2O$-contaminated FLiBe overlay are presented in Fig. 3.7. The electronic profiles of both RHEA compositions in contact with pure and hydrated salt are displayed by the -COHP curves in Fig. 3.8 and Fig. 3.9, respectively, and examined in further detail in Tables 1-4, as well as Figures 21-24 in the Appendix.

No evidence of stable covalent M–F bonding was observed across both RHEA compositions and all time steps, irrespective of moisture ingress (Fig. 3.6 and Fig. 3.7). Upon addition of an $H_2O$ molecule at the salt-alloy interface, no persistent M-O bonds were reported for either RHEA system as well. More specifically, M-F and M-O bond lengths frequently exceed 2.0 Å with modest ICOHP values that exhibit considerable fluctuations, especially for the NbTaMoWV composition. These behaviors are suggestive of minimal orbital overlap between refractory metal atoms and fluorine/oxygen species; hence, negligible chemical bonding, as further evidenced by the partial DOS in Fig. 3.3 and Fig. 3.4. The DOS and COHP analyses emphasize that irrespective of salt purity, the initial corrosion effects of molten salt on RHEA surfaces are minimal, thus reinforcing the chemical inertness of BCC NbTaMoW and NbTaMoWV.

Nonetheless, transient bonding phenomena are identified at specific time frames. For the NbTaMoW-FLiBe interface (Fig. 3.6-a.) at 20 ps, the strongest M–F interactions were observed between Ta20–F3 and Ta8–F46, reflected in shorter bond lengths and moderately negative ICOHP values (e.g., –1.5 to –2.0 eV). At 30 ps, the interaction between Nb20–F14

dominated, characterized by a bond length of 1.781 Å and a significantly negative ICOHP value of –2.345 eV – the most negative of all atoms pairs examined. At 40 ps, a relatively strong interaction was detected between W2–F6, although with a more positive ICOHP compared to Nb20–F14, suggesting a weaker albeit more stable interaction. For the interface between NbTaMoW and the hydrated salt (Fig. 3.7-a.), the Ta8-F3 bond shows greater stability as compared to the Ta-F bonds observed with pure salt (Fig. 3.6-a.), although the ICOHP values remain moderate in magnitude (e.g., –1.0 to –1.5 eV). Notably, Ta8-F3 achieves a negative ICOHP value of -1.613 eV at 40 ps, manifesting the strong interaction between Ta and F. Moreover, W4-O1 demonstrates persistence between 10 and 40 ps, affirming the stability of W interactions with both F and O.

Significantly, it is evident that M-F interactions at distances less than 2.0 Å occur more frequently at the NbTaMoWV-FLiBe interface in both pure and $H_2O$-contaminated salt as compared to NbTaMoW-FLiBe in the same conditions, although these additional interactions do not necessarily confer enhanced strength. As seen in Fig. 3.6-b. and Fig. 3.7-b., V–F bonds manifest at the NbTaMoWV interface with both pure and hydrated salt, respectively; however, they tend to exhibit weak bonding interactions, as evidenced by relatively positive ICOHP values (e.g., 0 to –1.0 eV). Among the more robust transient interactions, Ta–F bonds are particularly noteworthy in pure salt conditions: F47–Ta4 (10–30 ps) and F24–Ta1 (20 ps) exhibit significant overlap. However, the dynamic process of bond formation and dissolution for Ta-F reflects interfacial mobility rather than enduring chemisorption. Upon contact with $H_2O$, the most significant interaction occurs between Nb2-O1 with a corresponding bond length of 1.967 Å and a very negative ICOHP value of -2.006 eV at 20 ps. This substantiates the strong affinity of Nb for O which has been shown to prevail in the early stages of corrosion[101]. Despite this, Nb-F bonding fluctuates considerably with time, emphasizing the dynamism of bonding formation and dissolution in the initial degradation phase.

The electronic structure illustrated by the COHP curves is presented in Fig. 3.8 for designated metal–fluorine bonds at the (100) surfaces of NbTaMoW (top, 40 ps) and NbTaMoWV (bottom, 40 ps) in contact with pure FLiBe at 800 K. The COHP curves are

presented in Fig. 3.9 for designated metal–fluorine and metal-oxygen bonds at the metal interfaces with hydrated FLiBe at 800 K. At the NbTaMoW-FLiBe interface in Fig. 3.8-a., three significant M–F interactions are discerned after 40 ps: Ta20–F3, Nb20–F14, and W2–F6. Among these, W2-F6 exhibited the sharpest bonding peak centered around –7 eV, eluding to a relatively strong covalent character. The COHP profiles for Ta20–F3 and Nb20–F14 illustrate considerably shorter bonding peaks, implying weaker interactions. Taking into consideration the relatively negative ICOHP values observed for Nb-F and Ta-F at previous time frames (Fig. 3.6 and Fig. 3.7), these results emphasize the dynamism and instability of the metal-fluorine bonds. At the NbTaMoW-$H_2O$-FLiBe interface in Fig. 3.9-a., a highly sharp and compact bonding peak is observed for Ta8-F3 well below the Fermi level at -8 eV, reaffirming the reactivity of Ta towards F. A compact, yet lower bonding peak is observed at -4 eV for W4-O1, highlighting the relative stability of W interactions with O.

Conversely, the NbTaMoWV system at 40 ps exhibits a more intricate bonding environment in pure salt conditions (Fig. 3.8-b.), characterized by a broader array of M–F interactions involving V, Ta, Nb, and Mo. Notably, Ta4–F47 and Ta1–F24 manifest robust -COHP peaks below the Fermi level at -7 eV and -8 eV, respectively. These observations are consistent with previous ICOHP and DOS results, underscoring the role of Ta as a crucial bonding center at the RHEA-salt interface and highlighting its affinity towards F. V15–F52, V2-F3 and V3-F16 are also characterized by moderate bonding peaks. Intriguingly, Mo3–F33 exhibits a sharp bonding peak around -5.5 eV, whereas Nb2–F42 shows a weaker bonding contribution at -6 eV. Upon addition of $H_2O$ ((Fig. 3.9-b.), V15-F3 and V3-F47 exhibit modest bonding contributions at -7 eV and -6 eV, respectively.V2-O1 displays an even lower bonding peak at -6 eV, affirming the role of vanadium in modulating interfacial reactivity, albeit with weaker orbital overlap. A significant bonding peak is also observed for Nb2-O1 at -6 eV, highlighting the strength of Nb interactions with F/O. Overall, V engages in more frequent interactions with F/O species at the NbTaMoWV-FLiBe and NbTaMoWV-$H_2O$-FLiBe interface, however, the bonding is more dispersed and generally less robust compared to the concentrated and stronger interactions within the NbTaMoW system.

In summary, analyses of COHP and ICOHP elucidate the following findings: i) Irrespective of $H_2O$ contamination, stable covalent metal–fluoride bonds are absent during the 10–40 ps simulation interval at 800 K, ii) Upon addition of an $H_2O$ molecule, the RHEA-salt interface is completely devoid of stable covalent metal-oxide bonds, iii) Among the transient bonds documented, Nb–F interactions emerge as the strongest, whereas V–F bonds occur at the highest rate but exhibit the weakest bonding interactions, iv) the NbTaMoWV alloy system manifests a higher occurrence of weak metal-fluorine contacts, indicating increased fluorine coordination, albeit without corresponding enhancement in interfacial bonding strength, v) Ta–F bonds demonstrate notable dynamism, with bonds intermittently forming and rupturing, indicative of a fluid and weakly interactive interface. These ephemeral yet measurable interactions conclude that, although the majority of M–F/O contacts are weak or non-bonding, select local geometries, particularly those involving Nb and W, have the potential to temporarily facilitate bonding. The lack of enduring covalent M–F/O bonds across all observed time frames and alloy compositions highlights the limited corrosion of RHEA surfaces in pure and $H_2O$-contaminated FLiBe at elevated temperatures.

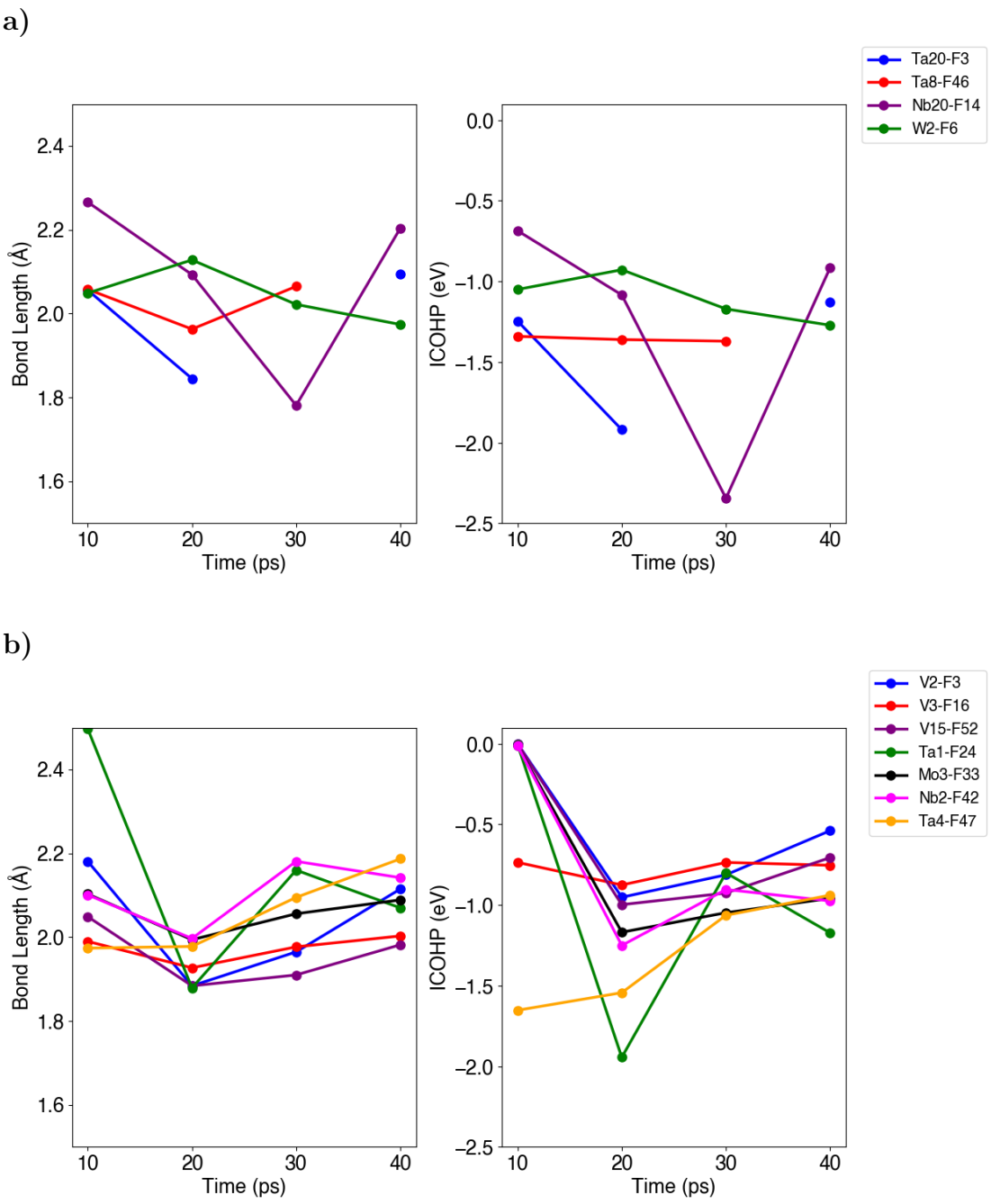



Figure 3.6: The evolution of bond length and integrated crystal orbital Hamilton population (ICOHP) of representative metal fluorides at the a) (100)-NbTaMoW−FLiBe and b) (100)-NbTaMoWV−FLiBe interface at 800 K. The cutoff distance for the atom pair is 3 Å. If the distance between the atom pair exceeds 3 Å, the interatomic interaction is considered insignificant and the bond length and ICOHP are not reported.

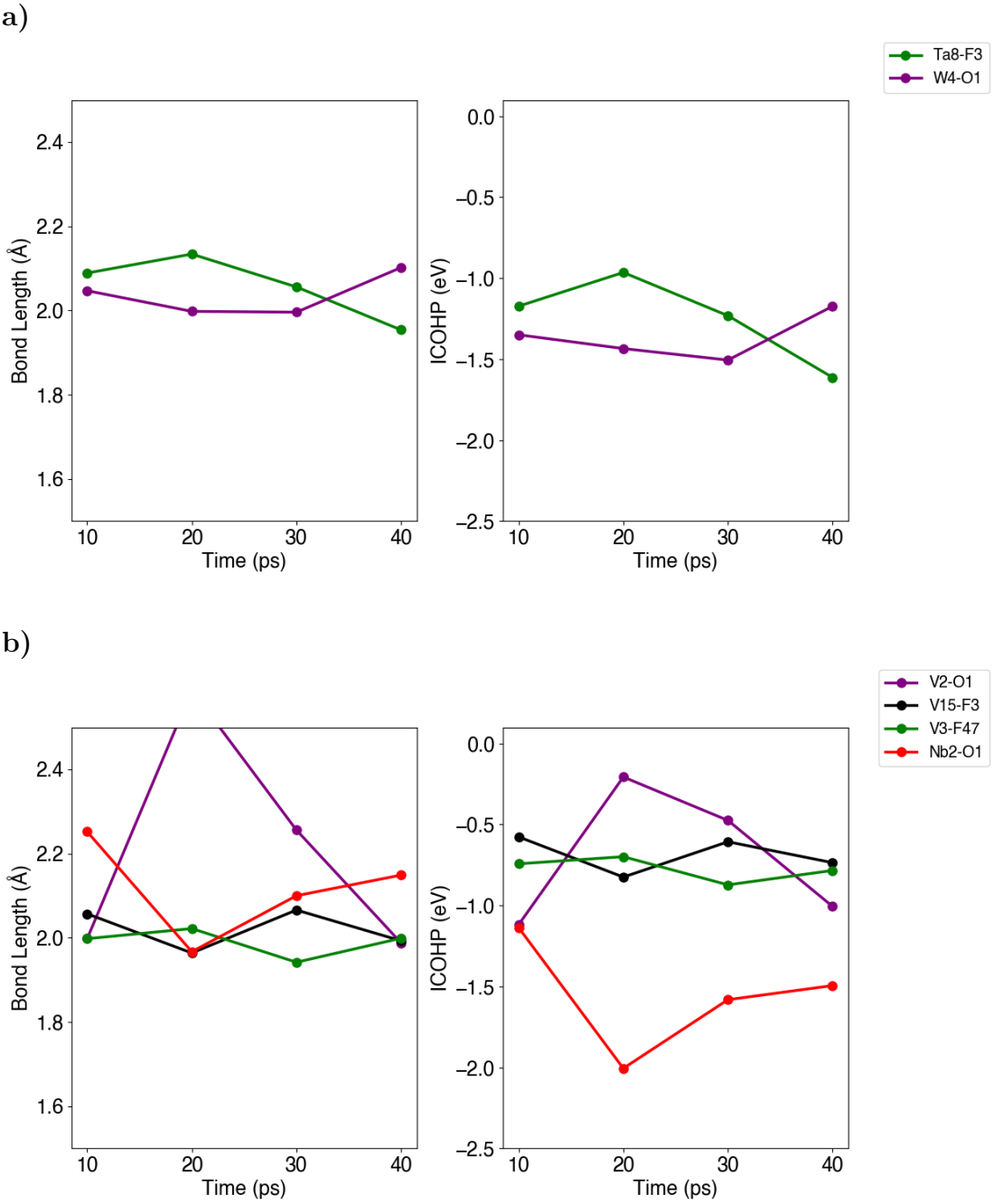



Figure 3.7: The evolution of bond length and integrated crystal orbital Hamilton population (ICOHP) of representative metal fluorides at the a) (100)-NbTaMoW−$H_2O$−FLiBe and b) (100)-NbTaMoWV−$H_2O$−FLiBe interfaces at 800 K. In the above interfacial environments, 1 $H_2O$ molecule was added to the FLiBe salt overlay. The cutoff distance for the atom pair is 3 Å. If the distance between the atom pair exceeds 3 Å, the interatomic interaction is considered insignificant and the bond length and ICOHP are not reported.

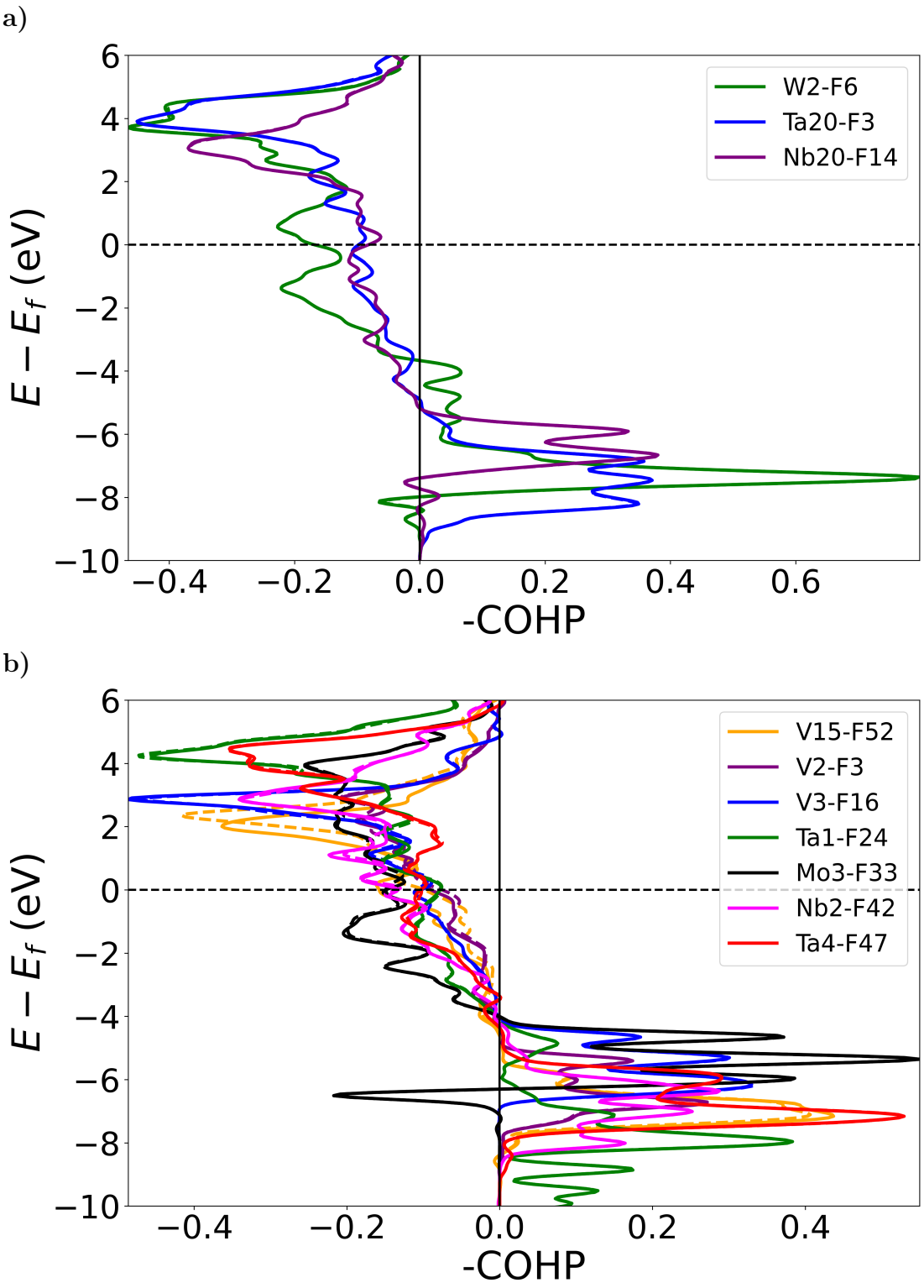



Figure 3.8: Crystal orbital Hamilton population (COHP) analysis of the BCC (100) surfaces of a) NbTaMoW and b) NbTaMoWV in contact with molten FLiBe. The COHP analysis was performed at 800 K after 40 ps of simulation time. The black dotted line represents the Fermi level which is set to 0 eV.

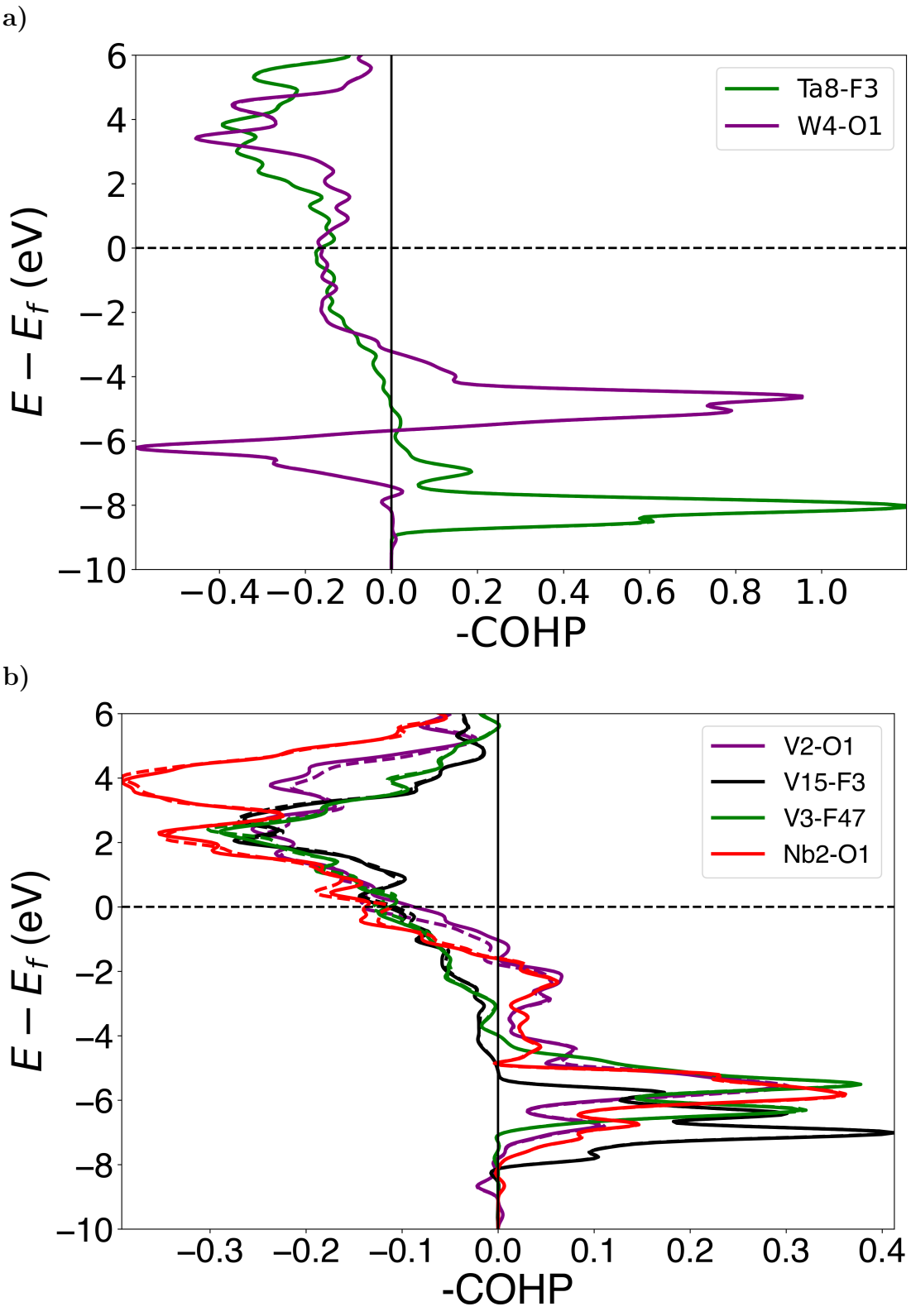



Figure 3.9: Crystal orbital Hamilton population (COHP) analysis of the BCC (100) surfaces of a) NbTaMoW and b) NbTaMoWV in contact with molten FLiBe contaminated with a $H_2O$ molecule. The COHP analysis was performed at 800 K after 40 ps of simulation time. The black dotted line represents the Fermi level which is set to 0 eV.

## 3.4 Electron Localization Function

In order to elucidate the interfacial redox behavior, electron localization function (ELF) analysis was performed for both RHEA compositions in contact with pure and hydrated FLiBe from 10 to 40 ps. By integrating the electron density over distinct atomic sites, the number of valence electrons on each atom was calculated and calibrated against the valence electrons in the initial configuration (at 0 ps). The corresponding change in valence electrons on distinct atoms at the NbTaMoW and NbTaMoWV interfaces with pure FLiBe are detailed in Fig. 3.10 and Fig. 3.11, respectively. The effect of introducing $H_2O$ on the evolution of valence electrons is presented in Fig. 3.12 and Fig. 3.13, respectively. Within this context, a reduction in electron density indicates oxidation, normally observed on transition metals, whereas an increase indicates reduction, predominantly occurring on electronegative fluorine and oxygen atoms. As reported in section 3.3, at the NbTaMoW-FLiBe interface, notwithstanding that Nb20–F14 exhibits the highest bonding strength at 30 ps interface (Fig. 3.6-a.), the Ta20–F3 bond exhibits more pronounced polarization as evidenced by the loss of 0.4 valence electrons from Ta20 between 0 and 20 ps (Fig. 3.10). Nonetheless, both Nb20–F14 and Ta20–F3 become become destabilized with time, ultimately causing the dissociation of Ta20–F3 by 30 ps and Nb20–F14 by 40 ps. This behavior aligns with the considerable electron restoration on the metal sites and simultaneous electron depletion on the fluorine atoms as manifested in the progression of the ELF in Fig. 3.10. Ta20 and Nb20 approach their initial charged state, resulting in complete bond reversal by 30 ps for Ta20 and 40 ps for Nb20. Despite the robust initial bonding observed in the evolution of bond length and ICOHP, Nb20–F14 does not preserve a low reduction potential for an extended period, determining that transient bonding strength does not inherently equate to enduring redox stability. For the NbTaMoW system with the hydrated salt overlay (Fig. 3.12), the significant gain of +0.8 valence electrons on Ta8 after 10 ps suggests rapid dissociation of the Ta8-F3 bond. The subsequent loss of 0.2 valence electrons from Ta8 between 30 and 40 ps implies a renewed interaction between Ta8 and F3. Interestingly, the electron density on W4 and O1 remains relatively constant through out the simulation, especially for W4, highlighting its lower redox activity.

At the NbTaMoWV interface (Fig. 3.11 and Fig. 3.13), similar trends are observed with notable differences due to the addition of vanadium. In pure salt conditions, the V2–F3 bond (Fig. 3.11, top) undergoes rapid dissociation at 10 ps, as indicated by a sharp increase in valence electrons in V2 ( +0.38), corroborating oxidation-induced bond rupture. While the electron density on V3–F16 and V15–F52 appears more stable, ELF data show gradual oxidation of V3 and V15, suggesting that V participates in dynamic but weak bonding interactions with fluorine. Additionally, in Fig. 3.11 (bottom), Ta1 shows the most pronounced charge depletion at 20 ps, aligning with the peak in Ta1–F24 bond strength (Fig. 3.6-b.), suggesting a more polarized and chemically active site. Analogous to the ELF evolution observed for the NbTaMoW system, tantalum undergoes the most significant electron loss amongst all constituent metals, suggesting a higher oxidation susceptibility. This observation aligns with the elevated electronic energy in the conduction band contributed by the Ta d-orbitals, signifying a higher tendency for Ta to donate electrons to electronegative species such as fluorine. In hydrated salt, the rupture of the V2-O1 bond observed in Fig. 3.7-b. at 20 ps is depicted by the corresponding loss of +0.4 valence electrons from O1 between 0 and 20 ps in Fig. 3.13 (bottom). Furthermore, a decrease of 0.6 valence electrons on F47 and simultaneous gain of 0.1 electrons on V3 at 20 ps is associated with V3-F47 bond dissolution, highlighting the bond fragility of V-F and V-O. The loss of 0.3 valence electrons from Nb2 between 10 and 20 ps is representative of the enhanced Nb2-O1 interaction at 20 ps in Fig. 3.7-b. after which the charge on Nb2 stabilizes. Despite the addition of moisture to the molten salt environment, metal-fluorine and metal-oxygen bonds remain primarily ephemeral and weak.

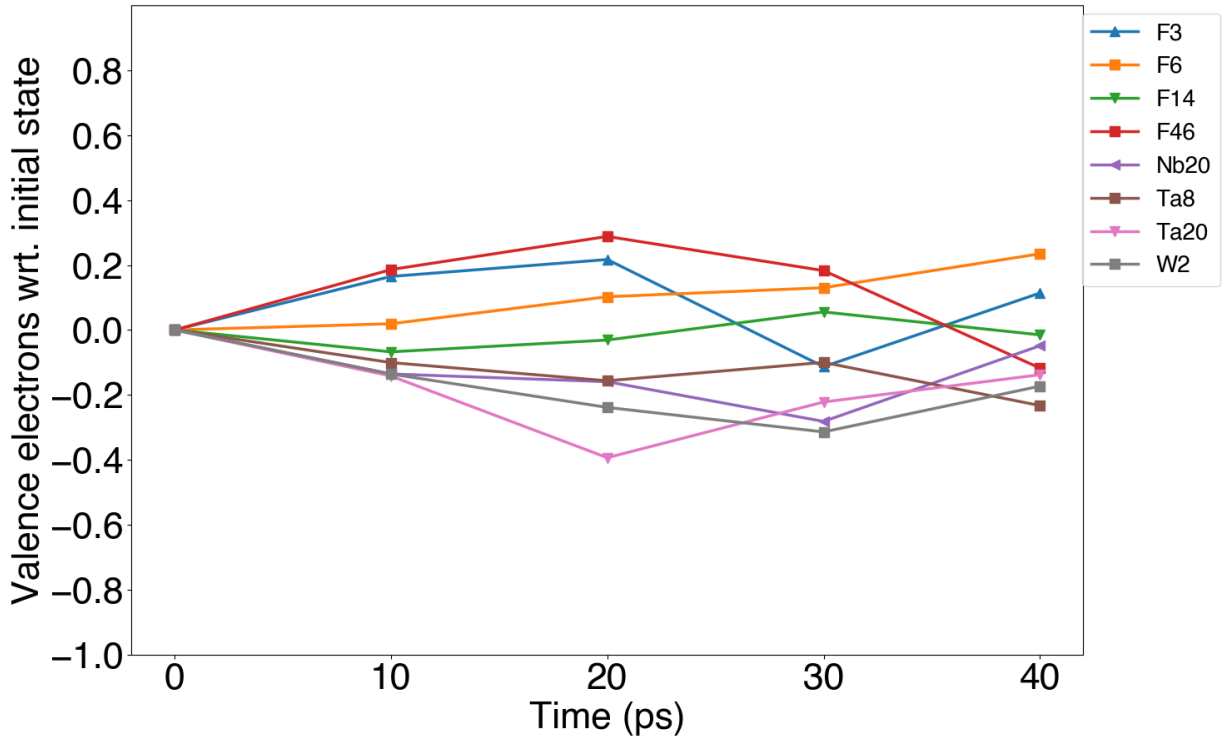



Figure 3.10: Change in valence electrons of representative surface atoms at the interface between (100)-NbTaMoW and pure FLiBe at 800 K. The number of valence electrons at a specified atomic site is normalized to the valence electrons at 0 ps.

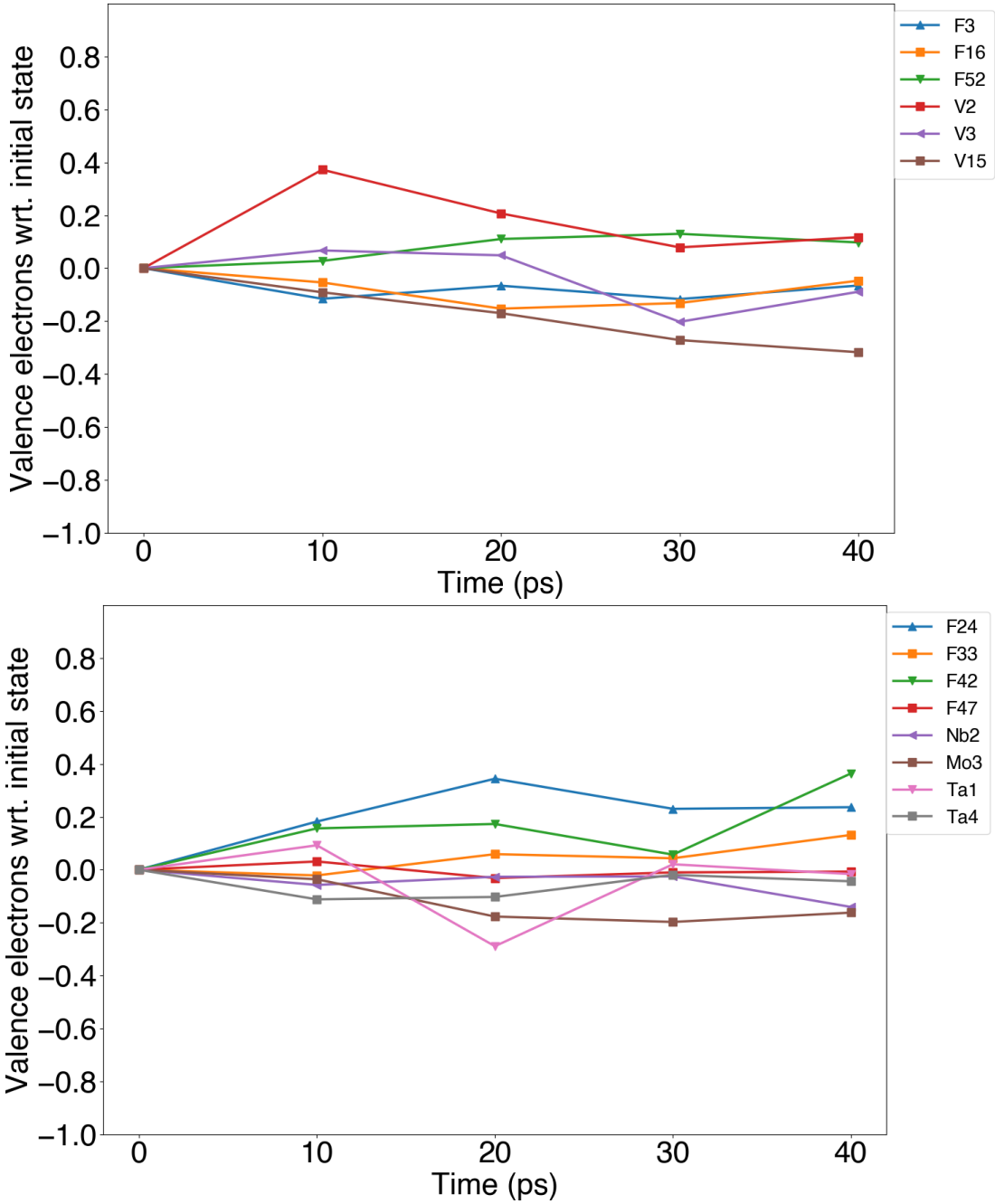



Figure 3.11: Change in valence electrons of representative surface atoms at the interface between (100)-NbTaMoWV and pure FLiBe at 800 K. The change in valence electrons for atoms participating in V-F bonds is at the top and the atoms involved in other metal fluoride bonds are at the bottom. The number of valence electrons at a specified atomic site is normalized to the valence electrons at 0 ps.

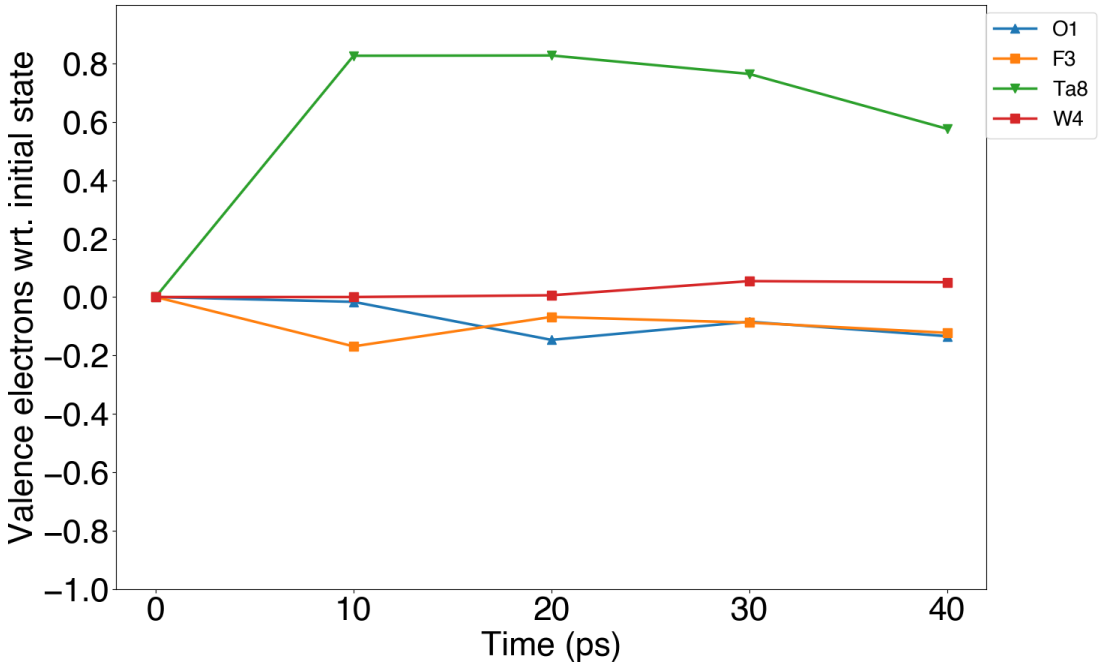



Figure 3.12: Change in valence electrons of representative surface atoms at the interface between (100)-NbTaMoW and $H_2O$-contaminated FLiBe at 800 K. The number of valence electrons at a specified atomic site is normalized to the valence electrons at 0 ps.

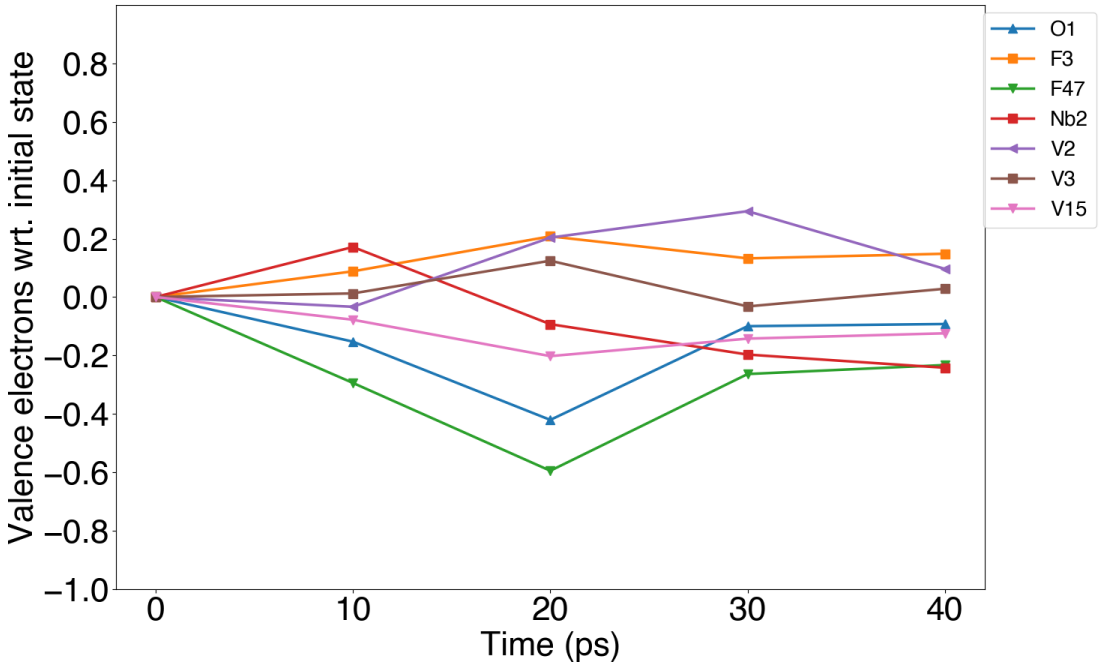


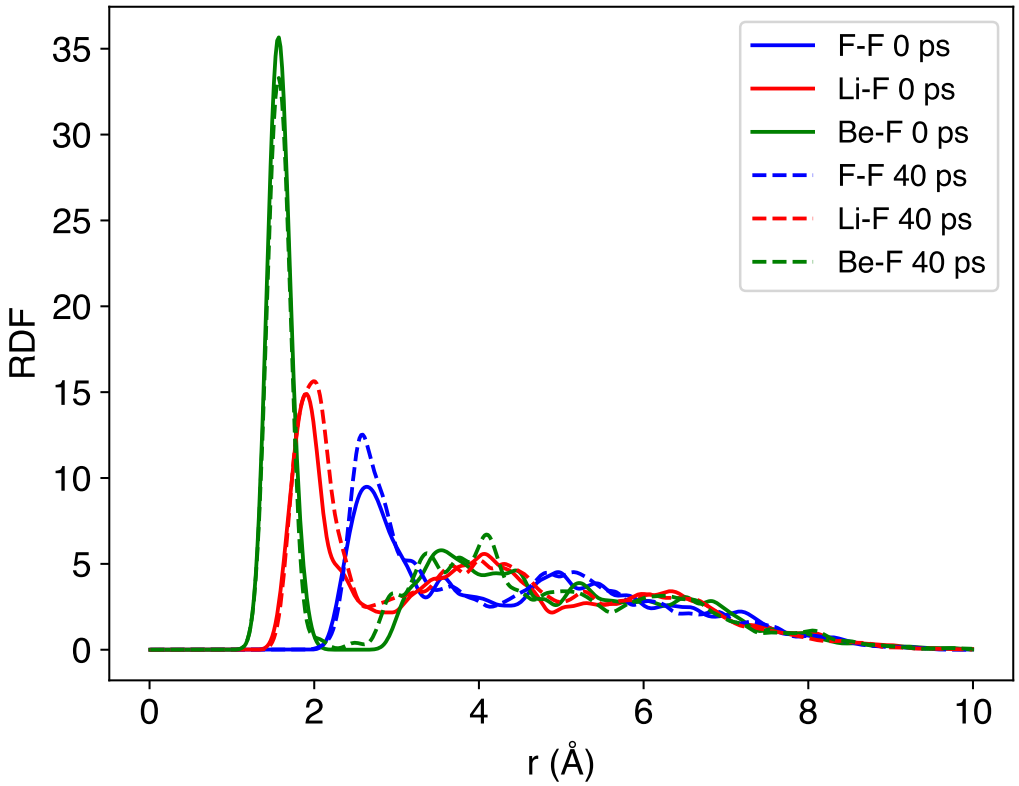

Figure 3.13: Change in valence electrons of representative surface atoms at the interface between (100)-NbTaMoWV and $H_2O$-contaminated FLiBe at 800 K. The number of valence electrons at a specified atomic site is normalized to the valence electrons at 0 ps.

## 3.5 Effect of RHEAs on Salt Chemistry

The radial distribution function was calculated for pure and hydrated FLiBe salt after contact with both (100)-NbTaMoW and -NbTaMoWV slabs at 800 K to deduce the effect of the RHEAs on the salt chemistry (Fig. 3.15). The structure of the salt remains mainly unaffected in both its pure state and contaminated state after exposure to both RHEA surfaces for 40 ps at 800 K, which is expected in such a short simulation time. FLiBe retains its liquid phase, as shown by the short-range ordering in Fig. 3.15. Both NbTaMoW and NbTaMoWV-FLiBe interfaces exhibit a small decrease in the Be-F bonding strength after 40 ps. Furthermore, there is an increase in the F-F bonding strength in NbTaMoW-FLiBe and a decrease in the F-F bonding strength in NbTaMoWV-FLiBe. The shift in the Li-F bonding strength remains insignificant at both interfaces.

Upon exposure to 1 $H_2O$ molecule, there is negligible change in the Be-F or Li-F peak after 40 ps of simulation, manifesting the structural integrity of FLiBe irrespective of hydration and subsequent contact with RHEA surfaces. At the NbTaMoWV-H2O-FLiBe interface, there appears to be a narrowing of the F-F peak, implying a greater local ordering of FLiBe after 40 ps. This effect is attributed to the equilibration of the salt structure between 0 and 40 ps at 800 K. All in all, FLiBe retains its strong short range ordering, despite contamination with $H_2O$.

a)




b)

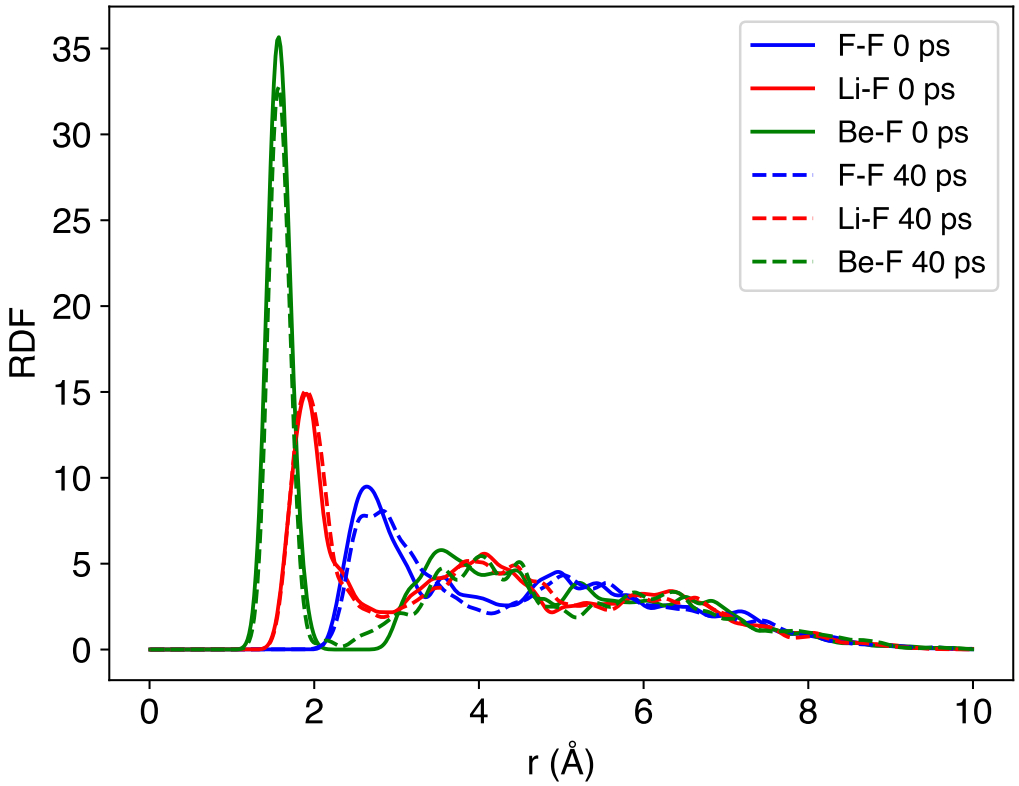
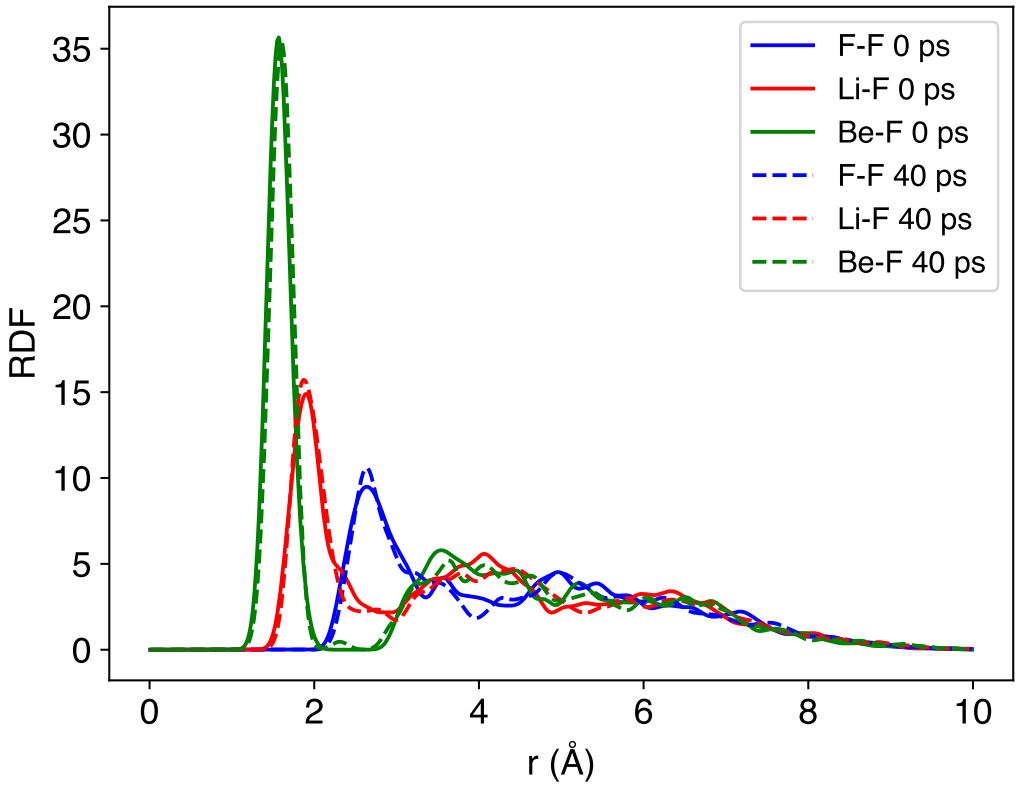



Figure 3.14: Radial distribution function of FLiBe salt after contact with a) (100)-NbTaMoW and b) -NbTaMoWV at 800 K for 40 ps.

a)




b)

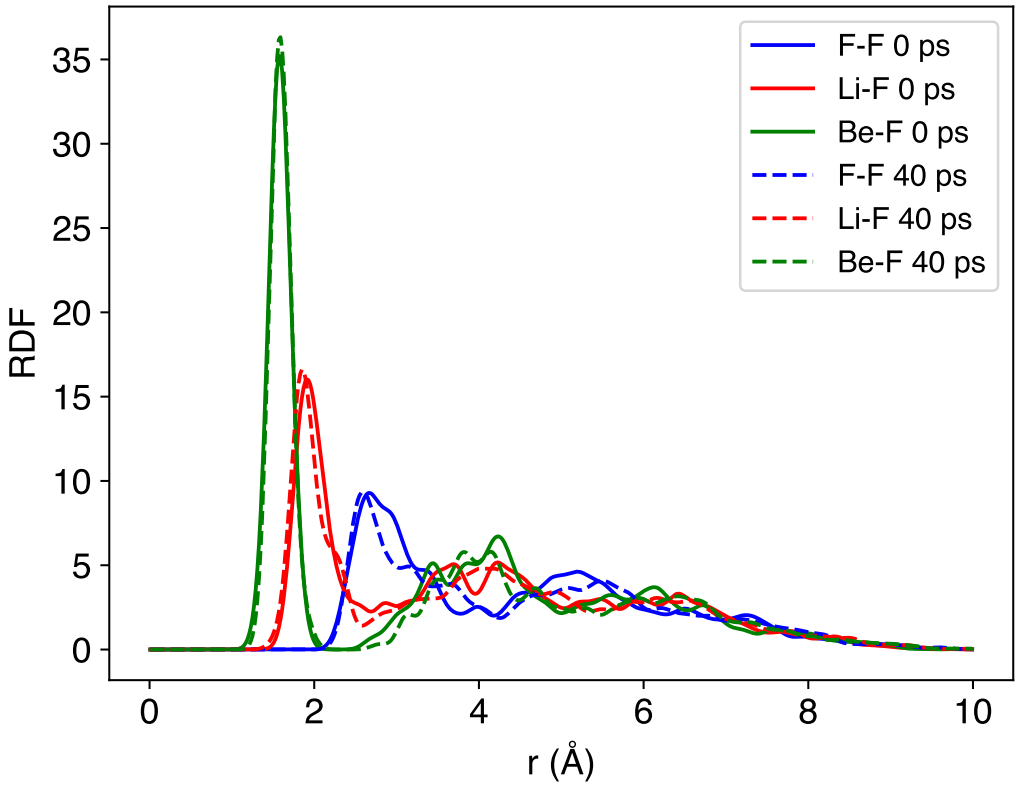



Figure 3.15: Radial distribution function of $H_2O$-contaminated FLiBe salt after contact with a) (100)-NbTaMoW and b) -NbTaMoWV at 800 K for 40 ps.

## 3.6 Conclusions

In this study, the corrosion behavior of NbTaMoW and NbTaMoWV RHEAs in pure and $H_2O$-contaminated molten salt conditions was examined using Density Functional Theory (DFT) and Ab Initio Molecular Dynamics (AIMD) simulations. Electronic structure analyses, comprising of Density of States (DOS), Crystal Orbital Hamilton Population (COHP), and Electron Localization Function (ELF) partitioning, were employed to reveal the bonding characteristics and charge distribution at the interface. Our key findings are summarized as follows: (i) *$H_2O$ addition*: The effects of $H_2O$ on the preliminary stages of RHEA degradation are negligible - no significant differences are observed in the electronic and bonding analyses between the pure salt and $H_2O$-contaminated salt interface after 40 ps at 800 K. (ii) *Element-Specific Oxidation Behavior*: Ta is the most susceptible to oxidation, as evidenced by significant shifts of d-orbitals to higher energies, unstable Ta–F bonds (as shown by COHP), and substantial electron transfer to fluorine (confirmed by ELF analysis). Mo, in contrast, displays the smallest shift in d-states and minimal interaction with fluorine, suggesting greater resistance to oxidation. Nb forms the strongest interactions with fluorine and oxygen, as indicated by the relatively short bond lengths and negative ICOHP. (iii) *Effect of Vanadium Addition*: V forms weak bonds with fluorine (ICOHP > -1.0 eV), indicating minimal redox activity and low reactivity. The integration of vanadium into the NbTaMoW alloy (i.e., forming NbTaMoWV) results in reduced electronic excitation and weaker metal–fluorine interactions, suggesting enhanced structural and chemical stability. (iv) *Interface Stability*: The NbTaMoW interface, shows stronger Nb–F interactions and greater d-electron energy shifts, indicating a higher tendency towards oxidation compared to the NbTaMoWV interface. This observation reinforces the conclusion that vanadium enhances corrosion resistance by strengthening metal–metal bonding and reducing the availability of reactive sites. (v) *Salt Chemistry*: The structure of the FLiBe salt remains largely unaffected in the presence of NbTaMoW and NbTaMoWV after 40 ps at 800 K. Overall, the incorporation of vanadium into NbTaMoW-based HEAs appears to mitigate corrosion by reducing oxidation susceptibility and stabilizing the alloy's electronic structure at the molten salt interface. These insights highlight the potential of

tailored compositional adjustments in HEAs for improved performance in extreme environments. Due to the high computational cost of AIMD, the short simulation time (40 ps) and small system size (80 atoms) in this corrosion investigation remain a drawback. Future studies would benefit from the parameterization of a ReaxFF[102] force field for the FLiBe–NbTaMoW and FLiBe–NbTaMoWV interfaces. This would permit for longer time-scale simulations ($>$ 100 ps) and larger system sizes ($>$ 2000 atoms) using classical molecular dynamics which would permit for accurate prediction of corrosion rates.

# References


[1] R. S. El-Emam, A. Constantin, R. Bhattacharyya, H. Ishaq and M. E. Ricotti, *Renew. Sustain. Energy Rev.*, 2024, **192**, 114157.

[2] S. Aslam, S. Rani, K. Lal, M. Fatima, T. Hardwick, B. Shirinfar and N. Ahmed, *Green Chemistry*, 2023, **25**, 9543–9573.

[3] US DOE Nuclear Energy Research Advisory Committee and the Generation IV International Forum, *A Technology Roadmap for Generation IV Nuclear Energy Systems*, http://www.ne.doe.gov/genIV/documents/gen_iv_roadmap.pdf.

[4] G.I.F Portal, *Molten Salt Reactors (MSRs)*, https://www.gen-4.org/generation-iv-criteria-and-technologies/molten-salt-reactors-msr.

[5] Oak Ridge National Laboratory (ORNL), *Molten Salt Reactor*, https://www.ornl.gov/molten-salt-reactor.

[6] E. Midgley, *What are Molten Salt Reactors?*, 2025, https://www.iaea.org/newscenter/news/what-are-molten-salt-reactors.

[7] M. McClearn, *Terrestrial Energy's Molten-Salt Reactor Clears Prelicensing Review.*, 2023, https://www.theglobeandmail.com/business/article-terrestrial-energys-molten-salt-reactor-clears-prelicensing-review/.

[8] O. Benes and J. M. Konings, *Molten Salt Reactor Fuel and Coolant*, Elsevier Ltd., 2012, pp. 259–289.

[9] C. N. Bahri, W. M. Al-Areqi, M. Ruf, I. F. M and A. A. Majid, *AIP Conf. Proc*, 2017, **1802**, 040008.

[10] R. Yoshioka, M. Kinoshita and I. Scott, *Molten Salt Reactors and Thorium Energy*, Woodhead Publishing Series in Energy, 2017, p. 189–207.

[11] World Nuclear Association, *Molten Salt Reactors*, 2024, https://world-nuclear.org/information-library/current-and-future-generation/molten-salt-reactors.

[12] G. Martinez-Guridi, L. Peguero and F. Reitsma, *STATUS OF MOLTEN SALT REACTOR TECHNOLOGY*, International Atomic Energy Agency (IAEA) Technical Report 489, 2023.

[13] G. Locatelli, M. Mancini and N. Todeschini, *Energy Policy*, 2013, **61**, 1503–1520.

[14] T. J. Dolan, *Molten Salt Reactors and Thorium Energy*, Woodhead Publishing Series in Energy, 2017, pp. 1–12.

[15] R. C. Briant and A. M. Weinberg, *Nucl. Sci. Eng.*, 1957, **2**, 797–803.

[16] V. V. Ignatiev, M. V. Kormilitsyn, L. A. Kormilitsyna, Y. M. Semchenkov, Y. S. Fedorov, O. S. Feinberg, O. V. Kryukov and A. V. Khaperskaya, *At Energy*, 2019, **125**, 279–283.

[17] C. Degueldre, J. Findlay, D. Cheneler, S. Sardar and S. Green, *Appl. Radiat. Isot.*, 2024, **205**, 111146.

[18] J. Barnes, R. Coutts, T. Horne and J. Thai, *PAM Review Energy Science & Technology*, 2019, **6**, 38–55.

[19] S. Attarian, D. Morgan and I. Szlufarska, *J. Mol. Liq.*, 2022, **368**, 120803.

[20] A. Redkin, A. Khudorozhkova, E. Il'ina, S. Pershina, P. Mushnikov, A. Isakov, Y. Zaikov, A. Kataev and M. Laptev, *J. Mol. Liq.*, 2021, **341**, 117215.

[21] W. R. Grimes, D. R. Cuneo, F. F. Blankenship, G. W. Keilholtz, H. F. Poppendiek and M. T. Robinson, *Molten-Salt Reactor for Nuclear Fuel Cycle Closure on All Actinides.*, Addison-Wesley, 1958.

[22] A. Leong, J. Zhang and S. D. Rountree, *High Temp. Corros. Mater*, 2023, **99**, 375–397.

[23] A. E. Danon, O. Muránsky, I. Karatchevtseva, Z. Zhang, Z. J. Li, N. Scales, J. J. Kruzic and L. Edwards, *Corros. Sci.*, 2020, **164**, 108306.

[24] *Corrosion in Molten Salt Reactors*, https://madcor.neep.wisc.edu/previous-work/corrosion-in-molten-salt-reactors, The UW-Madison MAterials Degradation under COrrosion and Radiation (MADCOR).

[25] K. Sridharan and T. R. Allen, *Molten salts chemistry*, Elsevier, 2013, pp. 241–267.

[26] L. C. Olson, J. W. Ambrosek, K. Sridharan, M. H. Anderson and T. R. Allen, *J. Fluor. Chem.*, 2009, **130**, 67–73.

[27] S. Guo, J. Zhang, W. Wu and W. Zhou, *Prog. Mater. Sci.*, 2018, **97**, 448–487.

[28] K. M. Sankar and P. M. Singh, *Corros. Sci.*, 2023, **213**, 110977.

[29] O. Muránsky, C. Yang, H. Zhu, I. Karatchevtseva, P. Sláma, Z. Nový and L. Edwards, *Corros. Sci.*, 2019, **159**, 108087.

[30] C. Sequeira, *High Temperature Corrosion in Molten Salts*, Trans Tech Publications, 2003.

[31] J. R. DiStefano, J. H. DeVan, J. R. Keiser, R. L. Klueh and W. P. Eatherly, *Materials considerations for molten salt accelerator-based plutonium conversion systems*, Oak ridge national lab. technical report, 1995.

[32] A. K. Misra and J. D. Whittenberger, 22nd Intersociety Energy Conversion Engineering Conference, 1987, p. 9226.

[33] S. Bell, T. Steinberg and G. Will, *Renew. Sustain. Energy Rev.*, 2019, **114**, 109328.

[34] T. Ishitsuka and K. Nose, *Corr. Sci.*, 2002, **44**, 247–263.

[35] K. H. Stern, *Metal oxide solubility and molten salt corrosion*, Naval Research Laboratory Technical Report NUL Memorandum Report 4772, 1982.

[36] C. F. Baes, *J. Nucl. Mater.*, 1974, **51**, 149–162.

[37] G. Ting, *PhD thesis*, Univ. of Tennessee, Knoxville, 1973.

[38] B. D'Souza, W. Zhuo, Q. Yang, A. Leong and J. Zhang, *Corr. Sci.*, 2021, **187**, 109483.

[39] S. S. Raiman and S. Lee, *J. Nucl. Mater.*, 2018, **511**, 523—-535.

[40] H. Arkoub and M. Jin, *Comput. Mater. Sci.*, 2025, **255**, 113903.

[41] H. L. Chan, E. Romanovskaia, J. Qiu, P. Hosemann and J. R. Scully, *npj Mater Degrad*, 2022, **6**, 1–10.

[42] C.-L. Ren, H. Han, W.-B. Gong, C.-B. Wang, W. Zhang, C. Cheng, P. Huai and Z.-Y. Zhu, *J. Nucl. Mater.*, 2016, **478**, 295–302.

[43] E. P. George, D. Raabe and R. O. Ritchie, *Nat Rev Mater*, 2019, **4**, 515—-534.

[44] L. Čelko, L. Klakurková and J. Švejcar, *Defect Diffus. Forum*, 2010, **297-301**, 771–777.

[45] W. Callister, *Impurities in Solids, in: Materials Science and Engineering and Introduction, 7th ed.*, John Wiley and Sons, Inc., 2007, p. 83–85.

[46] J. W. Yeh, S. K. Chen, S. J. Lin, J. Y. Gan, T. S. Chin, T. T. Shun, C. H. Tsau and S. Y. Chang, *Adv. Eng. Mater.*, 2004, **6**, 299—303.

[47] F. Otto, Y. Yang, H. Bei and E. P. George, *Acta Mater.*, 2013, **61**, 2628–2638.

[48] B. Cantor, I. T. H. Chang, P. Knight and A. J. B. Vincent, *Mater Sci Eng A*, 2004, **375-377**, 213–218.

[49] M. C. Troparevsky, M. J. R, P. R. C. Kent, A. R. Lupini and G. M. Stocks, *Phys. Rev. X*, 2015, **5**, 011041.

[50] T. Li, D. Wang, S. Zhang and J. Wang, *Metals*, 2023, **13**, 363.

[51] W. Hsu, C. W. Tsai, A. C. Yeh and J. W. Yeh, *Nat Rev Chem*, 2024, **8**, 471–485.

[52] N. A. P. K. Kumar, C. Li, K. J. Leonard, H. Bei and S. J. Zinkle, *Acta Mater.*, 2016, **113**, 230–244.

[53] H. Shi, A. Jianu, R. Fetzer, D. V. Szabó, S. Schlabach, A. Weisenburger, C. Tang, A. Heinzel, F. Lang and G. Müller, *Corros. Sci.*, 2021, **189**, 109593.

[54] O. N. Senkov, G. B. Wilks, J. M. Scott and D. B. Miracle, *Intermetallics*, 2011, **19**, 698–706.

[55] L. Bai, Y. Hu, X. Liang, Y. Tong, J. Liu, Z. Zhang, Y. Li and J. Zhang, *J. Alloys Compd.*, 2021, **857**, 157542.

[56] Y. Qiu, S. Thomas, M. A. Gibson, H. L. Fraser and N. Birbilis, *npj mater. degrad.*, 2017, **1**, 15.

[57] Y. Y. Chen, T. Duval, U. D. Hung, J. W. Yeh and H. C. Shih, *Corros. Sci.*, 2005, **47**, 2257–2279.

[58] Y. Qiu, M. Gibson, H. Fraser and N. Birbilis, *Mater. Sci. Technol.*, 2015, **31**, 1743284715Y.000.

[59] C. P. Lee, C. C. Chang, Y. Y. Chen, J. W. Yeh and H. C. Shih, *Corros. Sci.*, 2008, **50**, 2053–2060.

[60] A. Mazzarolo, M. Curioni, A. Vicenzo, P. Skeldon and G. Thompson, *Electrochim. Acta*, 2012, **75**, 288–295.

[61] K. Sieradzki and R. C. Newman, *J. Electrochem. Soc*, 1986, **133**, 1979–1980.

[62] Y. L. Chou, J. W. Yeh and H. C. Shih, *Corros. Sci.*, 2010, **52**, 2571–2581.

[63] X.-W. Qiu and C.-G. Liu, *J. Alloys Compd.*, 2013, **553**, 216–220.

[64] Y.-J. Hsu, W.-C. Chiang and J.-K. Wu, *Mater. Chem. Phys.*, 2005, **92**, 112–117.

[65] M. Elbakhshwan, W. Doniger, C. Falconer, M. Moorehead, C. Parkin, C. Zhang, K. Sridharan and A. Couet, *Sci. Rep.*, 2019, **9**, 18993.

[66] A. Schneider, D. Andersson and Y. Zhang, *Commun. Mater.*, 2024, **5**, 91.

[67] A. Katai, A. Varma and C. Tetsassi Feugmo, *Faraday Discuss.*, 2025.

[68] S. Blinder, *Advanced Physical Chemistry: A Survey of Modern Theoretical Principles*, The Macmillan Company, 1969.

[69] R. Sadus, *Molecular Simulation of Fluids: Theory, Algorithms, Object-Orientation, and Parallel Computing*, Elsevier, 2024.

[70] M. J. Buehler, *Introduction to classical molecular dynamics (cont'd)*, 2007.

[71] D. Marenduzzo, *Thermostats in Molecular Dynamics*, https://www2.ph.ed.ac.uk/~dmarendu/MVP/MVP03.pdf, Lecture notes, School of Physics.

[72] S. Nosé, *Mol. Phys.*, 2018, **52**, 255–268.

[73] A. Schultz and D. Kofke, *J. Chem. Phys.*, 2018, **149**, 124109.

[74] D. Sholl and J. Steckel, *Density Functional Theory: A Practical Introduction*, John Wiley  Sons, Inc., 2023.

[75] D. Marx and J. Hutter, *Ab Initio Molecular Dynamics: Basic Theory and Advanced Methods*, Cambridge University Press, 2009.

[76] Perdew, Burke and Ernzerhof, *Phys. Rev. Lett.*, 1996, **77**, 3865–3868.

[77] R. Hummel, *Electronic Properties of Materials*, Springer, 2012.

[78] V. L. Deringer, A. L. Tchougréeff and R. Dronskowski, *J. Phys. Chem. A*, 2011, **115**, 5461–5466.

[79] A. D. Becke and N. E. Edgecombe, *J Chem. Phys.*, 1990, **92**, 5397.

[80] A. Savin, R. Nesper, S. Wengert and T. Fassler, *Angew. Chem. Int. Ed. Engl.*, 1997, **36**, 1808–1832.

[81] A. P. Thompson, H. M. Aktulga, R. Berger, D. S. Bolintineanu, W. M. Brown, P. S. Crozier, P. J. in 't Veld, A. Kohlmeyer, S. G. Moore, T. D. Nguyen, R. Shan, M. J. Stevens, J. Tranchida, C. Trott and S. J. Plimpton, *Comput. Phys. Commun.*, 2022, **271**, 108171.

[82] J. Byggmästar, K. Nordlund and F. Djurabekova, *Phys. rev B*, 2021, **104**, 104101.

[83] J. Byggmästar, K. Nordlund and F. Djurabekova, *Phys. Rev. Mater.*, 2022, **6**, 083801.

[84] A. V. Shapeev, *Multiscale Modeling and Simulation*, 2016, **14**, 1153–1173.

[85] M. Ångqvist, W. A. Muñoz, J. M. Rahm, E. Fransson, C. Durniak, P. Rozyczko, T. H. Rod and P. Erhart, *Adv. Theory Simul.*, 2019, 1900015.

[86] L. Martínez, R. Andrade, E. G. Birgin and J. M. Martínez, *J. Comput. Chem.*, 2009, **30**, 2157–2164.

[87] H. L. W. Romatoski R R, *Ann. Nucl. Energy*, 2017, **109**, 635–647.

[88] G. Kresse and J. Furthmüller, *Phys. Rev. B*, 1996, **54**, 11169–11186.

[89] S. Grimme, J. Antony, S. Ehrlich and H. Krieg, *J. Phys. Chem.*, 2010, **132**, 154104.

[90] S. Maintz, V. L. Deringer, A. L. Tchougréeff and R. Dronskowski, *J. Comput. Chem.*, 2016, **37**, 1030–1035.

[91] A. Otero-de-la Roza, E. R. Johnson and V. Luaña, *Comput. Phys. Commun.*, 2014, **185**, 1007–1018.

[92] K. Momma and F. Izumi, *J. Appl. Crystallogr.*, 2011, **44**, 1272–1276.

[93] A. Stukowski, *Modelling Simul. Mater. Sci. Eng.*, 2010, **18**, 015012.

[94] C. L. Fu and K. M. Ho, *Phys. Rev. B*, 1983, **28**, 5480–5486.

[95] *Webelements*, http://www.webelements.com.

[96] D. Fernández-Pello, J. M. Fernández-Díaz, M. A. Cerdeira, C. González and R. Iglesias, *Mater. Today Commun.*, 2020, **24**, 101323.

[97] P. Borges, R. Ritchie and M. Asta, *Sci. Adv.*, 2024, **10**, year.

[98] A. P. Sutton, *Electronic Structure of Materials*, Oxford University Press, 1993.

[99] Y. J. Hu, G. Zhao, B. Zhang, C. Yang, M. Zhang, Z. K. Liu, X. Qian and L. Qi, *Nat. Commun*, 2019, **10**, 4484.

[100] Y. L. Hu, L. H. Bai, Y. G. Tong, D. Y. Deng, X. B. Liang, J. Zhang, Y. J. Li and Y. X. Chen, *J. Alloys Compd.*, 2020, **827**, 153963.

[101] R. Su, H. Zhang, G. Ouyang, L. Liu and D. D. Johnson, *Acta Mater.*, 2023, **246**, 118719.

[102] T. P. Senftle, S. Hong, M. M. Islam, S. B. Kylasa, Y. Zheng, Y. K. Shin, C. Junkermeier, R. Engel-Herbert, M. J. Janik, H. M. Aktulga, T. Verstraelen, A. Grama and A. C. T. van Duin, *npj Comput Mater*, 2016, **2**, 15011.

[103] P. E. Blöchl, *Phys. rev B*, 1994, **50**, 17953–17979.

[104] R. Dronskowski and P. E. Bloechl, *J. Phys. Chem.*, 1993, **97**, 8617–8624.

# APPENDICES

# Appendix A

# Electronic, Bonding and Charge Transfer Analyses

Table A.1: Bond lengths and ICOHP values for (100)-NbTaMoW slab in contact with FLiBe at 10, 20, 30, and 40 ps.

| **Bond** | **Bond Length (Å)** | | | | **ICOHP (Spin up)** | | | | **ICOHP (Spin down)** | | | |
|---|---|---|---|---|---|---|---|---|---|---|---|---|
| | **10 ps** | **20 ps** | **30 ps** | **40 ps** | **10 ps** | **20 ps** | **30 ps** | **40 ps** | **10 ps** | **20 ps** | **30 ps** | **40 ps** |
| F3-Ta20 | 2.056 | 1.845 | N/A | 2.095 | -1.246 | -1.920 | N/A | -1.129 | -1.247 | -1.923 | N/A | -1.130 |
| F46-Ta8 | 2.058 | 1.963 | 2.065 | N/A | -1.341 | -1.361 | -1.371 | N/A | -1.344 | -1.358 | -1.371 | N/A |
| F6-W2 | 2.049 | 2.128 | 2.022 | 1.974 | -1.050 | -0.928 | -1.171 | -1.272 | -1.051 | -0.928 | -1.171 | -1.273 |
| F14-Nb20 | 2.266 | 2.093 | 1.781 | 2.204 | -0.686 | -1.084 | -2.345 | -0.914 | -0.687 | -1.083 | -2.346 | -0.913 |

Table A.2: Bond lengths and ICOHP values for (100)-NbTaMoWV slab in contact with FLiBe at 10, 20, 30, and 40 ps.

| **Bond** | **Bond Length (Å)** | | | | **ICOHP (Spin up)** | | | | **ICOHP (Spin down)** | | | |
|---|---|---|---|---|---|---|---|---|---|---|---|---|
| | **10 ps** | **20 ps** | **30 ps** | **40 ps** | **10 ps** | **20 ps** | **30 ps** | **40 ps** | **10 ps** | **20 ps** | **30 ps** | **40 ps** |
| F16–V3 | 1.990 | 1.927 | 1.977 | 2.003 | –0.736 | –0.876 | –0.736 | -0.754 | –0.728 | –0.874 | –0.723 | -0.753 |
| F3–V2 | 2.181 | 1.884 | 1.965 | 2.115 | 0.000 | –0.952 | –0.813 | -0.539 | 0.000 | –0.949 | –0.810 | -0.547 |
| F42–Nb2 | 2.101 | 1.997 | 2.181 | 2.142 | –0.013 | –1.251 | –0.904 | -0.975 | –0.014 | –1.252 | –0.904 | -0.971 |
| F47–Ta4 | 1.974 | 1.978 | 2.095 | 2.187 | –1.653 | –1.544 | –1.064 | -0.939 | –1.654 | –1.546 | –1.069 | -0.941 |
| F24–Ta1 | 2.497 | 1.879 | 2.160 | 2.070 | –0.005 | –1.945 | –0.801 | -1.173 | –0.005 | –1.951 | –0.803 | -1.174 |
| F33–Mo3 | 2.103 | 1.994 | 2.056 | 2.089 | –0.013 | –1.169 | –1.048 | -0.959 | –0.012 | –1.167 | –1.043 | -0.958 |
| F52–V15 | 2.049 | 1.884 | 1.910 | 1.982 | 0.000 | –0.998 | –0.926 | -0.706 | 0.000 | –0.998 | –0.928 | -0.771 |

Table A.3: Bond lengths and ICOHP values for (100)-NbTaMoW slab in contact with FLiBe contaminated with a $H_2O$ molecule at 10, 20, 30, and 40 ps.

| **Bond** | **Bond Length (Å)** | | | | **ICOHP (Spin up)** | | | | **ICOHP (Spin down)** | | | |
|---|---|---|---|---|---|---|---|---|---|---|---|---|
| | **10 ps** | **20 ps** | **30 ps** | **40 ps** | **10 ps** | **20 ps** | **30 ps** | **40 ps** | **10 ps** | **20 ps** | **30 ps** | **40 ps** |
| O1-W4 | 2.047 | 1.998 | 1.996 | 2.102 | -1.350 | -1.435 | -1.506 | -1.174 | -1.353 | -1.438 | -1.505 | -1.174 |
| F3-Ta8 | 2.089 | 2.134 | 2.056 | 1.954 | -1.173 | -0.965 | -1.232 | -1.613 | -1.174 | -0.967 | -1.233 | -1.616 |

Table A.4: Bond lengths and ICOHP values for (100)-NbTaMoWV slab in contact with FLiBe contaminated with a $H_2O$ molecule at 10, 20, 30, and 40 ps.

| **Bond** | **Bond Length (Å)** | | | | **ICOHP (Spin up)** | | | | **ICOHP (Spin down)** | | | |
|---|---|---|---|---|---|---|---|---|---|---|---|---|
| | **10 ps** | **20 ps** | **30 ps** | **40 ps** | **10 ps** | **20 ps** | **30 ps** | **40 ps** | **10 ps** | **20 ps** | **30 ps** | **40 ps** |
| O1-V2 | 1.998 | 2.588 | 2.256 | 1.988 | -1.118 | -0.207 | -0.475 | -1.006 | -1.090 | -0.202 | -0.524 | -0.973 |
| F47-V3 | 1.998 | 2.022 | 1.942 | 1.999 | -0.743 | -0.699 | -0.873 | -0.784 | -0.734 | -0.694 | -0.859 | -0.736 |
| O1-Nb2 | 2.252 | 1.967 | 2.100 | 2.149 | -1.138 | -2.006 | -1.582 | -1.495 | -1.144 | -1.997 | -1.564 | -1.516 |
| F3-V15 | 2.057 | 1.964 | 2.066 | 1.993 | -0.577 | -0.825 | -0.607 | -0.736 | -0.576 | -0.822 | -0.669 | -0.742 |

Table A.5: Structural properties of BCC refractory metal unit cells calculated using DFT with PBE functional and 2b+3b tabGAP potentials. The lattice constant and bulk modulus were derived from Murnaghan's equation of state (Figure S3 & S4) and compared to experiment room-temperature values.

| **Refractory Metal** | $\boldsymbol{E_0}$ **(eV)** | | $\boldsymbol{a}$ **(Å)** | | | $\boldsymbol{B}$ **(GPa)** | | |
|---|---|---|---|---|---|---|---|---|
| | **DFT** | **tabGAP** | **DFT** | **tabGAP** | **Expt.** | **DFT** | **tabGAP** | **Expt.** |
| Nb | -21.218 | -20.305 | 3.291 | 3.273 | 3.300 | 164.7 | 147.2 | 170.0 |
| Mo | -23.148 | -22.027 | 3.140 | 3.116 | 3.147 | 319.1 | 274.0 | 230.0 |
| Ta | -24.912 | -23.392 | 3.291 | 3.295 | 3.301 | 202.5 | 154.9 | 200.0 |
| W | -27.410 | -25.942 | 3.164 | 3.157 | 3.165 | 346.6 | 292.2 | 323.0 |
| V | -19.046 | -18.007 | 2.958 | 2.971 | 3.030 | 221.0 | 174.0 | 160.0 |

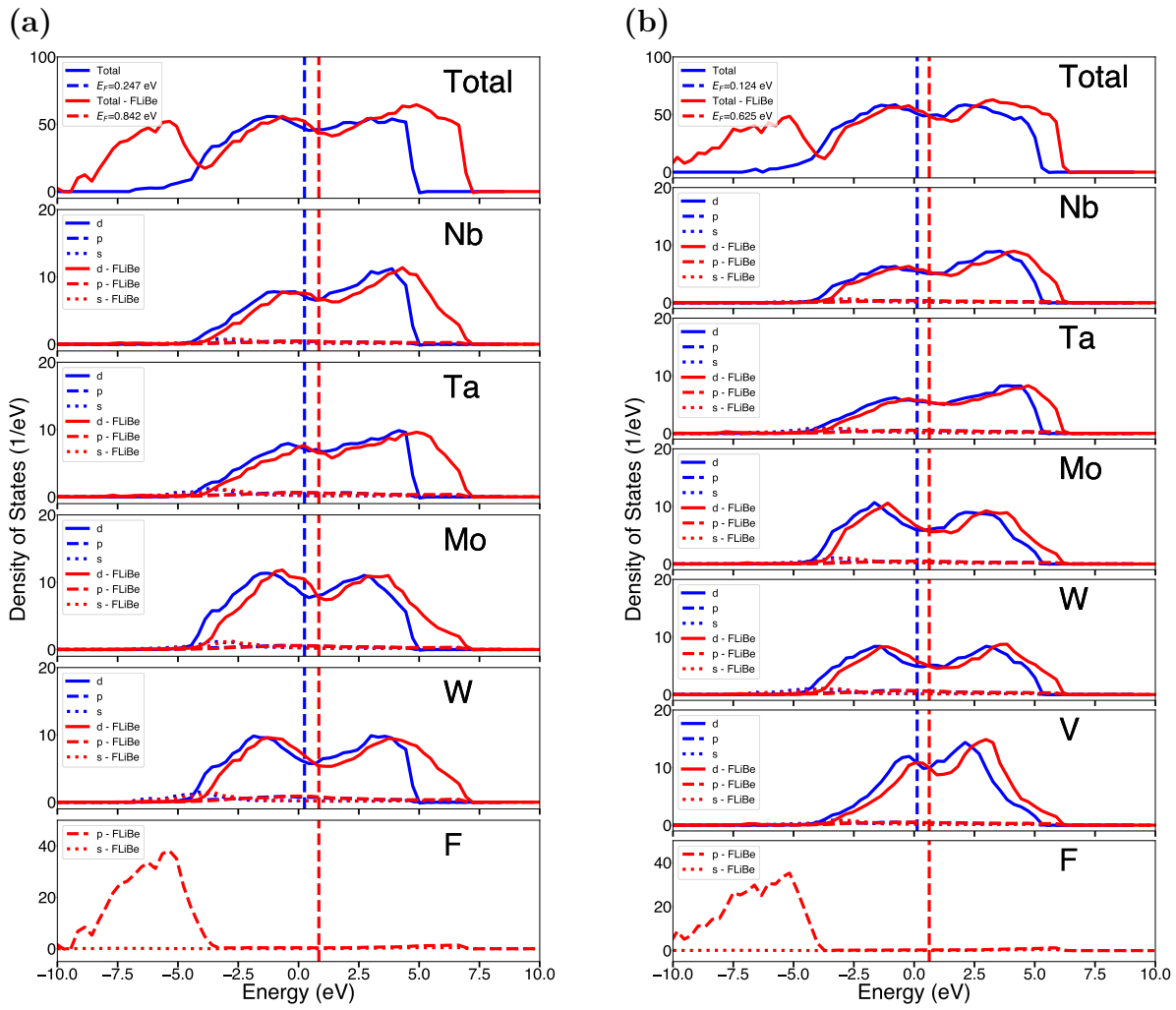



Figure A.1: Total and partial density of states of BCC (100) surfaces of (a) NbTaMoW and (b) NbTaMoWV, in contact with a molten FLiBe salt after 20 ps at 800 K. The blue curves represent the DOS of the clean refractory high-entropy alloy (RHEA) surface without the salt layer, while the red curves show the DOS with the FLiBe layer present.

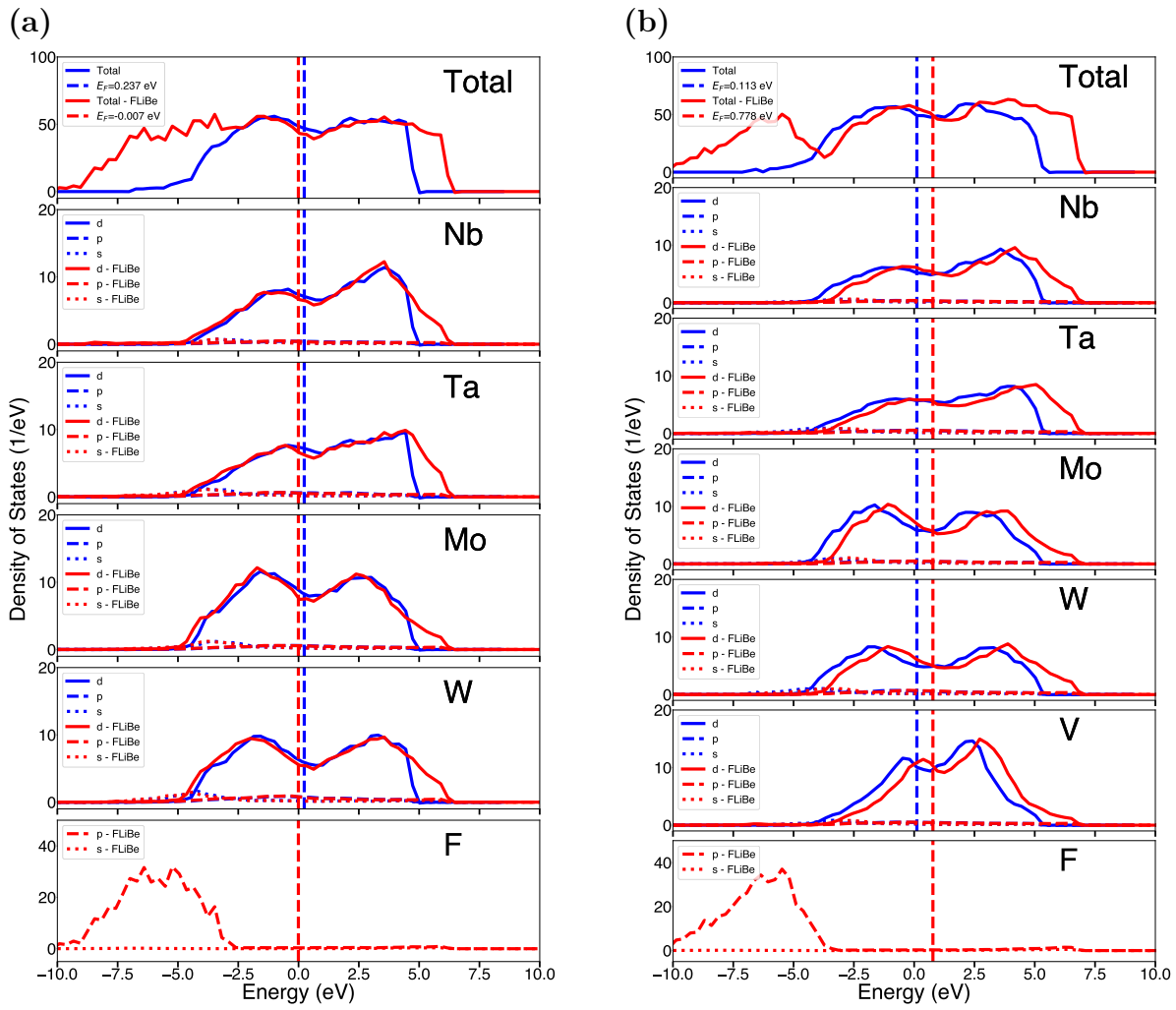



Figure A.2: Total and partial density of states of BCC (100) surfaces of (a) NbTaMoW and (b) NbTaMoWV, in contact with a molten FLiBe salt after 30 ps at 800 K. The blue curves represent the DOS of the clean refractory high-entropy alloy (RHEA) surface without the salt layer, while the red curves show the DOS with the FLiBe layer present.

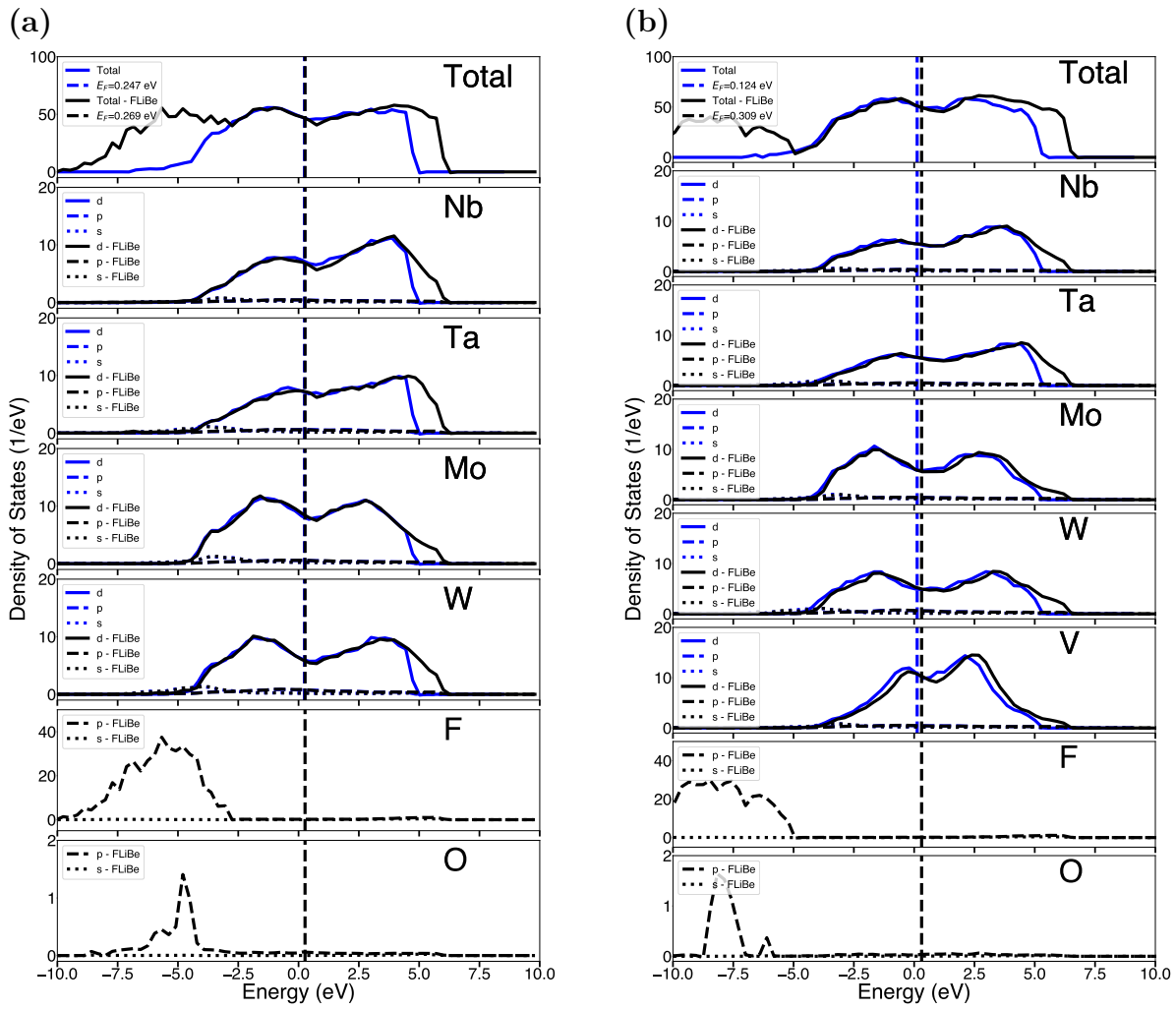



Figure A.3: Total and partial density of states of BCC (100) surfaces of (a) NbTaMoW and (b) NbTaMoWV, in contact with a molten FLiBe salt contaminated with a $H_2O$ molecule after 20 ps at 800 K. The blue curves represent the DOS of the clean refractory high-entropy alloy (RHEA) surface without the salt layer, while the black curves depict the DOS with the H2O-contaminated FLiBe layer present.

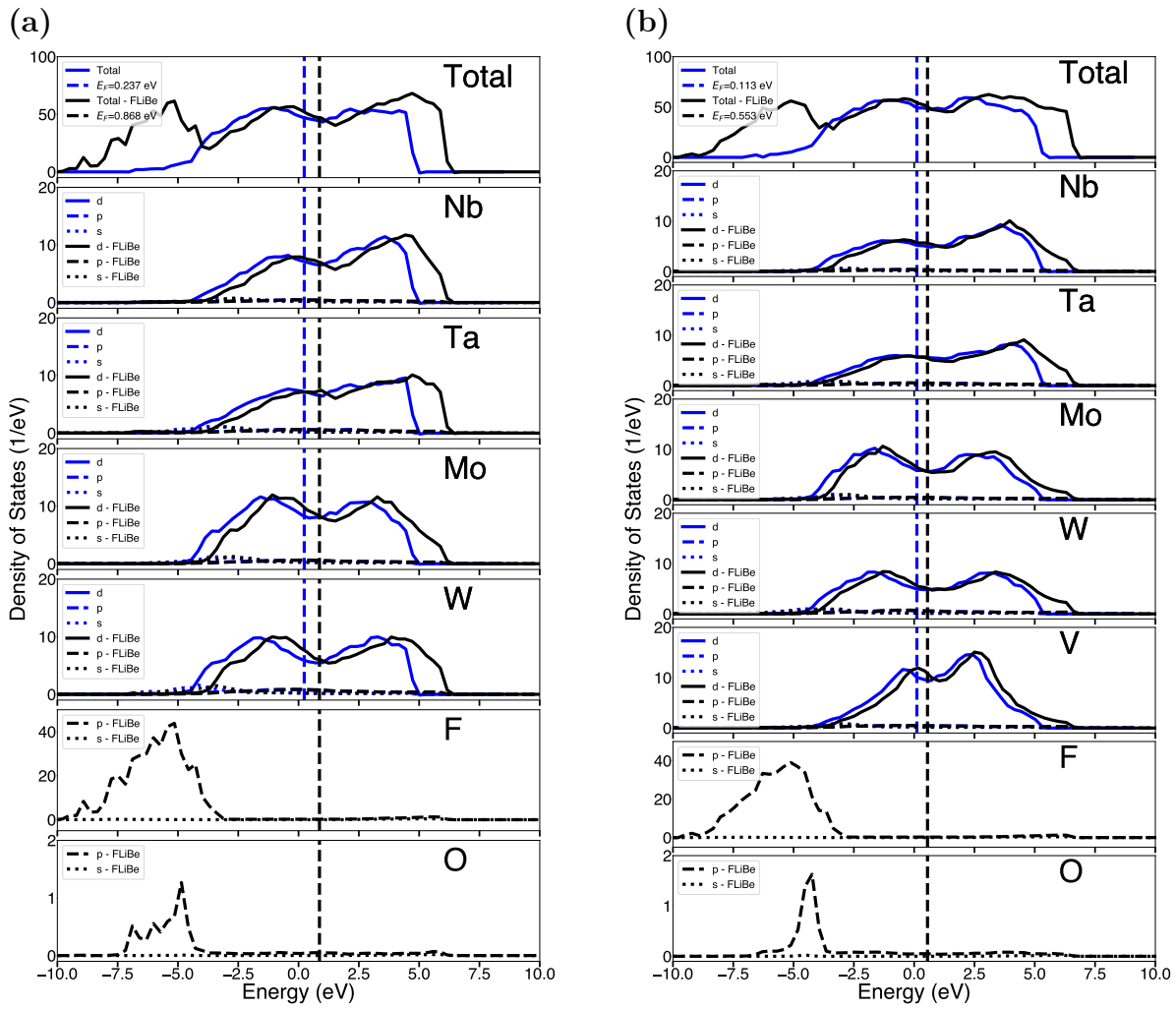



Figure A.4: Total and partial density of states of BCC (100) surfaces of (a) NbTaMoW and (b) NbTaMoWV, in contact with a molten FLiBe salt contaminated with a $H_2O$ molecule after 30 ps at 800 K. The blue curves represent the DOS of the clean refractory high-entropy alloy (RHEA) surface without the salt layer,while the black curves depict the DOS with the H2O-contaminated FLiBe layer present.

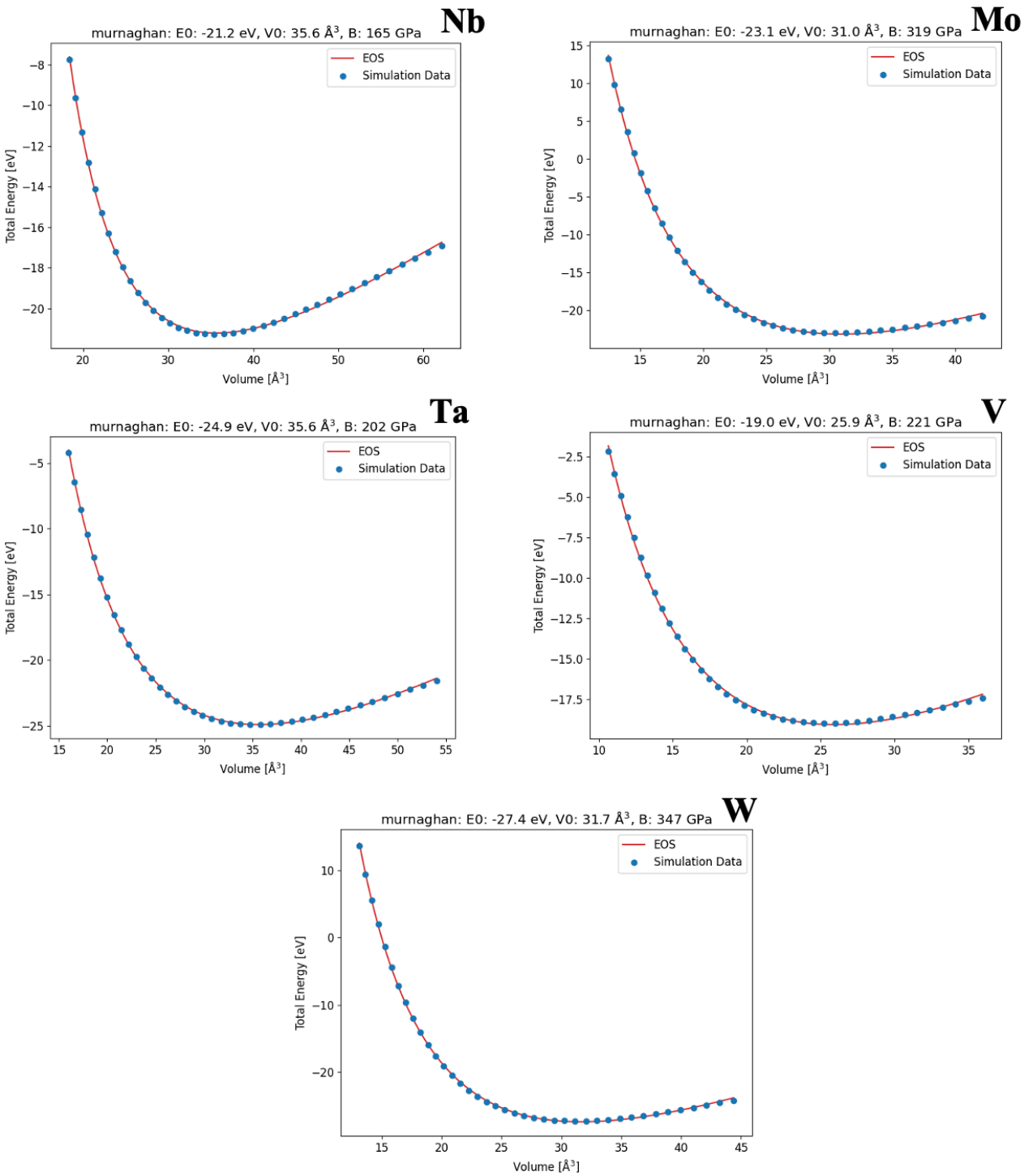



Figure A.5: Murnaghan's equation of state for BCC refractory metal unit cells calculated using Density Functional Theory with PBE exchange-correlation functional.

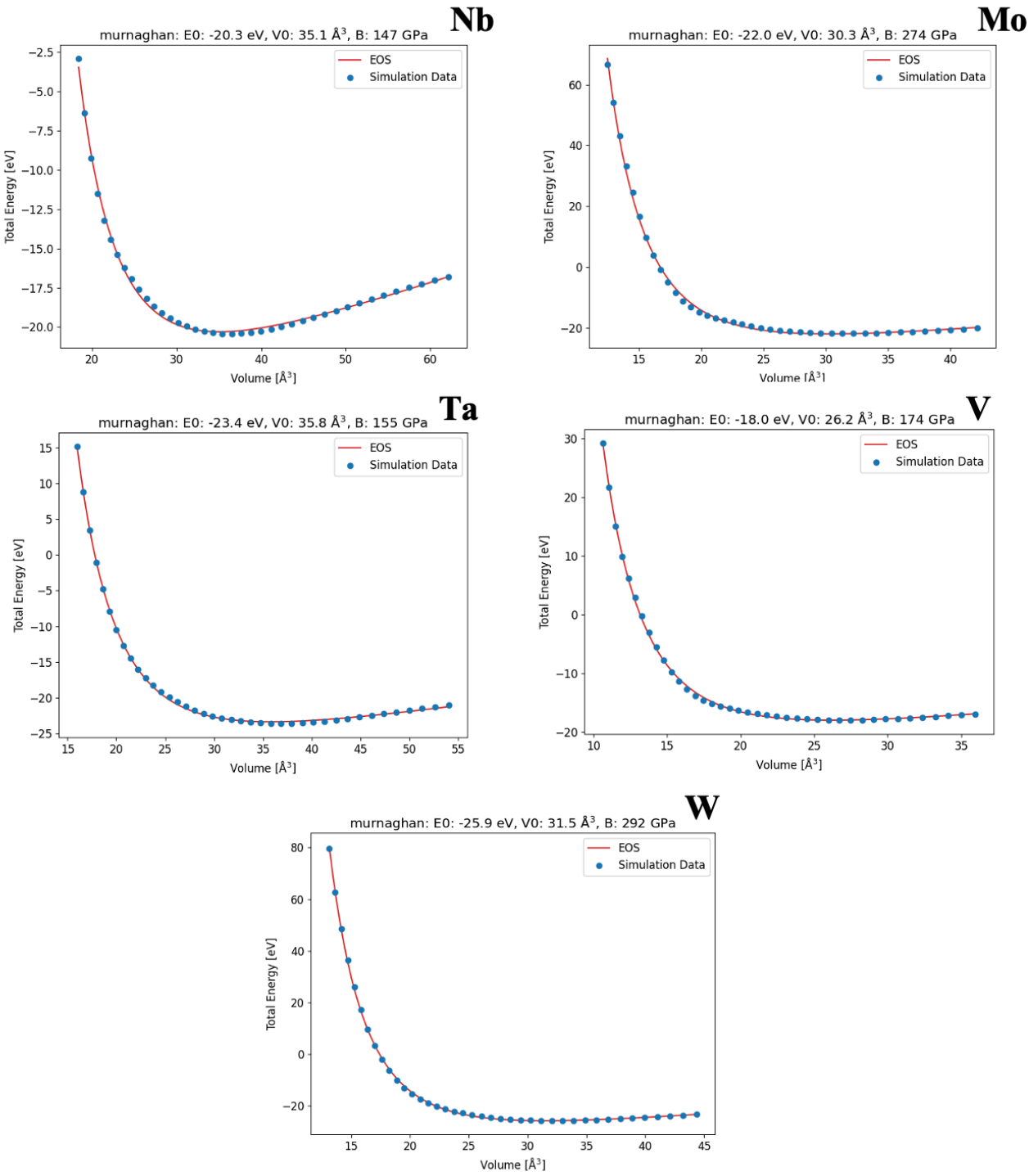



Figure A.6: Murnaghan's equation of state for BCC refractory metal unit cells calculated using using 2b+3b tabGAP potentials.

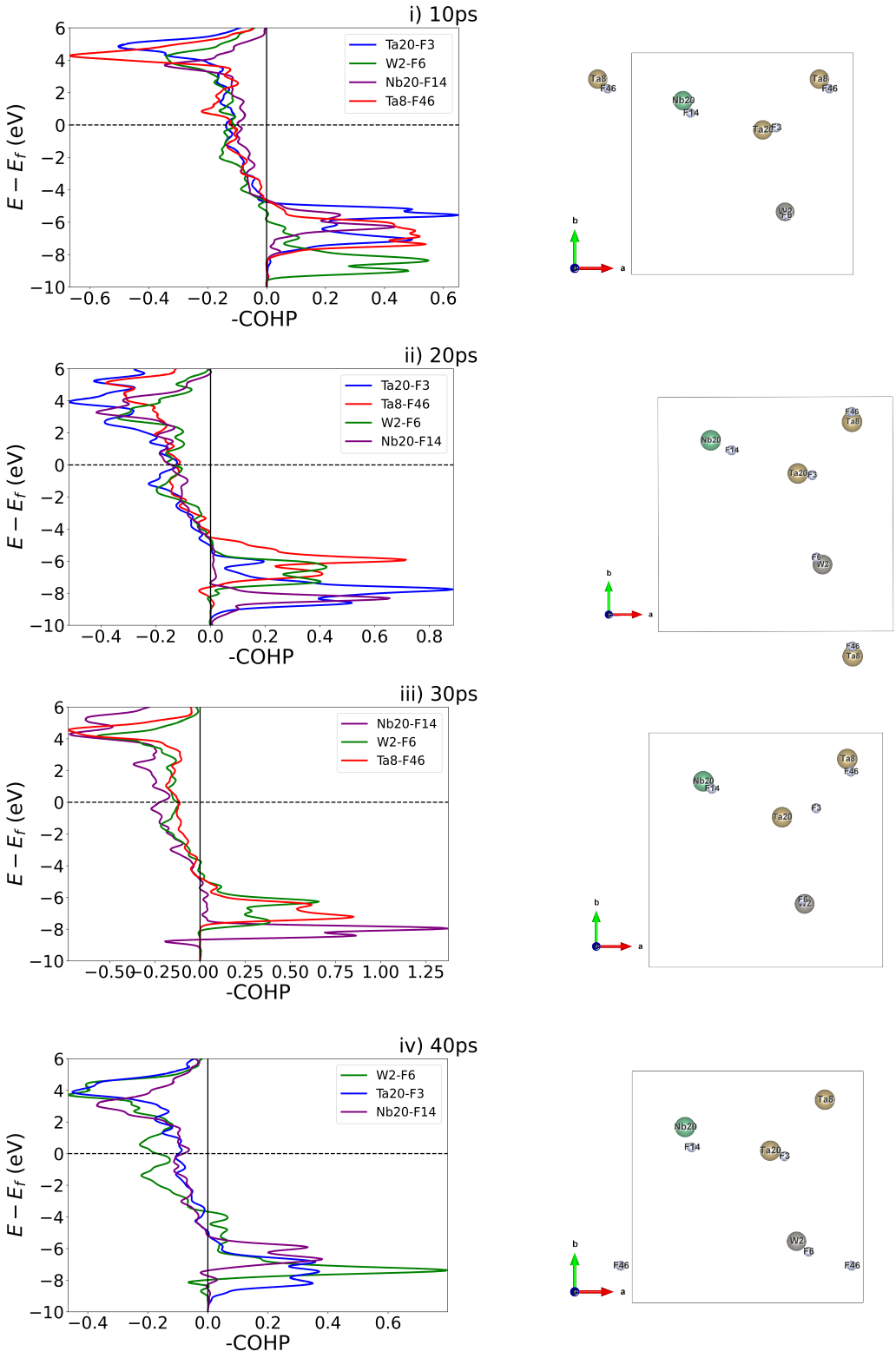



Figure A.7: Crystal Orbital Hamilton Population (COHP) analysis of the BCC (100)-NbTaMoW surface in contact with molten FLiBe at 800 K, shown at four time points: (i) 10 ps, (ii) 20 ps, (iii) 30 ps, and (iv) 40 ps. Left: COHP plots highlighting the evolution of metal–fluorine bonding interactions over time, and right: top-view snapshots of the salt–alloy interface corresponding to each time step.

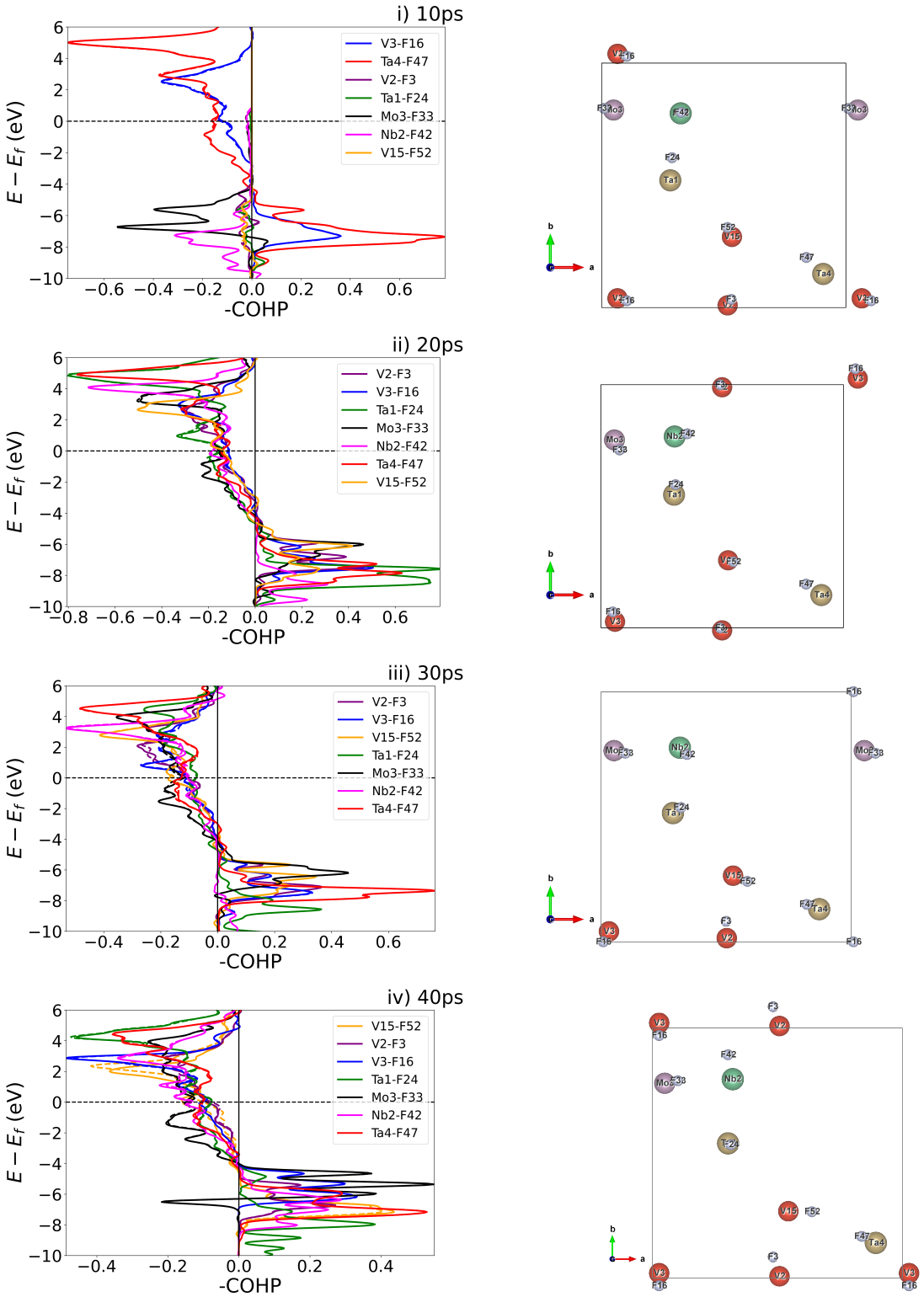



Figure A.8: Crystal orbital Hamilton population (COHP) analysis of the BCC (100)-NbTaMoWV surface in contact with molten FLiBe at 800 K, shown at four time points: (i) 10 ps, (ii) 20 ps, (iii) 30 ps, and (iv) 40 ps. Left: COHP plots highlighting the evolution of metal–fluorine bonding interactions over time, and right: top-view snapshots of the salt–alloy interface corresponding to each time step.

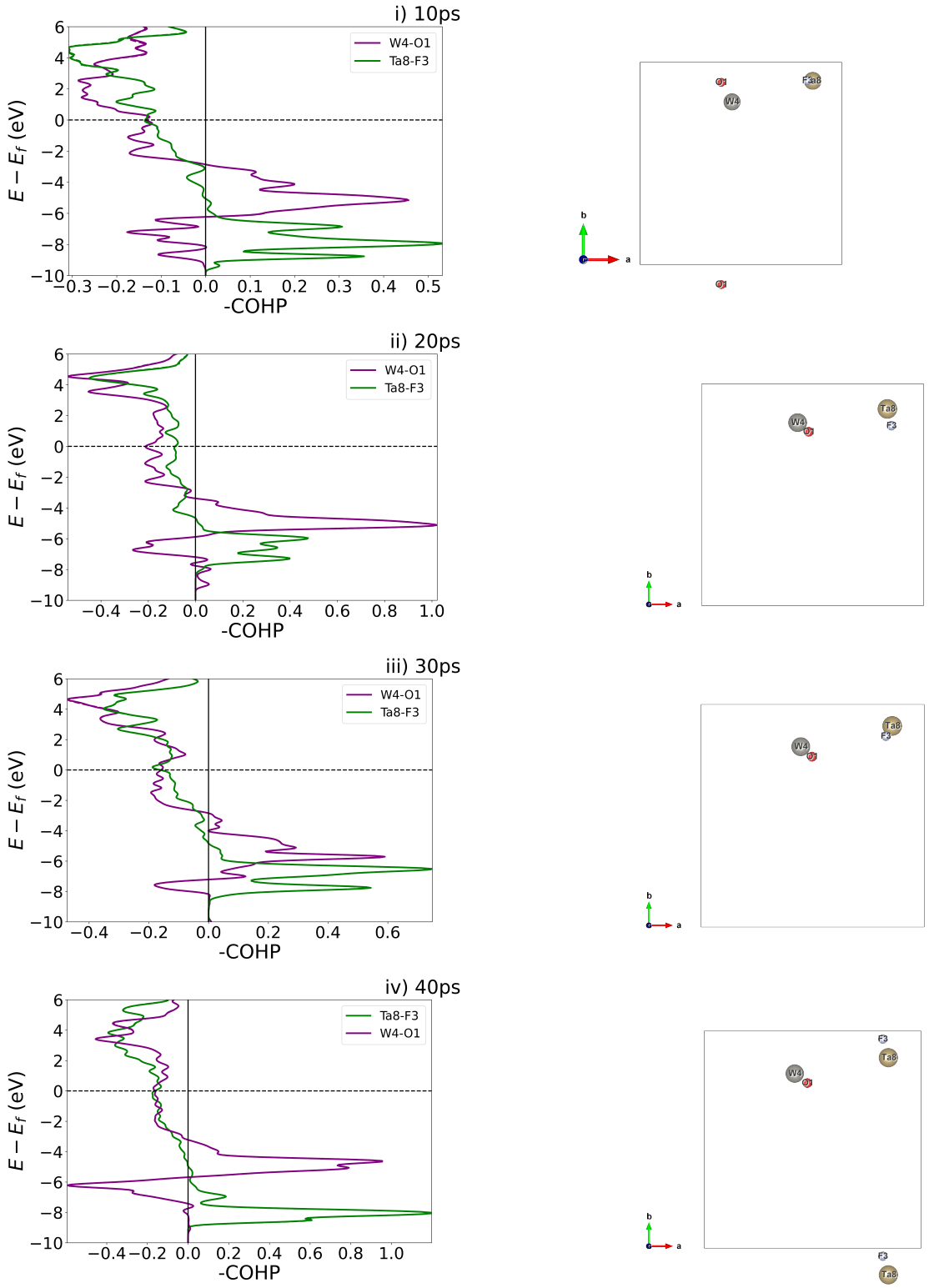



Figure A.9: Crystal orbital Hamilton ppulation (COHP) analysis of the BCC (100)-NbTaMoW surface in contact with molten FLiBe contaminated with a $H_2O$ molecule at 800 K, shown at four time points: (i) 10 ps, (ii) 20 ps, (iii) 30 ps, and (iv) 40 ps. Left: COHP plots highlighting the evolution of metal–fluorine and metal-oxygen bonding interactions over time, and right: top-view snapshots of the salt–alloy interface corresponding to each time step.

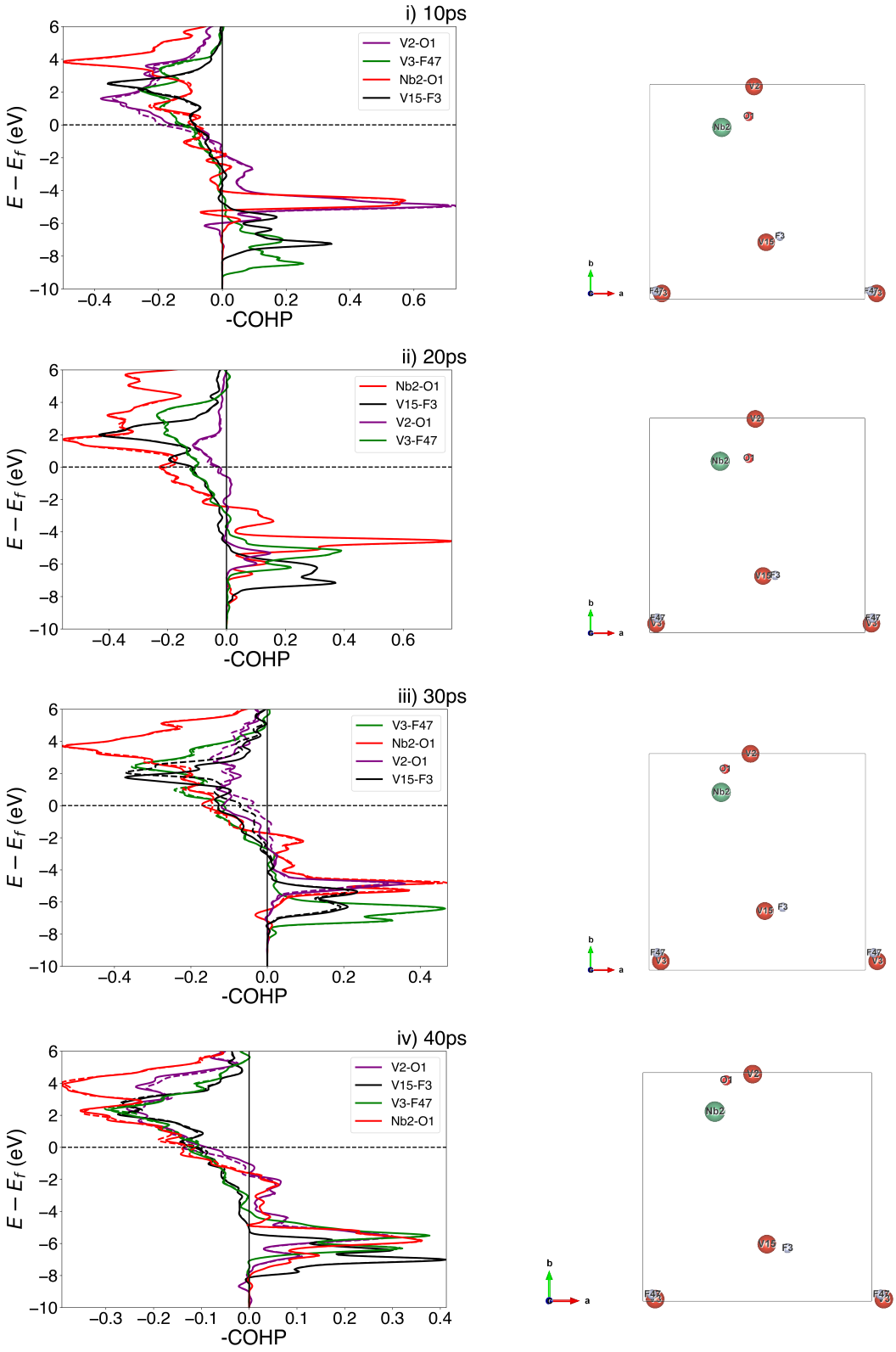



Figure A.10: Crystal orbital Hamilton population (COHP) analysis of the BCC (100)-NbTaMoWV surface in contact with molten FLiBe contaminated with a $H_2O$ molecule at 800 K, shown at four time points: (i) 10 ps, (ii) 20 ps, (iii) 30 ps, and (iv) 40 ps. Left: COHP plots highlighting the evolution of metal–fluorine and metal-oxygen bonding interactions over time, and right: top-view snapshots of the salt–alloy interface corresponding to each time step.

# Appendix B

# Revised Simulation Workflow and Observations

## B.1 Revised Computational Workflow

Due to the substantial loss of the BCC lattice arrangement observed in Fig. 3.1 and the potential co-existence of both solid and liquid phases depicted in Fig. 3.2 after equilibration of both RHEA slabs at 800 K using the tabGAP machine-learned potential[82], the initial computational framework in Fig. 2.1 was updated accordingly in Fig. B.1. Specifically, the thermally equilibrated FLiBe salt overlay is directly added to the BCC (100)-NbTaMoW and (100)-NbTaMoWV surfaces at 0 K as illustrated in Fig. B.1 without performing an *NPT* simulation on the RHEAs at 800 K. The assumption that the RHEA slabs remain a single-phase BCC crystalline at 800 K and undergo a negligible volume change from 0 to 800 K is made. It is possible that the tabGAP force field parameterized for the RHEAs is not transferrable to higher temperatures, thereby misrepresenting the chemical system at 800 K. Additionally, during construction of the salt-alloy interface, the $H_2O$ molecule was moved deeper into the salt system in the revised computational workflow by translating the $H_2O$ molecule further in the positive z-direction. It is expected that the $H_2O$ molecule dissociates into $H^+$ and $OH^-$ early in the simulation as reported by Schneider's research group[66].

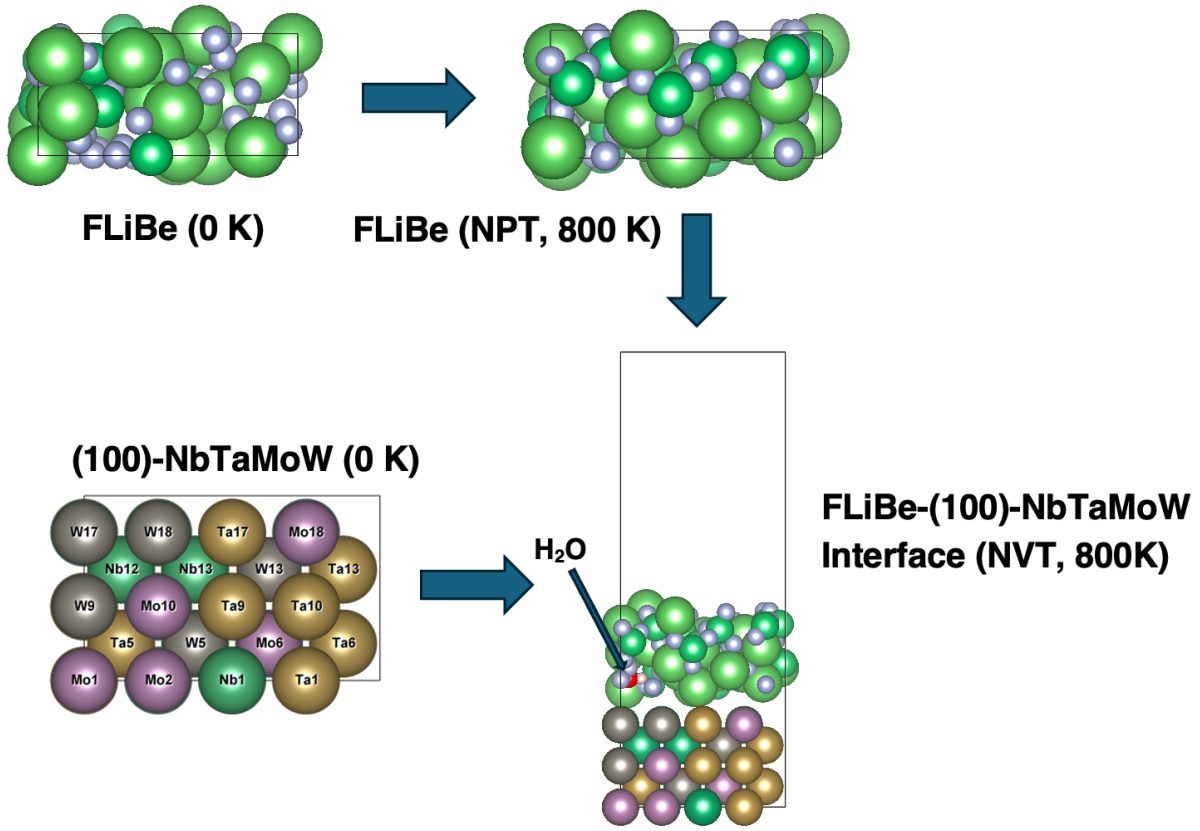



Figure B.1: Revised workflow for constructing the refractory high entropy alloy (RHEA)–salt interface. Top left: Initial configuration of FLiBe at 0 K. Top right: Thermally equilibrated FLiBe at 800 K under *NPT* conditions. Bottom left: Initial BCC (100)-NbTaMoW slab at 0 K. Bottom right: Construction of the interface between the BCC slab and the equilibrated molten salt, under *NVT* conditions at 800 K. 1 $H_2O$ molecule was added to the FLiBe salt and the system was simulated in the *NVT* ensemble.

## B.2 Revised Observations

### B.2.1 Radial Distribution Function

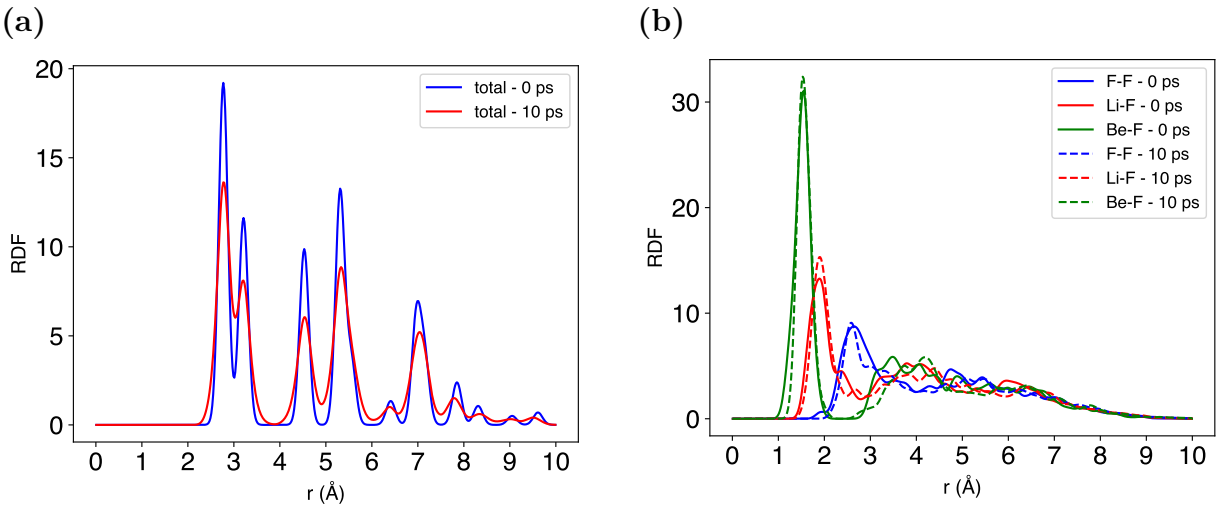



Figure B.2: a) Total radial distribution function for the metal surface component of the $H_2O$-contaminated FLiBe-NbTaMoW interface and the b) Radial distribution function for the fluoride bonds in the $H_2O$-contaminated FLiBe overlay on NbTaMoW after 10 ps at 800 K in the *NVT* ensemble.

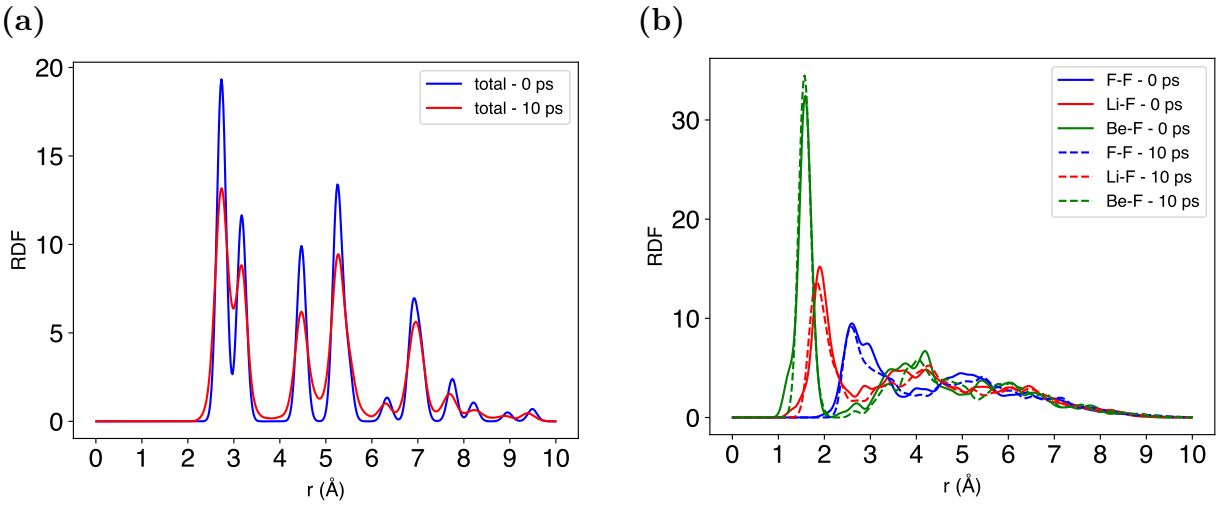
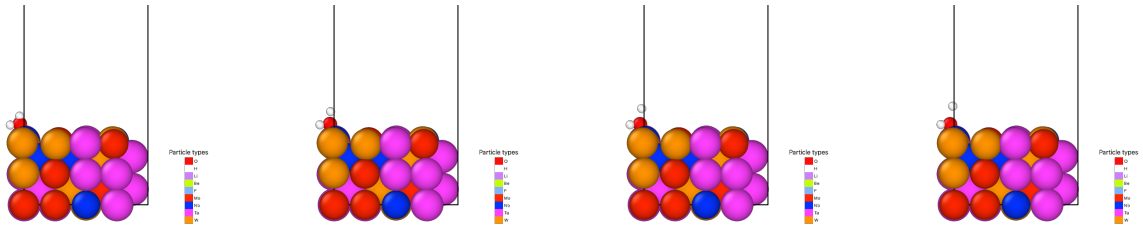



Figure B.3: a) Total radial distribution function for the metal surface component of the $H_2O$-contaminated FLiBe-NbTaMoWV interface and the b) Radial distribution function for the fluoride bonds in the $H_2O$-contaminated FLiBe overlay on NbTaMoWV after 10 ps at 800 K in the *NVT* ensemble.

As evidenced by the long-range ordering in the radial distribution function for NbTa-

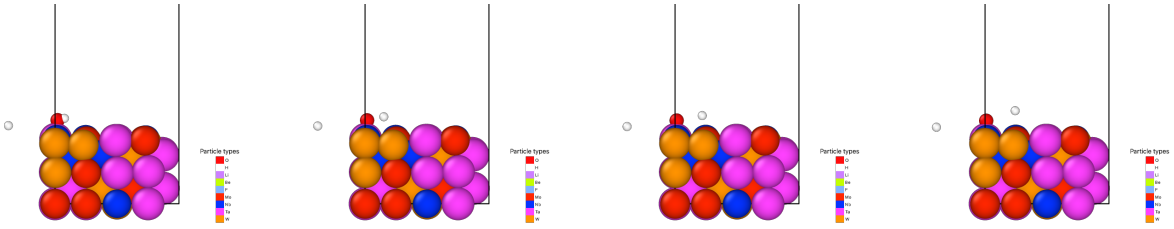
MoW and NbTaMoWV surfaces (Fig. B.2-a. and Fig. B.3-a., respectively), both refractory high entropy alloys (RHEAs) remain solid after 10 ps at 800 K in the revised simulation detailed in Fig. B.1. The merging of the first two RDF peaks accompanied by a reduction in the intensity of subsequent peaks in Fig. B.2-a. and Fig. B.3-a. indicate that both metal surfaces are no longer a single-phase BCC crystalline due to the displacement of some atoms from their initial BCC lattice arrangement after 10 ps at 800 K. Upon exposure to the metal surface for 10 ps at 800 K, the salt exhibits only minor variations in its local structure as depicted in Fig. B.2-b. and Fig. B.3-b. Hence, the RHEA surfaces do not change the salt chemistry in the preliminary stages of corrosion.

### B.2.2 $H_2O$ Reaction Mechanism



(a) (b) (c) (d)

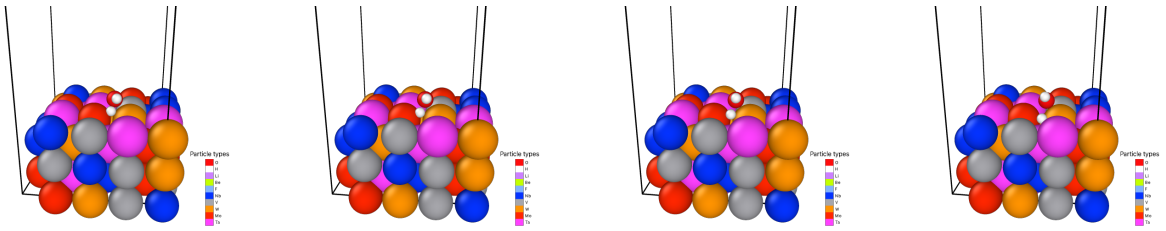
Figure B.4: The splitting of the $H_2O$ molecule at the molten FLiBe-NbTaMoW interface after a) 0.155 ps, b) 0.156 ps, c) 0.157 ps and d) 0.158 ps at 800 K in the *NVT* ensemble. The top FLiBe overlay was removed from the interface to allow an unobstructed view of the $H_2O$ molecule.



(a) (b) (c) (d)

Figure B.5: The splitting of the $OH^-$ molecule at the molten FLiBe-NbTaMoW interface after a) 0.815 ps, b) 0.816 ps, c) 0.817 ps and d) 0.818 ps at 800 K in the *NVT* ensemble. The top FLiBe overlay was removed from the interface to allow an unobstructed view of the $H_2O$ molecule.

The $H_2O$ within the FLiBe salt approaches the interface between the salt and the alloy as a molecule and thereafter undergoes partial dissociation into $H^+$ and $OH^-$ as was



(a) (b) (c) (d)

Figure B.6: The splitting of the $H_2O$ molecule at the molten FLiBe-NbTaMoWV interface after a) 0.026 ps, b) 0.028 ps, c) 0.030 ps and d) 0.032 ps at 800 K in the *NVT* ensemble. The top FLiBe overlay was removed from the interface to allow an unobstructed view of the $H_2O$ molecule.

discovered by Schneider et al.[66]. The splitting mechanism of $H_2O$ at the salt-alloy interface is monitored using the OVITO[93] visualization software in Fig. B.4-B.6. The top FLiBe overlay was removed from the interface to allow an unobstructed view of the $H_2O$ molecule. At the $H_2O$-contaminated FLiBe-NbTaMoW interface, $H_2O$ splits into $H^+$ and $OH^-$ after 0.156 ps at 800 K as shown in Fig. B.4. Interestingly, the resulting $OH^-$ further splits into $O^{2-}$ and $H^+$ after 0.816 ps as shown in Fig. B.5. At the $H_2O$-contaminated FLiBe-NbTaMoWV interface, the splitting of $H_2O$ into $H^+$ and $OH^-$ is observed after a mere 0.028 ps, earlier on in the simulation compared to the interface with NbTaMoW.

### B.2.3 Density of States

The density of states (DOS) is calculated in Fig. B.7 for the $H_2O$-contaminated FLiBe interfaces with a) NbTaMoW and b) NbTaMoWV after 10 ps at 800 K in the revised simulation detailed in Fig. B.1. The results are mainly similar to those observed during the previous simulation in Fig. 3.4, except that the DOS curves are smoother in the former, which could be attributed to the phase transition from solid to liquid observed in Fig. 3.2. Additionally, the changes in the partial DOS of the individual metal constituents upon the addition of $H_2O$ (black curve) are minimal in Fig. B.7-a., indicating the need to analyze more trajectory snapshots to better account for the system's dynamism.

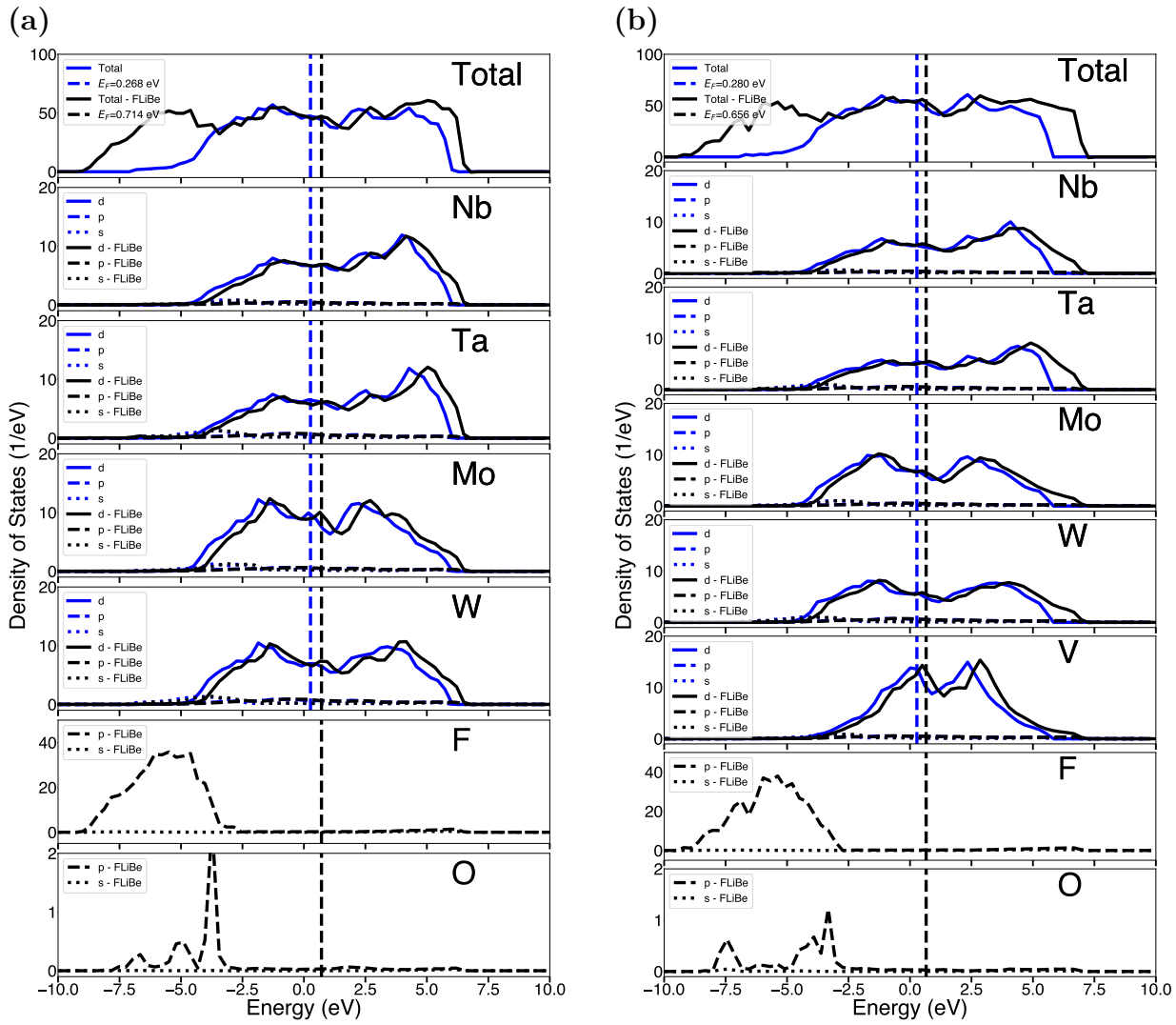



Figure B.7: Total and partial density of states of the BCC (100) a) NbTaMoW and b) NbTaMoWV surfaces, in contact with a molten FLiBe salt contaminated with a $H_2O$ molecule after 10 ps of the revised simulation at 800 K. The blue curves represent the DOS of the clean refractory high-entropy alloy without the FLiBe layer, while the black curves depict the DOS with the $H_2O$-contaminated FLiBe layer present. The dotted blue and black vertical lines represent the Fermi level of the clean RHEA surface and the RHEA with the $H_2O$-contaminated salt, respectively.

### B.2.4 Crystal Orbital Hamilton Population Analysis

The crystal orbital Hamilton population analysis was conducted for both RHEA compositions in hydrated salt in Fig. B.8 after 10 ps at 800 K in the revised simulation detailed in Fig. B.1. At the interface between $H_2O$-contaminated FLiBe and NbTaMoW, a sharp

-COHP peak is observed for Ta20-F39 below the Fermi level at -6.5 eV, substantiating the reactivity of Ta towards F previously documented. In contrast, a modest -COHP peak is observed for Ta17-F18 at $\sim$-8 eV. Upon incorporation of vanadium (V) into the alloy, low-intensity, broad -COHP peaks are observed for both V16-F14 and V15-F56, further manifesting the weak bonding interactions between V and F.

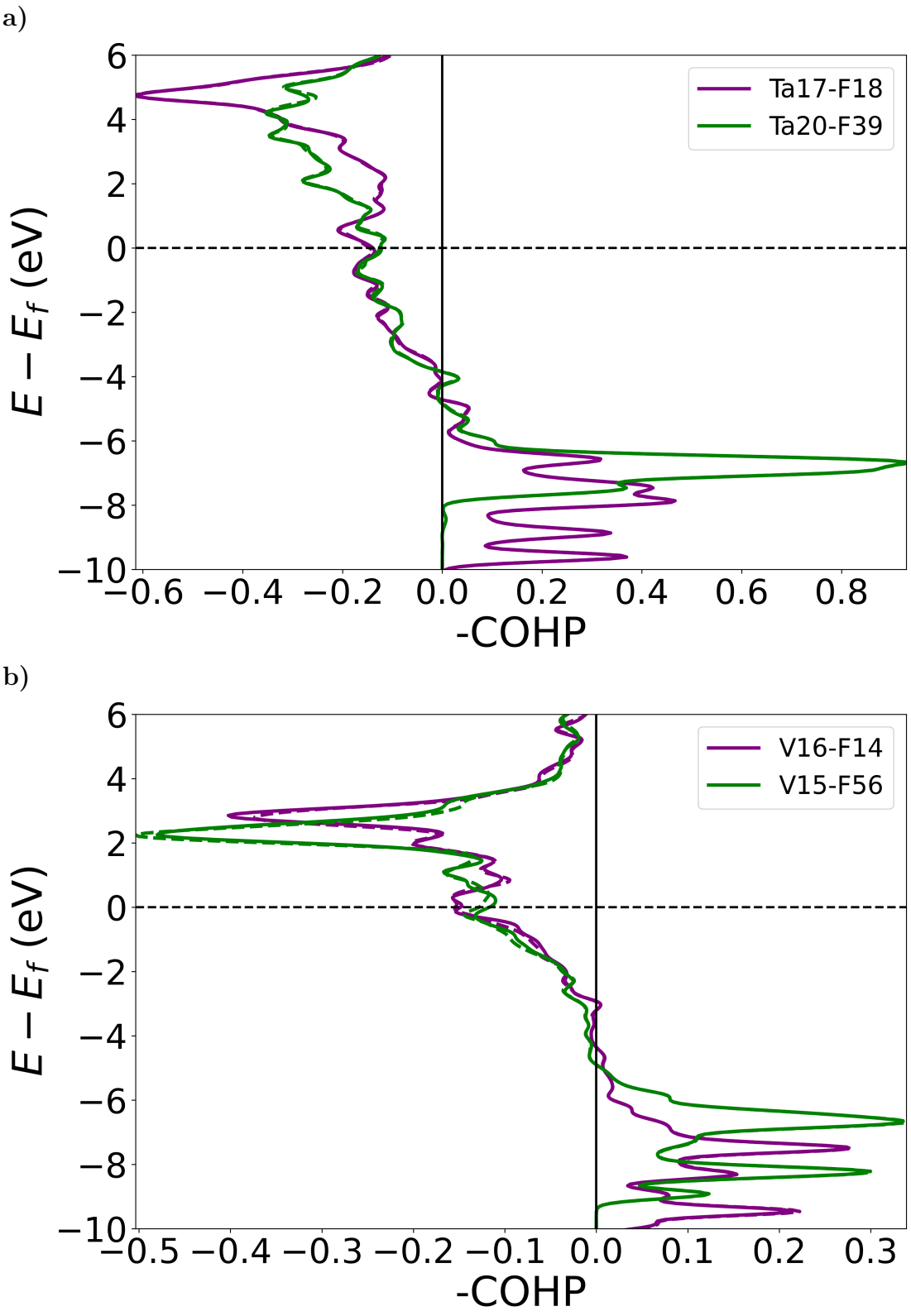



Figure B.8: Crystal orbital Hamilton population (COHP) analysis of the BCC (100) surfaces of a) NbTaMoW and b) NbTaMoWV in contact with molten FLiBe contaminated with a $H_2O$ molecule after 10 ps of the revised simulation at 800 K. The black dotted line represents the Fermi level which is set to 0 eV.